
**Università degli Studi di Palermo**

DIPARTIMENTO DI SCIENZE FISICHE E ASTRONOMICHE
Corso di Dottorato di Ricerca in Fisica

Tesi di Dottorato di Ricerca in Fisica

# Computational Studies on $BaCeO_3$ and $BaZrO_3$ Derivatives

New Models and Protocols

Candidato
**Antonio Cammarata**

Tutor
**Prof. Antonio Emanuele**

Co-Tutor
**Prof. Dario Duca**

**Ciclo XXII**

Ph.D. Thesis of Antonio Cammarata
in partial fulfillment of the requirements
to get the degree of “Doctor of Philosophy in Physics”

Department of Physical and
Astronomical Sciences
University of Palermo
Palermo, Italy, year 2011

To my brother Vincenzo
and to my parents

# Contents

# Introduction

Constant technological worldwide development and increasing world population are the most appropriate indicators to understand how much rapidly energy demand increases. The reached levels impose incisive and well articulated energy production and stock plans, in order to sustain such global growth rate. These problems leaded to the concept of *Sustainable Development*, a body of relationships among human activities and biosphere in which they take place, assuring actual and future generations needs.

Nowadays, continuous energy demand is mainly satisfied by non-renewable fonts. Sustainable development of the energetic system has the target to improve human being quality, developing production energy methods with low environmental impact. Actual transformation energy systems are not enough efficient to match the present needs with the sustainability requirements well defined in the Brundtland report.

All that acts as a strong driving force towards development of high efficiency energy production and distribution. Great expectations to help in finding solutions to these questions are placed on solid protonic conductors. They propose as efficient devices for energy conversion through their use in fuel cells, besides playing a fundamental role in realizing reactors for nuclear fusion plants. Protonic conduction process is not well understood and many groups around the world are hardly working in this fast growing field. From a fundamental physics viewpoint studies on proton conduction and its counterpart, proton trapping, appear to show the same exciting ingredients of the electron conduction/trapping in silver halides in the 50s of last century. That is, great pressure towards applications and the challenge to understand structural and dynamic properties of matter at microscopic level. Essentially two main approaches are used: experimental and computational ones.

The study here proposed has the aim to investigate the local environment of protonic sites and the protonic transfer phenomenon by means of computational techniques, in order to bring a further contribution to the interpretation of experimental data and to suggest specific researches in designing new protonic conducting materials. In fact, results coming from computation can shed light in fundamental physical aspects and subtleties virtually impossible to study experimentally.

In particular, barium cerate and barium zirconate perovskites and their

derived protonic conductors are studied, making correspondences among structural modifications induced on the native compound by cation substitution and the proton conducting ability. Ab initio as well as Molecular Dynamics computational methods are used. Among the outcomes, non trivial features of the yttrium atom as a substituent for the tetravalent cation in perovskite materials is inferred. Our findings reproduce experimental results and provide a novel structural explanation of them. Also, first simulation results on proton dynamic reveal unexpected features which open room to further research work.

The first chapters is a survey on proton conduction mechanisms and related materials; next, a general overview on computational models and the state of art of the title compounds is given, describing in details the models used for the present calculations. Finally, three chapters are devoted to the presentation of the obtained results, discussing related implications on designing new protonic conducting materials.

# Chapter 1

# Protonic Conductivity and Related Materials

The ability of conducting protons is a characteristic owned by as many as different class of structures — be them crystalline, molecular or amorphous ones, and have a fundamental role in many important processes like photosynthesis or electricity production. Studies on it span across many scientific field of interest, and efforts are mainly devoted to understand the protonic conduction mechanism and to design, as the last aim, protonic conducting materials. The latter are fundamental part of devices of technological interest, *Fuel Cells* among the most important. These are a good candidate for energy conversion satisfying either the actual progress needs or the requirements for a sustainable development.

Nonetheless, the details of the elementary processes on which protonic conduction is based are still not clear, since they often depend on the specific systems taken into consideration. So, in order to describe the phenomenon of the protonic conductivity in a unitary framework, a good starting point could be to single out which are the common features of the proton behaviours in the different environments it can reside.

## 1.1 Chemistry of the Proton

Complexity of the protonic conduction mechanism can be easily viewed if we look briefly to the chemistry of the proton. The proton is the only ion which is not surrounded by electronic shells, so it is strongly interacting with the electron density of its environment. In metals, for example, the delocalized electron density of the conduction band encloses the proton, thus creating a positive or negative ion according to the position of H 1s energy level relatively to the Fermi energy of the pure metal. In non-metallic environment, the proton interacts with the electron density of its nearest neighbour atoms. If the latter are oxygen atoms, proton can create with

them an O−H bond of about 1 Å length and hydrogen bonds of about 2.6 Å length, all with a strong directional character.

In compounds with a low concentration of electronic charge carriers, proton can be considered confined within the electron density enclosing it. This situation is observed, for example, in a rigid array of host species like a crystalline oxide, where no significant translational motion of protons is allowed and only the local ones (e.g. vibrations) occur. Nonetheless, in the 1960s, Fischer, Hofacker and Rathner understood that the dynamic of the proton environment may assist proton diffusivity [1, 2, 3, 4].

The ways in which proton diffuses can be grouped into two big mechanisms, both sharing the hypothesis that proton is not free but it is bounded to some chemical species. The first simple one is the *vehicle mechanism* [5], in which proton migration is due to the translational dynamics of bigger species: the proton is bound to a vehicle (e.g. $H_3O^+$) whose diffusion rate determines the one of the proton. If the "vehicle" cannot have a drift velocity but only local motions (e.g. oxygen atoms in a crystalline matrix), the protons can be transferred from one "vehicle" to another through reorganizations of the proton environment; this second one is termed as *Grotthuss mechanism* [6]. The reorganization usually involves the rearrangement of the vehicle and its surrounding as well as dipole reorientation*. The relevant rates for this mechanism are the ones relative to the proton transfer and the reorganization of its environment; also, increasing the temperature, proton diffusion progressively changes from Grotthuss-type dominated to vehicle-type dominated mechanisms.

## 1.2 Protonic Conduction Models

In order to understand the details of protonic conduction mechanisms, it turns to be necessary to analyse the general features of the hydrogen bond and to single out which are its peculiarities in proton conducting materials.

The hydrogen bond is a weak directional interaction, whose energy values range from 0.1 to 0.6 eV, about 1 order of magnitude lower than those of other types of chemical bonds. This enables hydrogen bond to adapt easily to the environment and to be sensitive to thermal fluctuations. In liquid systems where hydrogen bonding is the main intermolecular interaction, like $H_2O$ and $NH_3$, short-range ordering appears with strong fluctuation in time and space, leading to "flickering clusters", as they were termed in first studies on local structure of liquid water [7].

The isolated dimer $H_5O_2^+$ has a minimum when the separation $O\cdots O$ is of 2.40 Å, corresponding to a symmetrical hydrogen bond; this bond is as much weaker as more hydrogen bonds are found in the nearby like, for

*Electron density relative to the bond between the proton and the bounded vehicle usually singles out a dipole because of the strong ionic character of the proton.

example, in the bulk of liquid water. Stronger proton donor/acceptor bonds confine the proton donor/acceptor distance, so determining the hydrogen bond interaction. It seems that compounds with the highest proton diffusivity are hydrogen bonded liquids or solids; examples of these situations are heteropolyacid hydrates (e.g., $H_3PW_{12}O_{40}\cdot 29\,H_2O$) or acidic salts of oxoacids with big cations (e.g.,$CsHSO_4$) [8]. Deeper understanding of proton diffusivity, therefore, must include hydrogen bond fluctuations as well as the role of the environment on its properties.

The hydrogen bond must provide a path for letting the proton transfer from its donor to the acceptor species, since this seems to be the most limiting step of the overall proton diffusion.

As usually happens in most proton conductors, the proton is bound to an oxygen atom and it is transferred towards an other oxygen one. As a first simplified attempt of describing the proton transfer, let us consider the position of all the nuclei except for the hydrogen one fixed; let us call $\vec{r}$ and $\vec{R}$ the proton transfer coordinate and the oxygen coordinate respectively. Following the Born-Oppenheimer approximation [9], let us suppose that only the electronic cloud is allowed to adapt itself to the position of the proton along the transfer coordinate $\vec{r}$. Studies on a large variety of compounds show that the equilibrium position of the proton in a hydrogen bond for a given O$\cdots$O separation is quite uniform and the closest possible O$\cdots$O distance is about 2-4 Å with a symmetrical strong hydrogen bond [10]; by using these data, the energy potential has been parametrized to a Lennard-Jones type potential [11]. With this choice, the energy potential curve versus the oxygen separation $\vec{R}$ assumes a symmetric double well shape with a barrier that decreases when the O$\cdots$O separation diminishes. During the transfer, the proton is always surrounded by a non-zero electron density; the more significant is this last one, the lower is the height of the energy barrier the proton must overcome. In short, proton transfer can be described as a *hopping* process.

The average oxygen O$\cdots$O distance $\vec{R}_0$ in proton conductors is usually higher than 2.6 Å and the corresponding transfer energy barriers are higher than the observed activation enthalpies of the whole protonic conduction process. This happens probably because thermal fluctuation in $\vec{R}$ can lower the effective barrier in the energy surface $E(\vec{r},\vec{R})$. In this simplified picture, in presence of a rigid array of proton donors and acceptors, the activation enthalpy is provided only by the proton vibration with corresponding O$-$H vibration frequency of $\sim 10^{14}s^{-1}$. Excitations in $\vec{R}$ lower the energy barrier, so creating a proton transfer path that can become of diffusive type for low O$\cdots$O separations (adiabatic transfer). In this latter case, the only relevant frequency is that one of the proton donor/acceptor oscillation which is usually about 2 order of magnitudes lower than the O$-$H stretching one, as it depends on the masses of the moieties of the vehicle.

In our simplification, the total energy $E(\vec{r},\vec{R})$ can be written as follows:

$$E\left(\vec{r},\vec{R}\right) = E_{\vec{R}}\left(\vec{r}\right) + E\left(\vec{R}\right) \tag{1.1}$$

where the first term is the Lennard-Jones model potential and the second one contains second or higher order correction terms. Last term takes into account the fundamental vibration frequency of an oxygen atom in an oxide lattice (e.g. $10^{13}s^{-1}$), and possible anharmonic and repulsive effects which prevent that proton donor to acceptor distance shorten below a limit value. Generally, strong anharmonicity is shown by all kind of protonic conductors, because of strong vibrational coupling among more than one normal mode [8].

In the case of harmonic donor/acceptor vibration, the transition state energy and the donor/acceptor separation are reduced compared to the static barrier. Reducing the frequency values of $\vec{R}$ normal modes results in a shortening of the average donor/acceptor separation; by further reduction of the $\vec{R}$ frequencies, the energy of the transition decreases keeping almost unchanged the $\vec{R}$ equilibrium value around 2.4 Å, at which the barrier along $\vec{r}$ disappears. In the last case the proton transfer frequency is that of the donor/acceptor vibration, often similar to the one of the vehicle diffusion.

The simplified approach in describing terms contributing to the total energy of a protonated system is completed by taking into account all the remaining species besides the proton and its carrier, that is, those moieties belonging to the solvent. This last one can be described by using a multi-dimensional coordinate $\vec{S}$, modifying the symmetry of the proton transfer potential, for example, by polarizing the hydrogen bond. In this scenario, the symmetric double well potential discussed above becomes asymmetric making inequivalent the two possible sites in the hydrogen bond.

Let us call $\vec{S}_0$ an isotropic average solvent configuration not changing the symmetry of the double well proton potential. A fluctuation of $\vec{S}_0$ can be produced by proton motions in the hydrogen bond and, at the same time, this fluctuation can induce proton-transfer events (see Figure 1.1).

When $\vec{S} = \vec{S}_0$, the proton-transfer potential is symmetrical. The longer the proton oscillates in one of the two equivalent stable positions, the more it stabilizes this site at the expense of the other one, assisted by the solvent relaxation. Solvent interactions decrease the rate of proton transfer because the activation enthalpy increases by the amount equal to the solvent activation energy; this depends on the coupling between the solvent and the protonated moiety, and on the rate of proton-transfer compared to that of solvent relaxation. Diffusion and structural reorganizations like rotation and reorientation are phenomena that can be described by time changes of the $\vec{R}$, $\vec{S}$ and $\vec{r}$ coordinates, as elements of the proton-conduction process; in this sense, the above discussion about the contributions to the total energy, applies as a rule irrespective of which processes the coordinates represent. Like the proton-transfer mode, also the rates of diffusion, rotation

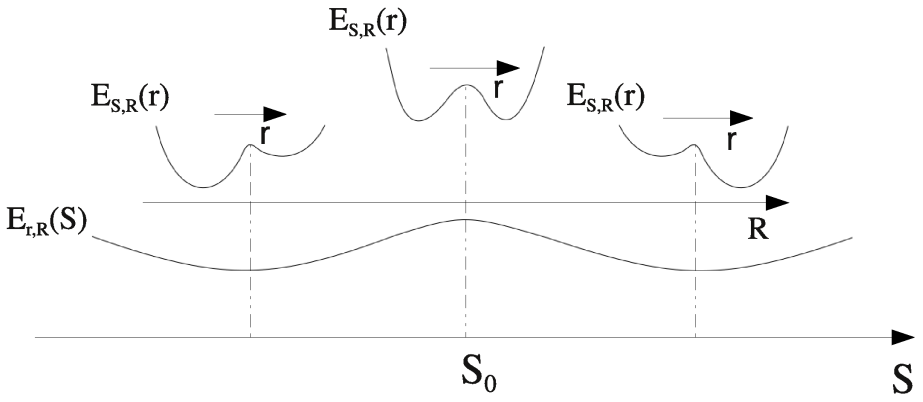


Figure 1.1: Schematic representation of the protonic transfer: $\vec{r}$ and $\vec{R}$ are the proton and oxygen coordinates respectively, while with $\vec{S}$ the multi-dimensional solvent coordinate is indicated.

and reorientation are expected to depend on fluctuations of the positional coordinates of the environment. Therefore, the rate of proton transfer and of breaking the hydrogen bond is expected to be affected by fluctuations of the O$\cdots$O separation. The weakness of the hydrogen bond makes it sensitive to the coupling with the environment so favouring pattern of hydrogen bond networks [8]; in the extreme cases, this patterning could result in a totally disordered or totally ordered network in which the number of sites is reduced to the number of protons.

To establish proton transport over macroscopic distances, all the elements involved in the transport process have to cooperate in order to produce an uninterrupted proton-transport trajectory. The problem is that the elementary reactions may conflict due to their coupling with the environment. Short hydrogen bonds allow proton transfer between adjacent donor and acceptor species but deny the possibility of diffusion, rotation, and reorientation of the involved moieties, whereas weak hydrogen bondings favour the opposite behaviour. Good proton-conducting phases usually don't show strong hydrogen bonding. In any case, thermal fluctuations of the protonated structure let the system pass through configurations assisting proton hopping, to configurations in which hydrogen bonds are weakened, so allowing structural relaxation.

The modes involved in the solvent rearrangement contribute to the self-localization of the proton at one side of the hydrogen bond; on the other hand, they contribute to the formation of a proton diffusion trajectory. In this sense, non polar compounds with big, rigid anions are among the best proton conductors. Rigid anions give only small contributions to the solvent

effect because they efficiently separate neighbouring hydrogen bonds by their large size, this diminishing the mutual polarization of neighbouring hydrogen bonds. In this way, proton disorder provides an isotropic environment that minimizes the barrier for the reorientation of these anions, averaging solvent effects and supporting conduction through Grotthuss mechanism.

## 1.3 Protonic Conductors

Protonic conductors, in general, are electrolytic materials able to sustain protonic transport, through which hydrogen migrates from the anode to the cathode during electrolysis. Using this definition, protonic conductors are those compounds in which electric conduction is realized by protonic species whose charge is positive - i.e. the bare proton, the hydronium ion, ammonium ion ($H^+$, $H_3O^+$, $NH_4^+$), or any other species that can be considered a protonic carrier like the $HS^-$ ion.

Classification of protonic conductors can be done according different parameters: *i)* working temperature, *ii*) method of synthesis, *iii*) nature of the compound, by dividing them, as a first attempt, in organic and inorganic ones. Water contents, its physical phase, the presence and the amount of proton excess allow a further subdivision of the proton conducting materials.

Several protonic conductors are characterized by the presence of domains in which liquid water is present; these are considered *two-phases systems*. An example of these systems are polymeric membranes, having a perfluorinated backbone and side chains terminated by acidic $-SO_3H$ groups, heteropolyacids or acidic phosphonates [8]. These materials must be hydrated in order to establish an equilibrium between protons and water molecules ($H_2O \leftrightharpoons H_3O^+$), assuring the protonic transport. Protons are inserted into the polymeric structure through ionic exchange of alkaline cations. The high protonic conduction, in these systems, is mainly produced by the fast dynamic of the water molecules that are, in membranes, ideal protonic vehicles.

An other group of protonic conductors is formed by compounds characterized by the presence of crystallographic protons. Organic and inorganic hydrated compounds belong to this group. In these materials some oxygen atoms (oxide ion) are bound to two of three hydrogen atoms, or one single proton is present per each anion, like in the cesium hydrogen-sulphonate ($CsHSO_4$). Other examples are acidic salts, hydroxides, hydroxicarbonates and other protonated species. Formation of defects like protonic vacancy or interstitial protons is a necessary condition for the conduction in hydrated crystallines, acid or hydroxides. Structural defect are created mainly by thermal disorder changing the local stoichiometric ratio of the compound or by doping it with species with oxidation number different from the stoichiometric formal one. These materials here discussed have the disadvantage to

decompose themselves at temperatures higher than 373 K. The decomposing temperature is higher if the water contents is lower, but also lower, on the other hand, its protonic conducting efficiency.

A third protonic conductors group is formed by materials in which protons do not belong to the structure, but are present as defects acquired when materials are synthesized or after absorption of hydrogen or water from the atmosphere in which they are. These materials are able to tolerate high temperatures or dehydration treatments, without fundamental structural alterations. In these materials, one proton is incorporated into interstitial sites and its mobility does not depend overall on native defects. The ability to acquire protonic defects may be improved by doping the compound with ions that promote the creation of defects like oxygen vacancies. Therefore, several studies are addressed to the investigation of the equilibrium that involve water vapour, protons and structural vacancies in the compound. A large number of structures, called High Temperature Protonic Conductors (HTPC), such as perovskitic compounds with general stoichiometry X:$ABO_3$ (i.e Y:$BaZrO_3$) or complex perovskites like $Ba_3(CaNb_2)O_9$, and other similar structures (i.e. $Ba_2In_2O_5$ brownmillerite[12]) belong to this class.

## 1.4 General Properties of Protonic Conductors

Each of the classes of compounds above mentioned is represented by those conductors that have a maximum conductivity in the range of $10^{-3} - 10^{-2}$ S/cm as a function of temperature. These values are characteristic of the specific material and can undergo variation after physical treatments: at high temperature, conductivity decreases due to reversible or unreversible water loss (polymeric compounds), due to decomposition of the material (hydroxides or acidic salts) or due to reversible loss of protons in the case of the oxides. On the other hand, high temperatures are required, in general, to get good conductivity values. In general, protonic conductors have their largest yield in a narrow temperature range.

In the Arrhenius diagram of Figure 1.2, conductivity curves of some substances, representative of each class, are shown as a function of the working temperature [8, 13, 14, 15]. From the analysis of the figure, it is possible to observe that the high conductivity of the hydrated NAFION® polymeric membrane, at about 400K, is comparable with that of an aqueous solution of HCl 1M; beyond that temperature, the material starts to dehydrate. In the same figure, conductivity curve of $CsHSO_4$ is reported, representative of systems with crystallographic protons: it behaves as fast proton conductor round 440K; on the other hand, it melt at a temperature of about 500K. At last, some phosphates and oxides show a good conductivity up to 900K. At higher temperatures, their protonic conductivity usually reaches a maximum

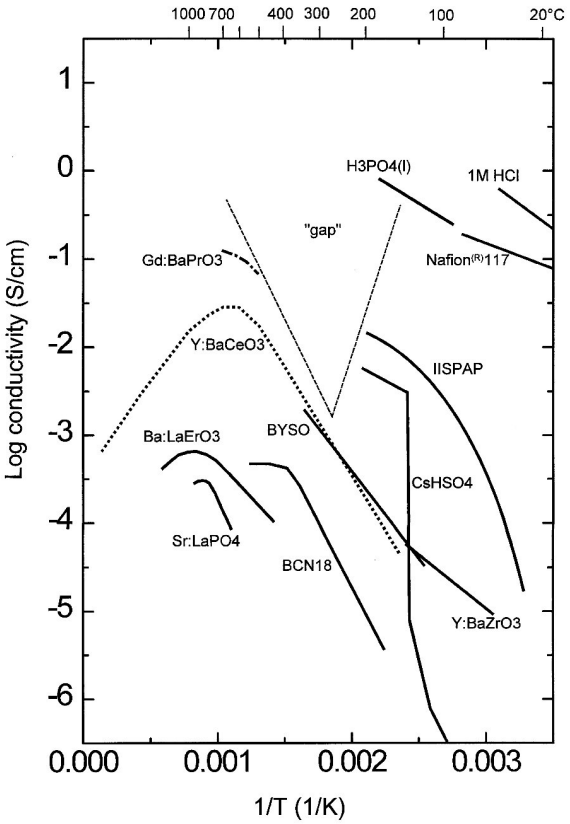


Figure 1.2: Conductivity data for different kind of protonic conductors as reported in [13] (redrawn).

and then decreases after protonic defect loss. Data available for $Ba_2YSnO_{5.5}$ [13] and for Y:$BaZrO_3$ [15] show that conductivity of these materials is similar to that of $BaCeO_3$ compound at low temperature. Furthermore, data related to mixed perovskite Ba:$LaErO_3$ [16] and to Sr:$LaPO_4$ [17], show that their related curves raises up to a maximum conductivity value without being this a significant conductivity improvement.

Polymeric membranes are used in various industrial processes for their fair good conductivity and technological features, but their major drawbacks are that their damage in extreme chemical environment or at high temperatures; furthermore, in many application like hydrogen separation, gases must be cooled and then reheated, an energy expensive process, obtaining a low purity gas at flux rates suitable for industrial purposes [18]. Some crystalline compounds with crystallographic protons, like $CsHSO_4$, have the tendency to lose the hydration water with increasing temperature; it is then necessary to increase the pressure to keep the conductivity at rel-

atively high values. Alternatively, other similar compounds like zirconium sulfoaryl phosphonates show that a high hydration of the compound tends to level the acidic strengths of the sulfonic group, thus determining its full dissociation. Substitution of the $-SO_3H$ group with thermally more stable acid groups (i.e. phosphobic acid group) lead to protonic conductors stable up to 580 K [19]. At temperature higher than 700K, High Temperature Protonic Conductors family of materials shows pronounced proton conducting properties; notwithstanding their valuable feature of working at high temperatures, they still suffer from chemical degradation against acidic gases, such as $CO_2$ and $SO_2$, that can be present in the reaction environment[20].

## 1.5 Solid Oxide Protonic Conductors

In the early 1980s, Iwahara and co-workers demonstrated that proton conductivity occurs in doped $SrZrO_3$ and $SrCeO_3$ [21, 22] perovskite compounds, attracting great interest towards $ABO_3$ perovskite materials because of their potential as electrolyte materials in several electrochemical devices [23, 24]. Since then, this kind of ceramic oxides gained great interest, proposing themselves as promising materials for their chemical stabilities along with high proton conductivity [13, 20, 23].

A ceramic protonic conductor is a solid solution whose structure is, usually, of perovskite type. Strictly speaking, with the term *perovskite*[†] it is named the calcium titanate mineral with $CaTiO_3$ as structural formula; however, all mixed oxides with isomorphic structure are also called with the name *perovskite*.

A crystal of perovskitic type has structural formula $ABX_3$. In this, A and B are positive ions while X is a generic negative ion. The ideal perovskitic structure is made by octahedra formed by oxygen atoms lying on the vertices like shown in Figure 1.3[‡].

The symmetry group of the ideal perovskite structure is $Pm\bar{3}m$. The axes formed by B−X octahedral bonds can be taken as the crystallographic ones. A solid oxide of perovskitic type has seldom the ideal structure just described; more often, according to several kinds of A, B and X cations and anions, the structure show distortions with respect to the cubic symmetry [25].

In order that protonic conduction can occur, hydrogen atoms must be incorporated into material structures. This can be usually accomplished by a two-step procedure. In the first step, a certain amount of tetravalent B atoms are substituted by trivalent species. In this way, one oxygen vacancy

[†] *Perovskite* is named after a Russian mineralogist, Count Lev Aleksevich von Perovski, who was appointed Russian secretary of the internal affairs in 1842 [25].

[‡] All the figures concerning molecular structures reported in this work have been realized with the help of VESTA [26] and Gimp [27] softwares.

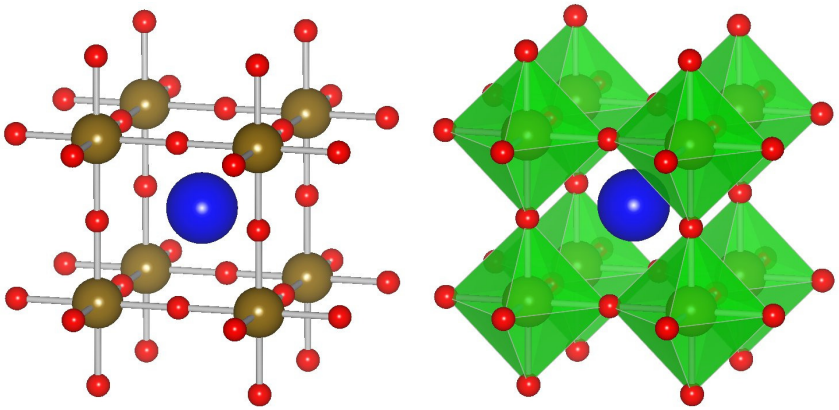

(a) (b)

Figure 1.3: Ideal cubic perovskite structure. The blue and brown spheres represent the position of the A and B cations respectively, while the red spheres indicate the position of the X anions.

per couple of doping cations is introduced in the material. In the second step, water vapour is steamed on the doped material producing structural O−H groups. In this sense, water adsorption is a dissociative process producing acidic centres (i.e. mobile protons) that is schematically represented by using the Kröger-Vink notation[§]:

$$H_2O_{(g)} + V_O^{\bullet\bullet} + O_O^X \leftrightarrows 2OH_O^{\bullet}. \tag{1.2}$$

In this way, protons are introduced into the host matrix and hydrogen diffusion, occurring through adjacent oxygen atoms [8, 28], may arise [29, 30]. As a consequence, local distortions involving doped B-sites [12] affect the proton environment, strongly influencing the mechanism of protonic conduction. Therefore, the study of the doped sites and their surrounding becomes of crucial importance in rationalizing local conduction details [29].

Although the substitution of tetravalent cation is the starting point to incorporate protonic defects into perovskite structures, it seems that it can reduce the proton mobility, as seen, for example, in proton conductivity measurements on $BaZrO_3$ where the activation energy for proton hopping is strongly dependent on dopant species [31]. Moreover, dopants can act as local "traps" for the protons, further affecting their mobility and their migration activation energy [32, 33, 34, 35, 36]

Ceramic protonic conductors of perovskitic kind, if put into atmosphere

[§]In Kröger-Vink notation $X_a^b$ means that the defect $X$ with charge $b$ substitutes for the element $a$; the charge $b$ is indicated with $'$ if positive, $^x$ if null, $^\bullet$ if negative.

containing hydrogen at temperatures round 1000K, show a drop of electronic conductivity and the appearance of protonic transport phenomena [23]. In these experimental conditions, typical conductivity values are of the order of $10^{-2}$ S/cm. In these oxides the protonic conduction phenomenon in these oxides has been verified through experiments on the electrochemical transport of hydrogen in atmosphere containing hydrogen or water vapour at high temperature[22, 37]. Some doped zirconates like calcium, strontium and barium ones, ($CaZrO_3$,$SrZrO_3$ and $BaZrO_3$), show hydration and successive appearance of the protonic conduction phenomenon at high temperature[15, 38]. However, the related conductivity values are one magnitude order lower than those characteristic of the cerium perovskitic compounds. Among the mentioned oxides, ceramic compounds $BaCeO_3$ derived show the highest conductivity values; on the other hand, zirconates hardly react in acidic environment and are stable in carbon dioxide $CO_2$ containing environments, unlike the cerate compounds that already a temperatures lower than 1000K start to form carbonates [20].

## 1.6 Technological Applications of Ceramic Protonic Conductors

Ceramic protonic conductors can be used as electromotive force (e.m.f.) generators or as electrochemical carrier of hydrogen in solids. In some kinds of galvanic cells, the solid oxide works as an electrolyte. If the e.m.f. of the cell is used as indicator of the hydrogen chemical potential, the corresponding device is called *activity sensor*; if the power produced by the cell is used, the device is called *fuel cell* [23]. As underlined in the previous sections, an important function of the protonic conductors is the hydrogen transport, based on the migration of the proton from a chemical species to an other one inside the solid oxide. This feature can be applied in devices called *hydrogen pumps*, that have the aim of separating and extract hydrogen from gas mixtures. Protonic conductors can also work as electrolysers if used for extracting hydrogen atoms from compounds like water or other chemical species that contain hydrogen.

Other possible applications of the protonic conductors as solid state electrolyte materials are listed in Table 1.1.

**Hydrogen Gas Sensors.** A proton concentration difference between two sides of a diaphragm, made by a protonic conductor, generates an electromotive force ($EMF$). This is a kind of hydrogen concentration cell in which the $EMF$ calculated is proportional to the logarithm of the ratio of the hydrogen partial pressures at the two sides of the membrane.

If both pressures values are known, the $EMF$ electromotive force is a measure of the hydrogen activity. In this electrochemical cell, the electrode

Table 1.1: Devices using High Temperature Proton Conducting solid electrolytes.

| Function | Applicability | Devices |
|---|---|---|
| EMF | Power | Fuel Cells |
| | Signal | Steam sensor |
| | | Hydrogen sensor for molten metals |
| | | Hydrogen gas sensor |
| | | Hydrocarbons sensor |
| | | $H^+-D^+$ isotope sensor |
| Electrochemical permeation | Electrolysis | Steam electrolyser for hydrogen production |
| | | $H_2S$ electrolyser for desulfurization |
| | | HCl electrolyser for $Cl_2$ recovery |
| | | Electrolyser for NOx removal |
| | | Electrolyser for tritium cycle |
| | Separation | Hydrogen extractor |
| | | Hydrogen pump for tritium cycle |
| | | Regulator of hydrogen gas pressure |
| | | Steam pump |
| | | Isotope concentrator |
| | Reaction | Membrane reactors for hydrogenation and dehydrogenation of organic compounds |

with the higher partial hydrogen pressure is the negative one.

Hydrogen sensors of this kind have been examined using test cells in which the electrolytic material is made by ceramic conductor derived by $SrCeO_3$, $BaCeO_3$ and $CaZrO_3$[39, 40, 41]. This kind of cell generates a stable and reproducible e.m.f.; the response is fairly fast (it needs about 20 s for the $EMF$ reaching the 90% of the theoretical value) and the trend of the electromotive force is in a good agreement with the expected values [39].

In order to individuate a standard, among systems analogous to those here described, several kind of solids have been examined [42]. A good candidate seems to be a mixture of aluminium phosphate ($AlPO_4$), partially hydrated, and lantanium cobaltite ($LaCoO_3$).

This kind of sensors can also be used at high temperature, to individuate the presence of water vapour or gaseous hydrocarbons [43].

**Hydrogen Sensors for Melted Metals.** Sensors of this kind use indium-doped calcium zirconate compounds (i.e. $CaZr_{0.9}In_{0.1}O_{2.95}$) and have porous platinum electrodes. The gaseous phase comes into contact with melted aluminium at about 1000K and hydrogen chemical potential in this phase is equal to the one relative to hydrogen content in the melted aluminium. Knowing the EMF of the cell with a fixed hydrogen concentration, it is

possible to know the hydrogen partial pressure, thus the amount of hydrogen present in the aluminium.

The usefulness of a fair accurate measure of the presence of hydrogen in metals lies in the increasing demand of metallic material with a high purity degree. This kind of sensors can also be used with elements like zinc or copper. In the case of copper, aluminium compounds are preferable because of their stability at high temperature, even if their conductivity is not so high[44].

The problem with this devices is the difficulty of finding materials to be used as standard for the reference hydrogen partial pressure in the sensor, because of their instability at high temperatures.

**Hydrogen Isotope Sensors.** The structure of a device able to reveal the presence of hydrogen isotopes is similar to a concentration cell for the protium. The sensitive element is always a ceramic protonic conductor: if on one side of the membrane protium is introduced while on the other one deuterium is present, the cell generates a stable and reproducible electromotive force [23]. An important relation that connects the *EMF* generated by the cell to the other main physical quantities is the following equation:

$$EMF \propto \ln \frac{\frac{u_H}{\gamma_h} p_{H_2,I}^{'1/2} + \frac{u_D}{\gamma_D} p_{D_2,I}^{'1/2} \exp\left(\frac{-\Delta\mu}{2RT}\right)}{\frac{u_H}{\gamma_h} p_{H_2,II}^{'1/2} + \frac{u_D}{\gamma_D} p_{D_2,II}^{'1/2} \exp\left(\frac{-\Delta\mu}{2RT}\right)} \tag{1.3}$$

where

$$\Delta\mu = \left(2\mu_D^0 - \mu_{D_2}^0\right) - \left(2\mu_H^0 - \mu_{H_2}^0\right) \tag{1.4}$$

and $\mu^0$, $p$, $\gamma$, $u$ are, respectively, the standard chemical potential, the partial pressure, the activity coefficient and the mobility of the species specified by subscript (H for protium and D for deuterium) $p_{H_2}^{'}$ and $p_{D_2}^{'}$ are the partial pressures of $H_2$ and $D_2$ in equilibrium while roman numbers distinguish between the two sides of the cells [45]. The validity of the equation 1.3 has not been completely verified because it is difficult to determine the quantity $\Delta\mu$, since the measure of the standard potential of protium and deuterium in the electrolyte is not easy. However, once the temperature and the kind of electrolyte are fixed, the Equation 1.3 reproduce the trend of the *EMF* with a unique $\Delta\mu$ value for the different kind of cells for the hydrogen isotopes. Indeed, it was shown that $EMF$ depends linearly on the $D_2$ concentration, if a mixture of protium and deuterium is used. This feature can be used to measure the concentration of hydrogen isotopic species in systems used in nuclear fusion processes [45].

**Hydrogen Pumps.** Hydrogen is the main species carried in protonic conductors. Thanks to this feature, it is possible to use ceramic protonic conductors to separate hydrogen from other moieties in a gas mixture. A system qualified to this aim is called *hydrogen pump*.

A hydrogen pump can also extract hydrogen from compounds in which it is present like $H_2O$ and $H_2S$; in this case, the device works as an electrolyser. Several research group have studied these systems and their performances [31, 46, 47, 48, 49, 50]. Recently, it has been found that the hydrogen amount carried by ceramic electrolytes derived from $SrCeO_3$, grows in a drastic way when a few percentages of water vapour is present [51]. However, separation rate is still relatively low to use these devices in systems for energy production.

**Solid Electrolyte Membrane Reactors.** A generic solid electrolyte membrane reactor (SEMR) is made, in a schematic picture, by a membrane separating two reaction chambers. This membrane has the role to transfer at least one reactant or one product from one side to the other of the reactor with the advantage that a single device is able to trigger a reaction (acting like a catalyst) and to separate the related components (reactant and products)[52].

Solid oxide ceramic membranes belong to the general category of inorganic dense membranes. On both sides of a membrane two porous electrodes are deposited; at high temperatures, selective permeation of only one ionic species like $O^{2-}$, $H^+$, $Na^+$ or $Li^+$ is allowed. The SEMR are devices similar to fuel cells, thus they can be exploited to produce electric energy or chemical energy; in literature, applications like catalysts are also reported [53, 54, 55, 56, 57, 58, 59, 60, 61].

A SEMR is mainly made by a solid state electrolyte membrane (that, in the most of cases, carries $O^{2-}$ or $H^+$), on the sides of which two porous electrodes are deposited. A counter electrode and reference electrodes are exposed to gas mixtures containing oxygen or hydrogen, while the load electrode is exposed to the reactant mixture and serves also as catalyst of the chemical reaction. If the hydrogen or oxygen chemical potential is different in the two chambers separated by the membrane, a drift force is generated which allows to the ionic species $O^{2-]}$ or $H^+$ to cross the lattice structure of the electrolyte. The appearance of a current or of a potential difference between the electrodes is associated to this process.

This kind of cell can act as: *i)* electrochemical sensor — cell potential depends on the concentration of compounds present on both sides of the membrane [62]; *ii)* fuel cell — the free reaction energy is directly converted into electric energy, overcoming the thermodynamic limitations of the conventional thermal engines [63, 64]; *iii)* reactor in which catalytic activity is modified to get higher conversion rates [61, 65]. Other interesting ap-

plications are solid state batteries [60], oxygen separators and dehumidifier [22].

The common feature to almost all the kind of SEMRs is that of carrying only one chemical species, let them be used to separate oxygen from the nitrogen in the air or for hydrogen production. In the first case, if the cathode is exposed to the air or to some mixture containing oxygen, only this last one is usually transferred through the electrolyte. This diminishes the volumetric flux of the reactants; furthermore, presence of impurities that can inhibit the catalysis are avoided [60].

It has experimentally shown that oxygen electrochemical contribution to the membrane electrodes can change and eventually improve reaction conversion rates, modifying selectivity and removing unwanted processes like coke formation [66, 67]. Similarly, an equilibrium shifting of hydrogenation reactions has been observed if hydrogen develops at the electrodes [68].

SEMRs can also operate as devices in which the production of chemical reactants is coupled with energy production. Keeping a concentration difference between active species on one side and on the other of the membrane, it is possible, to produce electric energy and, at the same time, to increase the reaction conversion rate [61, 69].

## 1.7 The Key-role of the Protonic Conductors for a Sustainable Development.

Constant demographic growth and continuous technological worldwide development coincide with constant increase of energy demand; the reached growth level and its consequences made indispensable an evaluation of the future availability of energetic stocks sufficient for sustaining the global growth. So, we got the concept of *Sustainable Development*, a body of relationships among human activities and biosphere in which they take place. Such relationships should assure the current needs without compromising that future generations will do the same[¶].

Table 1.2 compares the consumption of different energy forms, expressed as million tonnes of oil equivalent (MTOE)[‖], with the world population and the per capita energy use in the years between 1900 and 1997 [70, 71, 72].

The quick development of industries and transports, together with an improvement of life standard corresponds to an energy consumption growth from 911 MTOE in the year 1900 to 9647 MTOE of the 1997. This growth of energy request is due to only partially to the rapid growth of world population from 1762 to 5847 million people in the here considered period.

[¶]The first definition of *Sustainable Development* was given in the Brundtland report of the 42th General Assembly of the ONU in 1987.

[‖]A ton of oil equivalent corresponds to about 42 GJ.

Table 1.2: Worldwide energy use in million tonnes of oil equivalent (MTOE), world population and per capita energy consumption in the 20th century [70].

| Energy source | 1900 | | 1997 | |
|---|---|---|---|---|
| | MTOE | % | MTOE | % |
| Petroleum | 18 | 2 | 2940 | 30 |
| Natural gas | 9 | 1 | 2173 | 23 |
| Coal | 501 | 55 | 2122 | 22 |
| Nuclear | 0 | 0 | 579 | 6 |
| Renewable | 383 | 42 | 1833 | 19 |
| Total | 911 | 100 | 9647 | 100 |
| Population (million) | 1762 | | 5847 | |
| Per capita energy use (TOE) | 0.517 | | 1.649 | |
| Global $CO_2$ emission from fossil fuels (MMTC) | 534 | | 6601 | |
| Per capita $CO_2$ emission (MTC) | 0.3 | | 1.13 | |
| Atmospheric $CO_2$ (ppmv) | 295 | | 364 | |
| Life expectancy (years) | 47 | | 76 | |

The same table shows also data on $CO_2$ emissions; these have grown more than one order of magnitude in almost 100 years, to coincide with the increase of fossil fuels consumption. In order to control overall greenhouse gases emission, interventions of different kind are necessary, such as energetic efficiency improvement, use of fuels with low carbon content and carbon dioxide sequestration in geological formations.

A representative example of the balance between energy supply and demand in western society is given by the United States situation. Figure 1.4 shows a summary diagram of such situation.

USA energetic system is mainly based on fossil fuels use, that constitute the 58.92% of the primary energy sources; renewable energy sources are only the 6.87% of used resources. The 33.64% of the energy coming from primary energy sources is used to produce electric energy; more than the 65% of this energy is lost in conversion processes, due to the thermodynamic limits imposed by the Second Law [70].

From this rough outline, it is clear that the target of sustainable development of the energetic system is to develop highly efficient production energy devices using low environmental impact processes. The efficiency of actual transformation energy systems is not satisfactory, because more than 60% of initial energy is lost in conversion processes. Moreover, from an environmental point of view, the use of fossil fuels implies the emission of pollutants, such as $SO_x$ and $NO_x$, that are involved in the formation of the greenhouse gases. Nowadays, polluting substances are partially retained in purification plants, but the total elimination is guaranteed if they are absent in the starting fuels. Within these problems sketched since now, *fuel cells*

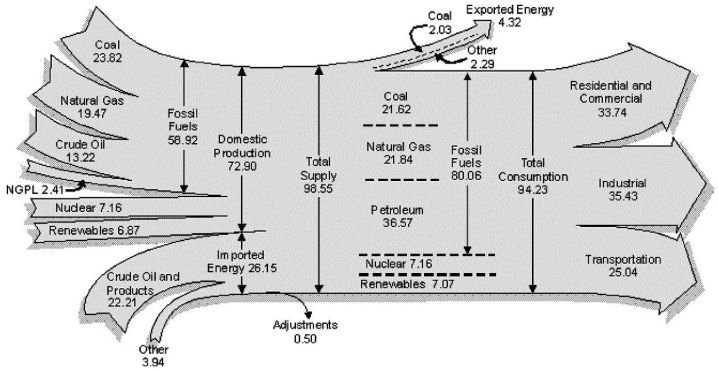


Figure 1.4: USA energy flux (quadrillion Btu) in the United States in 1998. Diagram redrawn from [70].

represent a good candidate as efficient energy conversion devices.

**General Features of a Fuel Cell.** The working principles of the fuel cells were first discovered by Sir William R. Groove, in 1839, a British jurist and physicist. Groove used hydrogen and oxygen as fuels, catalysed on platinum electrodes [73].

A fuel cell is an electrochemical device in which chemical energy stored in the fuel is directly converted into electric current. It is made by a material of electrolytic nature, able to produce ionic transport, inserted between anode and cathode; these come into contact, respectively, with a fuel — containing, in general, hydrogen atoms, and with an oxidizing agent, usually oxygen. Some atoms separate from the fuel becoming ions and cross the electrolyte reaching the cathode, where they will recombine with the oxidant; at the same time, free electrons are generated and from the anode reach the cathode through an external electric circuit. The products of the whole reaction are heat and water (liquid or vapour), eventually $CO_2$ if the fuel is a hydrocarbon. An essential feature of the electrolytic conductors used in fuel cells is that they must be poor electric conductors and good ionic conductors, both for activity and selectivity, in order to promote chemical reactions required for the optimum cell work.

The amount of current produced depends on the chemical activity of the reactants and on the power loss inside the cell; the production process, furthermore, continues until reactants are present. The electrodes and the electrolyte are chosen in such a way that they do not participate to the global reaction. A fuel cell can generate an e.m.f. of about 0.5-0.9 V; high e.m.f. can be reached making a series of many single cells.

**Efficiency of Fuel Cells.** Conversion energy efficiency in fuel cells can be examined by considering their maximum theoretical efficiency [74]. Limit efficiency $\eta_{Carnot}$ for engines based on heat exchange, such as those ones with steam turbines, is described by Carnot formula

$$\eta_{Carnot} = \frac{T_2 - T_1}{T_2} \tag{1.5}$$

where $T_2$ is the temperature (higher) of the heat source and $T_1$ is that one (lower) at which steam is released. For a steam turbine, operating at 400 °C with a condensation temperature of 50 °C, the limit efficiency is of 52%. This value is quite far to be reached if the steam, as it happens in the most of cases, is obtained burning fossils fuels. The situation is different for fuel cells, that are based on chemical processes, such as hydrogen oxidation and water formation. The variation of Gibbs free energy $\Delta G$ of these last processes is converted into electric energy. The e.m.f. of the cell, in the following equation represented as $\Delta U_0$, is related to the free energy by the equation

$$\Delta G = -nF\Delta U_0 \tag{1.6}$$

where $n$ is the number of electron involved in the reaction, $F$ is the Faraday constant and $\Delta U_0$ the potential difference of the cell at the thermodynamic equilibrium without any current flux [75]. If the fuel is hydrogen and the oxidizing agent is oxygen, $\Delta U_0 = 1.23V$ corresponding to $\Delta G = -237kJ/mol$ for the whole reaction in standard conditions

$$H_2 + \frac{1}{2}O_2 \rightarrow H_2O. \tag{1.7}$$

Efficiency $\eta_{fuelcell}$ can be calculated directly as

$$\eta_{fuelcell} = \frac{\Delta G}{-\Delta H} \tag{1.8}$$

where $\Delta H$ values change according to the water phase: $\Delta H$ is higher for liquid water because of condensation heat release. If water vapour is created, $\Delta H = -286kJ/mol$ and the maximum efficiency of the fuel cell would be 83%.

**Kind of Fuel Cells.** Fuel cells can be distinguished according to the kind of electrolyte used. A rough classification is the following: *i*) alkaline (Alkaline Fuel Cell), *ii*) with phosphoric acid (Phosphoric Acid Fuel Cell), *iii*) with melted carbonate salts (Molten Carbonate Fuel Cell) *iv*) with solid oxide (Solid Oxide Fuel Cell). Each kind of cell is characterized by different reactions that take place at the anode and cathode due to the transport of ionic species that generate an electric current flowing in an external circuit.

A common feature is that electrodes must be porous in order that gases can reach the electrode and the electrolyte at the same time. Main features of the four kind of fuel cells are reported in [70].

Fuel cells in which the electrolyte element is of solid oxide type, show the highest efficiency and stability. The electrolyte of SOFCs is of ceramic type; this reduces corrosion effects at the electrodes and eliminates those problems present in the cells in which the electrolyte is at liquid phase. In order to get a suitable ionic conductivity, the working temperature of these systems must be in the range between 1150 and 1300 K. The most used electrolyte in these cells is the yttrium oxide ($Y_2O_3$) stabilized with zirconium oxide ($ZrO_2$); the anode is usually a *cermet*** of nickel-zirconium ($Ni-ZrO_2$) or cobalt-zirconium ($Co-ZrO_2$), while the cathode is made by magnesium or strontium doped with lanthanum manganate ($LaMnO_3$).

The heat produced by the cells during the conversion of the chemical energy into electric energy, can be easily used in conventional thermal plants for electric energy production; on the other hand, because of the high working temperature, conditioning times needed by the system to reach the full load are long and it is necessary that the cell materials tolerate a big thermal stress. A solid state electrolyte makes easy to modify cell properties according to the logistic or technological needs [76].

Actual SOFCSs based plants can reach a power of 160 KW. The high working temperature (about 1300K) allows an enough wide choice of fuels with yields that can reach the 85% of the total thermal efficiency.

All fuel cells work without burning the fuel while the moving parts are few with respect to the conventional units for electric energy production (mechanical generators); furthermore, they are three times more efficient than internal combustion engines and energy production continues until both fuel and oxidizing agent are present at the electrodes.

Thus the advantages of fuel cells are due to the following features:

- high efficiency in energy conversion;
- nearly zero emission of polluting agents;
- great reduction of greenhouse gases emission in comparison with conventional devices;
- very low acoustic pollution;
- simplicity of conversion processes from chemical to electric energy;
- modular project for large scale production;
- quick response to the load;

**A *cermet* is a compound made by ceramic and metal.

- different kind of fuel can be used.

Thanks to all these features, fuel cells can find application in industrial, commercial, residential plants, transport and portable electronic devices; therefore, such fuel cells are pointed as the most promising technology that can satisfy, for a long time, the energetic needs of a modern society.

Nevertheless, disadvantages and problems to be resolved are still a lot. The cost per kW in building energy conversion plants based on fuel cells are still high compared with ones of traditional plants; moreover, some kind of cells require hydrogen in gas phase, that must be produced in the same place where it will be used, because of the lack of a distribution system; at last, using hydrocarbons as fuel requires the presence of desulphurization plants, that are, in general, potential source of pollution.

# Chapter 2

# Computational Models and Data Analysis

The study of a physical system is usually carried out through experimental techniques that are based on the analysis of sample responses to external stimulations. It often happens, however, that we cannot manage and gauge external stimulations to address experiments towards a particular goal because the system under investigation is "unreachable", either because it is far from us like, for example, interstellar gases, or because we cannot control the details of the experiment as accurately as we need, like in studying atomic motions. In these cases, an alternative way of investigation is trying to recreate the system with a *virtual* model and simulate the experiment with a computer, that is to create a *virtual sample* and to perform a *virtual experiment* on it. In this sense, computer simulations are also called *in silico* experiments*.

Computer simulations are thus a complementary tool to understand experimental data, contributing to discriminate the different aspects of a physical phenomenon and are an aid in formulating predictions on system behaviours under different environmental conditions. Protonic conduction and the elementary processes that lie on it are an immediate example on how this quite recent "experimental technique" is of fundamental importance to obtain a clear survey of a physical phenomenon, in order to reproduce it and to design devices to exploit its potentialities.

In the following, among the several computational techniques nowadays available, only those ones used in the present study will be outlined, paying attention to informations that can be obtained, the related accuracy and how to get them.

*The expression *in silico* was first used in 1989 by Pedro Miramontes, a mathematician from National Autonomous University of Mexico (UNAM) [77].

## 2.1 Computational Models

A *computational model* consists, in general, in choosing a *geometry* that reproduces the atomic positions of the system under consideration and a *method*, that allows to calculate its properties, possibly able to refine the already existing structural representation. The set of atoms chosen to build the model can coincide exactly with the whole real system or, as it happens in most of cases (particularly if studied in solid state), it only represents the part we want to study in details. A method consists, in general, in the theory be applied in order to get the required informations. The choice of the model is strongly conditioned by the computational resources at own disposal: it is the result of a compromise among the accuracy of the desired results, the time required to get them and the power of the computational resources available.

The geometry chosen for describing the system under study is initially taken from experimental data. For systems in solid state phase, like the solid oxide barium cerate and zirconate in this work analysed, data usually come from Neutron Powder Diffraction (NPD) experiments or similar techniques able to individuate atomic positions. Starting geometries will be chosen among those ones obtained in the desired experimental conditions. As we stated in section 1.5, protonic conduction in solid oxides is possible only if protonic defects are acquired by the host matrix, but this is allowed only by doping the native material with trivalent species; so, we can already individuate at least three different starting geometries for three different situations: the undoped structure, the doped one and the protonated system. If we take into account the experimental structures resolved at different temperatures [78], the number of geometries to be considered starts to grow very quickly.

In studying a crystalline system, it is common practice [12, 79, 80, 81] to choose one unit cell or a block of $m \times n \times l$ unit cells (this block called a *supercell*, with $m$, $n$ and $l$ positive integers) to which apply Periodic Boundary Conditions (PBC). This is in order to reproduce the crystalline structure and to take account of more than one cation substitution or lattice defects. Other approaches [82, 83, 84], suggested by experimental evidences [85, 86], showed that, also for crystalline systems, a good starting point can be a set (*cluster*) of atoms extracted from the crystalline network, without imposing PBC on it. The choice between the two approaches is dictated by the system considered and by the details we want to inspect. Overall, starting geometries must contain at least the system's main area of interest and its nearest environment, in order to get a minimal representation; furthermore, the shape of the geometry must be chosen accurately in order to avoid cutoff truncation outcomes, greatly affecting the results.

The bigger is the model structure, the more accurately it reproduces the real system; unfortunately, the larger is the model geometry, the greater is

the computational load which, depending on the used method, it is proportional to powers of $N$, the number of atoms involved.

Once the model geometry has been established, a *computational method* must be chosen in order to describe the properties of the chosen structure. It can be a physical model that describes atoms as made by electrons surrounding a positively charged nucleus, or that considers them or group of them as owning some features typical of the environment in which they are embedded.

In the first case the model is the *Quantum Mechanic* description of the matter, and all the methods based on it are called *ab initio*. They lean on the Schröedinger equation

$$-i\hbar\frac{\partial}{\partial t}\Psi\left(\vec{r},t\right)=\hat{H}\left(\vec{r},t\right)\Psi\left(\vec{r},t\right) \tag{2.1}$$

where $\hat{H}\left(\vec{r},t\right)$ is the Hamiltonian energy functional operator of the system and $\Psi\left(\vec{r},t\right)$ is the wave function that describes the system at the time $t$ all over the physical space $\{\vec{r}\}$. Once $\Psi\left(\vec{r},t\right)$ has been determined − that is once the above equation has been resolved, it is possible to get any observable physical quantity $O$ related to the system through the corresponding operator $\hat{O}$, being

$$O=\langle\Psi\left(\vec{r},t\right)|\hat{O}|\Psi\left(\vec{r},t\right)\rangle \tag{2.2}$$

its expectation value in Dirac notation.

Actually, due to the complexity of the functional form of the Hamiltonian $\hat{H}$, the only system for which it is possible to exactly solve the Schröedinger equation is the hydrogen atom, taking into account only the coulombic interaction between its charged constituents, one proton and one electron. All the other single atomic species and all the systems deriving from interactions among some them, such as molecules, crystals or amorphous structures, always obeys to the equation 2.1 but its solution is carried out only by means of several approximations. First of all, in the most of cases, it is possible to assume that the energy is a constant of the system, so as to deal with a time independent Schröedinger equation

$$\hat{H}\left(\vec{r}\right)\Psi\left(\vec{r}\right)=E\Psi\left(\vec{r}\right), \tag{2.3}$$

with $\hat{H}$ the energy functional of the system including only kinetic and electrostatic terms of point-like nucleus and electrons:

$$\hat{H}=\sum_{\alpha}\frac{P_{\alpha}^{2}}{2M_{\alpha}}+\sum_{i}\frac{p_{i}^{2}}{2m}+V\left(Q_{\alpha},q_{i}\right) \tag{2.4}$$

where $P_\alpha$ and $p_i$ are the momentum operators of the $\alpha$-th nucleus and of the $i$-th electron respectively, $M_\alpha$ and $m$ are the mass of the $\alpha$-th nucleus

and of the electron, and

$$V\left(Q_\alpha, q_i\right) = -\sum_{i,\alpha} \frac{Z_\alpha e^2}{r_{i\alpha}} + \sum_{\alpha<\beta} \frac{Z_\alpha Z_\beta e^2}{r_{\alpha\beta}} + \sum_{i<j} \frac{e^2}{r_{ij}} \tag{2.5}$$

is the potential energy operator of the entire system of nucleus and electrons. Then, an other strong approximation, usually made in dealing with solid state systems, is the one first proposed by Max Born and Robert Oppenheimer [9], taking advantage of the difference between nuclear and electron masses, in order to separate the nuclear motion from the electronic one. In this approximation, nuclei are supposed to be fixed in their initial position $Q'_\alpha$; then equation 2.3 is solved in its simplified form

$$\left[\sum_i \frac{p_i^2}{2m} + V\left(Q'_\alpha, q_i\right)\right] \psi\left(Q'_\alpha, q_i\right) = E'\left(Q'_\alpha\right) \psi\left(Q'_\alpha, q_i\right). \tag{2.6}$$

Eigenfunction $\psi\left(Q'_\alpha, q_i\right)$ is an electronic wave function while $E'\left(Q'_\alpha\right)$ is the corresponding eigenvalue when the nuclei are fixed in the position $Q'_\alpha$.

A further assumption is to set

$$\Psi\left(Q_\alpha, q_i\right) = \psi\left(Q_\alpha, q_i\right) \nu\left(Q_\alpha\right) \tag{2.7}$$

that is, the wave function is supposed to be a product between an electronic wave function $\psi\left(Q_\alpha, q_i\right)$ and a $\nu\left(Q_\alpha\right)$ function of only nuclear positions to be determined.

Despite the potential energy operator 2.5 contains only coulombic terms, an atomic description by means of the first principles of the quantum mechanics can assure good results. However, model geometries with a large number of atoms can involve a heavy computational load in terms of resources and time needed for the calculation[†]. In this case, a good choice is to substitute the quantum description of the system 2.3 with a completely classical one. This choice establishes a second class of computational methods: interactions among $N$ particles, atoms or groups of them, are described with a potential $V\left(\vec{r}_1, \ldots, \vec{r}_i, \ldots, \vec{r}_N\right)$, an analytic function of $3N$ coordinates, which takes into account interactions among two or more particles; the force acting on the $i$-th particle is then derived as the gradient of such potential with respect to the atomic positions:

$$\vec{F}_i = -\nabla V\left(\vec{r}_1, \ldots, \vec{r}_i, \ldots, \vec{r}_N\right). \tag{2.8}$$

Since $V\left(\vec{r}_i\right)$ is analytic, the $\vec{F}_i$ component values are straightforwardly derived. Obtaining the optimized geometry is in this case a simple iterative search of the $\vec{r}_i$ values for which all the $\vec{F}_i$ components are below a fixed

[†]To get an idea on how computational load depends on the number of atoms see, for example, I. N. Levine, *Quantum Chemistry*, 5th edition, (2000).

threshold. Also, by using relation 2.8 and Newton's second law of motion it is possible to get the evolution of the system as a function of time and calculate any required physical quantity (see section 2.4).

The expression for the potential $V$ in Equation 2.8 is usually derived *i*) starting from a quantum description of the system, obtaining an expression as a function of the nuclei position by means of successive approximations or *ii*) by fitting the potential on experimental data, without considering any relations with the first principles. In all cases, potentials are designed only for a limited set of systems, but sometimes they work well in situations far from those ones used for modelling them. The ability of a potential to properly describe different environments is called *transferability*; since a good transferability is difficult to get but it is a crucial point to get reliable results, it is better to use a potential only for those systems where they were designed on.

According to the features of the system we are studying and depending on informations we want to get from simulations on it, one or the other computational method is to be preferred, always keeping in mind the computational load required, the resources available and the time needed to get the desired results.

## 2.2 The Hartree-Fock Method

The simplest ab initio method used in calculations carried out in the present work is named *Hartree-Fock* method. To understand how it works, let us consider the time independent Schröedinger equation for a neutral atom with $N$ electrons:

$$\hat{H}\Psi\left(\vec{r}\right) \equiv \left\{ \sum_{i=1}^{N} \left[ \frac{p_i^2}{2m} - \frac{Ze^2}{r_i} \right] + \sum_{i<j}^{N} \frac{e^2}{r_{ij}} \right\} \Psi\left(\vec{r}\right) = E\Psi\left(\vec{r}\right) \tag{2.9}$$

in which we have neglected the relativistic terms. Let us suppose that the solution is of the following form:

$$\Psi\left(\vec{r}_1, \ldots, \vec{r}_N\right) = \frac{1}{\sqrt{N!}} \begin{vmatrix} \psi_1\left(\vec{r}_1\right) & \psi_2\left(\vec{r}_1\right) & \cdots & \psi_N\left(\vec{r}_1\right) \\ \psi_1\left(\vec{r}_2\right) & \psi_2\left(\vec{r}_2\right) & \cdots & \psi_N\left(\vec{r}_2\right) \\ \vdots & \vdots & \cdots & \vdots \\ \psi_1\left(\vec{r}_N\right) & \psi_2\left(\vec{r}_N\right) & \cdots & \psi_N\left(\vec{r}_N\right) \end{vmatrix} \tag{2.10}$$

such determinant is called *Slater determinant*; its elements $\psi_i\left(\vec{r}_j\right)$, called *atomic orbitals*, are functions of the $\vec{r}_j$ coordinate of the $j$-th electron, subject to the orthogonality condition

$$\left\langle \psi_i\left(\vec{r}_j\right) \middle| \psi_k\left(\vec{r}_j\right) \right\rangle = \delta_{ij} \tag{2.11}$$

with $\delta_{ij}$ the Kronecker delta and $\psi_i(\vec{r}_j)$ chosen so that they satisfy the variational principle

$$\delta\langle\Psi|H|\Psi\rangle = 0. \tag{2.12}$$

The choice of a solution as in 2.10 is called *Hartree-Fock* approach. Now, let us suppose that the Hamiltonian $\hat{H}$ in Equation 2.3 is the same as in 2.4 with $V$ chosen as in 2.5. With the same hypotheses as for the atomic case just considered, the tentative solution $\Psi(\vec{r}_1, \ldots, \vec{r}_N)$ of Equation 2.3 is built by using a set of function $\psi_i(\vec{r}_j)$, as in 2.10, this time called *molecular orbitals*, which have the following characteristics:

- a molecular orbital is an eigenfunction of a Hamiltonian functional made by one-electron operators and depends on the coordinates of only one electron;
- a molecular orbital is defined all over the space: it describes one electron with a non-zero probability to be everywhere in the space without being localized on any atoms of the molecules;
- it can represent the properties of at most two electrons according to the Pauli principle; the product of a molecular orbital with a spin function is called *molecular spin-orbital* and it can be occupied only by one electron;
- each molecular orbital belongs to an irreducible representation of the transformation group under which the Hamiltonian of the system is invariant.

A further simplifying hypothesis, first proposed by Roothan in 1951 [87], is to state that the molecular orbitals $\psi_i(\vec{r})$ can be expressed as *linear combination of atomic orbitals* (LCAO) $\phi_\mu$:

$$\psi_i = \sum_\mu c_{\mu i}\phi_\mu. \tag{2.13}$$

All the $\{\phi_\mu\}$ functions are called *basis set*; their analytical form is arbitrary and it is usually chosen according flexibility criteria in numerical implementations. The Roothan's assumption transformed the problem of solving differential equations into an algebraic equations system, known as *Self Consistent Field equations* (LCAO-SCF)[‡]. This simplification allows to search for solutions of the time indipendent Schröedinger equation starting from a tentative one like in 2.13, and refining the $c_{\mu i}$ coefficients through iterative methods, whose details can vary according to the way they are implemented, involving particular algorithms to drive the calculation to numerical convergence (see [88] as an example).

[‡]For a derivation of the Hartree-Fock method and the Roothan equations see, for example, M. Weissbluth, *Atoms and Molecules*, Academic Press, New York, (1978).

The choice of a Slater determinant like in 2.10 is a good starting point to build the solution of the Schröedinger equation for a multi-electron system; nonetheless, such determinant does not correspond to the exact eigenfunction of the ground state. According to the variational principle, the expectation value of the Hamiltonian $\hat{H}$ of the system (e.g. its energy), calculated on a trial wave function which is Slater determinant, will be surely higher than the lowest of its eigenvalues. This last one, within Born-Oppenheimer approximation and leaving out relativistic effects, is defined as the *exact energy* $E_0$ of the ground state [89]. By setting

$$E_{HF} = \langle \Psi_{Slater} | H | \Psi_{Slater} \rangle \tag{2.14}$$

in which $\Psi_{Slater}$ is a Slater determinant, we call *correlation energy* $E_C^{HF}$ the difference

$$E_C^{HF} = E_0 - E_{HF}, \tag{2.15}$$

that is a measure of the error introduced by adopting the Hartree-Fock scheme.

To take into account this energy term, several computational schemes have been developed that are able to better estimate the exact energy value with respect to the method discussed up to now, but heavily increasing the computational cost. Some of them can be considered as an evolution of the Hartree-Fock scheme, and this is why they are called *post-Hartree-Fock methods*; other methods approach the problem in a different way, by exploiting the Density Functional Theory (DFT).

## 2.3 The Density Functional Theory

An electronic wave function of $N$ electrons depends on $3N$ spatial and $N$ spin coordinates. The need of reducing the computational load required to calculate a wave function with $3N + N$ degrees of freedom, was the boost for elaborating methods that attain same results using a narrow number of variables. In 1964, Pierre Hoenberg and Walter Kohn [90] proved that, given a molecule in the non degenerate ground state, the molecular energy, the wave function and all the other electronic properties are uniquely determined by the probability electron density of the electronic ground state, as a function of only three spatial coordinates.

To explore the relation between electronic ground state wave function $\Psi(\vec{r}_1, \ldots, \vec{r}_n)$ and the corresponding probability density, let us consider the expression

$$|\Psi_0(\vec{r}_1, \ldots, \vec{r}_n)|^2 \, d\vec{r}_1 \cdot \ldots \cdot d\vec{r}_n; \tag{2.16}$$

this is the probability to find, at the same time, electron 1 in the volume element $d\vec{r}_1$, electron 2 in the volume element $d\vec{r}_2$ and so on. The probability

to find the $i$-th electron in a generic volume element $d\vec{r}_i$ is got by integrating Equation 2.16 on the other volume elements:

$$\int |\Psi_0(\vec{r}_1, \ldots, \vec{r}_n)|^2 \, d\vec{r}_1 d\vec{r}_2 \cdot \ldots \cdot d\vec{r}_{i-1}\vec{r}_{i+1} \cdot \ldots \cdot d\vec{r}_N; \tag{2.17}$$

this probability being the same for each of the $N$ electrons, the probability of finding an electron in a volume element is equal to $N$ times the 2.17. Therefore, the probability density $\rho_0(\vec{r})$ of finding an electron in a space point $\vec{r}$ is

$$\rho_0(\vec{r}) = N \int |\Psi_0(\vec{r}_1, \ldots, \vec{r}_n)|^2 \, d\vec{r}_1 d\vec{r}_2 \cdot \ldots \cdot d\vec{r}_{i-1}\vec{r}_{i+1} \cdot \ldots \cdot d\vec{r}_N. \tag{2.18}$$

Let us consider now an observable $O(\vec{r}_i)$, function only of the spatial coordinates of the $i$-th electron. The mean value of this function on the whole electronic ground state is

$$\begin{aligned} \langle \Psi_0 | \sum_{i=1}^{N} O(\vec{r}_i) | \Psi_0 \rangle &= \int \Psi_0^* \left[ \sum_{i=1}^{N} O(\vec{r}_i) \right] \Psi_0 d\vec{r}_1 \cdot \ldots \cdot d\vec{r}_N = \\ &= \sum_{i=1}^{N} \int |\Psi_0|^2 O(\vec{r}_i) \, d\vec{r}_1 \cdot \ldots \cdot d\vec{r}_N; \end{aligned} \tag{2.19}$$

since electrons are indistinguishable, each term of the sum in the last member of the 2.19 takes the same value; so

$$\langle \Psi_0 | \sum_{i=1}^{N} O(\vec{r}_i) | \Psi_0 \rangle = n \int |\Psi_0|^2 O(\vec{r}_1) \, d\vec{r}_1 \cdot \ldots \cdot d\vec{r}_N. \tag{2.20}$$

Remembering that $O(\vec{r}_1)$ depends only by $\vec{r}_1$, integration of 2.20 on all the other coordinates results in expression 2.18. Thus the expression 2.20 becomes

$$\langle \Psi_0 | \sum_{i=1}^{N} O(\vec{r}_i) | \Psi_0 \rangle = \int \rho(\vec{r}) \, O(\vec{r}) \, d\vec{r} \tag{2.21}$$

where the subscript was not specified because unnecessary. This result shows that any mean value of any observable can be calculated, as represented by a function of the spatial variables, once the electronic density $\rho(\vec{r})$ is known. This can be done without calculating the electronic wave function $\Psi_0$ of all the system.

Let us now consider the purely electronic Hamiltonian of a system:

$$\hat{H}_{el} = \sum_i \frac{P_i^2}{2m} + \sum_i \nu(\vec{r}_i) + \sum_j \sum_{i>j} \frac{e^2}{r_{ij}} \tag{2.22}$$

where

$$\nu\left(\vec{r}_i\right) = -\sum_{\alpha} \frac{Z_\alpha e^2}{r_{i\alpha}} \tag{2.23}$$

is the nuclear attraction energy, function of the distance $r_{i_\alpha}$ separating the $i$-th electron from the $\alpha$-th nucleus.The Hamiltonian 2.22 is written in the Born-Oppenheimer approximation; as a consequence, in the Schröedinger equation for the electronic wave function $\Psi_0$ of the system in the ground state

$$\hat{H}\Psi_0 = E_0\Psi_0 \tag{2.24}$$

the only variables are electronic coordinates, and the nuclear positions are only a parameter through the term $\nu\left(\vec{r}_i\right)$. In the Density Functional Theory, this term is considered as an *external potential* acting on the $i$-th electron. Once the number of electron and the external potential have been fixed, eigenvalues and eigenfunctions of the Hamiltonian 2.22 are unambiguously determined. Because Hoenberg and Kohn demonstrated that there is a bijective correspondence between the eigenfunction $\Psi_0$ and the probability density $\rho_0 = |\Psi_0|^2$ of the ground state, the electron probability density of the ground state determines the external potential. Consequently it also determines the Hamiltonian of the system, the wave function of the ground state, the energy $E_0$ and all the properties obtainable from it. The ground state energy $E_0$, thus, is a functional of the density:

$$\begin{aligned} E_0 &= \langle\Psi_0|\hat{H}|\Psi_0\rangle = \\ &= \bar{T}\left[\rho_0\left(\vec{r}\right)\right] + \int \rho_0\left(\vec{r}\right)\nu\left(\vec{r}\right)d\vec{r} + \bar{V}_{ee}\left[\rho_0\left(\vec{r}\right)\right] = \\ &= E_0\left[\rho_0\left(\vec{r}\right)\right] \end{aligned} \tag{2.25}$$

in which

$$\bar{T}\left[\rho_0\left(\vec{r}\right)\right] + \bar{V}_{ee}\left[\rho_0\left(\vec{r}\right)\right] \tag{2.26}$$

is a unknown functional of the density independent of the external potential.

In this way, Hoenberg and Kohn showed that all the properties of a system in the ground state can be determined without calculating the corresponding wave function. Nevertheless, they didn't show how to do it. The problem was resolved by W. Kohn and L. J. Sham in 1965 [91] who developed a way to calculate $\rho_0$ and, from it, the energy of the ground state; on the other hand, by using their method it is not possible to obtain exact results because the unknown potential 2.26 can be estimated only approximately. Over the years, several formulations have been proposed (Local Density Approximation, General Gradient Approximation and others [89]), also taking into account for the energy term in 2.15, each of them to be chosen always according to the reliability of the results for the system under consideration.

## 2.4 Molecular Dynamics

When details of the electronic structure are not important for our purposes and we need to look at the system only at a larger scale, a great opportunity is offered by *Molecular Dynamics* (MD) methods. These methods allow simulations on very large systems involving up to one million atoms (see for example [92]).

*Molecular Dynamics* is a computer simulation technique through which the time evolution of a set of interacting particles is described by integrating their equation of motion. Physical laws used are those of the classical mechanics, with the Newton's second law of motion the main one:

$$\vec{F}_i = m_i \vec{a}_i; \tag{2.27}$$

where $\vec{F}_i$ is the force acting on a particle with mass $m_i$, generating an acceleration $\vec{a}_i$. By integrating this equation for a system of $N$ particles, a trajectory in a $6N$-dimensional phase space is generated. According to statistical physics, physical quantities are represented by averages over an ensemble of configurations in the phase space: such configurations can be provided using trajectories obtained by a dynamical simulation. Such trajectories can be used if in the system studied is valid the ergodic hypothesis:

$$\langle O \rangle = \lim_{T \to +\infty} \frac{1}{T} \int_{t_0}^{t_0+T} O\left(\vec{r}(t), \vec{p}(t)\right) dt = \lim_{N_c \to +\infty} \frac{1}{N_c} \sum_{i=1}^{N_c} O_i\left(\vec{r}_i, \vec{p}_i\right) \tag{2.28}$$

stating that the time average value $\langle O \rangle$ of an observable $O$ is equivalent to the ensemble average of the same observable. Thus, ensemble averages can be calculated as an average over the $N_c$ configurations calculated in a dynamic simulation; i.e., to evaluate a physical quantity it is sufficient to do an arithmetic average of the instantaneous values assumed by that quantity during time evolution of the system. Since the equality in Equation 2.28 holds for a fully sampled phase space volume, we can expect that acceptable averages can be obtained in simulation of very long times. Due to the finite time span of simulations, it is then necessary to check if sampling is adequate and the system has reached equilibrium.

We can perform our simulations of isolated, thermal bath coupled or open systems (*microcanonical*, *canonical* and *grand canonical* systems respectively), depending on information we want to get and on the system we study; so, in addition to forces, an integration algorithm is able also to calculate and control other quantities at each dynamic step, such as temperature, volume and pressure. In any case, integration is based on *finite difference methods*, where simulation time is discretized in $N_c$ timesteps of width $\Delta t$.

Discretization and integration scheme itself introduce calculation errors; these can be grouped in: *i*) *truncation errors*, related to the accuracy of the

finite difference method, leaning generally on a truncated Taylor expansion, hence owning an intrinsic error; *ii*) *round-off errors*, related to the finite number of digits used to represent a number in a computer. Both errors can be reduced by decreasing $\Delta t$, at the expense of longer simulation times.

## 2.5 Data Analysis

Analysis of the ab initio results presented in this work are based on the inspection of the equilibrium geometry of the systems. Born-Oppenheimer approximation allows to calculate, in a simple manner, the force generated by a system of atoms on one of the nuclei belonging to the same system, deriving it directly from the classical potential 2.5. This result is known as *Hellmann-Feynman theorem* [93] and is of fundamental importance in the research of an equilibrium geometry starting from a given one. Indeed, such research is the result of an iterative procedure: once the computation of the electronic Hamiltonian eigenvalues is finished, nuclear positions $Q'_\alpha$ (see discussion on Equation 2.6) are varied by a finite quantity, and the forces acting on the nuclei are calculated; if the highest value among the force components on each nucleus is lower than a fixed threshold, then the geometry used for the force calculation is the stable one and the calculation has *converged*; otherwise, the procedure is repeated calculating the energy $E'(Q'_\alpha)$ corresponding to the new nuclear positions. This kind of research is called *geometrical optimization* and the stable geometry is said *optimized* [94]. Convergence criteria and algorithms to get it can be varied according to what we are interested to; generally, an atom can be considered laying in a stable position if the value of the force acting on it is equal or smaller than 0.02 eV/Å[§].

Structural informations can be better understood and enriched by electronic analysis of the optimized system. In the used approaches, ab initio calculations supply the ground state wave function written as linear combination of atomic orbitals belonging to the chosen basis set (see Equation 2.13). Analysis of atomic orbital contributions to each of the molecular orbital of the system (electronic population) allows obtaining several informations, as, for example, the electronic distribution on a particular atomic site. Among the schemes that have been proposed in literature [95, 96, 97, 98, 99, 100, 101, 102, 103, 104], only *Mulliken Population Analysis* and *C-Squared Population Analysis* will be presented, being the one used for our purposes.

[§]Geometries representing transition states of a reactions also satisfy these conditions; this notwithstanding, they are not stable points of the energy hypersurface. One of the methods to ensure that an optimized structure corresponds to a local minimum of the system energy is to evaluate the eigenvalues of the energy (Hessian matrix) in that point: a negative or an imaginary frequency states that such geometry is a transition state along the corresponding eigenvector [94].

In *Mulliken Population Analysis* [95, 96, 97, 98], the net contribution $\rho_{\alpha,i}$ of atomic orbital $\phi_\alpha$ to the $i$-th molecular orbital is

$$\rho_{\alpha i} = \sum_j c_{\alpha i} c_{ji} \langle \phi_\alpha | \phi_j \rangle; \tag{2.29}$$

by summing over all atomic orbitals describing an atom $A$, the electronic (Mulliken) atomic population of the atom $A$ is

$$MAP = \sum_i n_i \sum_{\alpha \in A} \rho_{\alpha i} \tag{2.30}$$

where $n_i = 0, 1, 2$ are molecular orbitals occupation numbers. In this way, it is possible to estimate the electronic charge of an atom $A$ for a given system. As it is possible to see from Equation 2.29, this kind of population analysis is basis set dependent, as well as all the other ones relying on atomic orbital expansions; for this reason, reliable comparisons between different systems can be done only if the corresponding calculations are performed with the same basis set.

If we are more interested in analysing molecular orbitals composition, excluding the overlap population coming from integrals of the kind $\langle \phi_i | \phi_j \rangle$, an alternative way is the *C-Squared Population Analysis* [103]. In this method, the contribution $\rho_{\alpha,i}$ of atomic orbital $\phi_\alpha$ to the $i$-th molecular orbital is

$$\rho_{\alpha i} = \frac{c_{\alpha i}^2}{\sum_j {c_{ji}}^2}, \tag{2.31}$$

while the contribution to the same MO of a given cluster of atoms A is given by

$$\rho_{Ai} = \frac{\sum_{\alpha \in A} c_{\alpha i}^2}{\sum_j {c_{ji}}^2}. \tag{2.32}$$

Equations 2.31 and 2.32 allow us to isolate and compare the electronic contributions to single molecular orbitals or to molecular orbital arrangements corresponding to a given energy bin ($\Delta\varepsilon_i$), fixing the discrete energy units in the electronic population analysis. A continuous function $\rho(\varepsilon)$ is achieved by a convolution of fixed width Lorentzian functions weighted by $\rho_{Ai}$ and centred on the energy eigenvalue $\varepsilon_i$.

If atomic details of the electronic distribution give us informations on how molecular orbitals are formed and where the charge is localized, the stability of the system after electron density variations can be studied also by considering the energetic cost of creating a charged defect, that is its *formation energy*. In our calculations, charge variations are accomplished by adding or subtracting electrons from the system; the formation energy $\Delta E^f$ of such charged defect can be calculated according to the following formalism [105]:

$$\Delta E^f(\mu) = \Delta E^d - q(\varepsilon_{TVB} - \mu) \tag{2.33}$$

where $\Delta E^d$ is the energy difference between the defective and the uncharged system, $q$ is the net charge of the system, $\varepsilon_{TVB}$ is the energy of the top of the valence band of the clean host (without any impurities, i.e. dopant or charges) and $\mu$ is the chemical potential for electrons. The curves of $\Delta E^f$ vs $\mu$ are straight lines with slope equal to $-q$; once the model system is fixed and only the net charge is varied, different $\Delta E^f$ lines with different slopes are obtained. The interesting part of such graphs is an energy range including the top valence band and the bottom of the conduction band of the native system. This is because ab initio calculations here presented carry out stable geometries corresponding to zero Kelvin structures, so electrons can be removed from the last occupied energy levels or added to the lowest unoccupied ones. By varying the electron chemical potential $\mu$ within this range, the most stable system, thus the most stable defect, is the one with the lowest total energy.

If ab initio geometrical optimizations are able to describe systems at zero Kelvin, classical molecular dynamics simulations allow us to follow time evolution of a structure at different temperatures. In this case, geometrical features can be described by the *Radial Distribution Function* $g(r)$. This function describes how particle density varies by varying the distance from a given fixed point. In other words, if for $N$ particles in a volume $V$, the mean density is $\rho_0 = N/V$, then the mean density at a distance $r$ from a given space origin is

$$\rho\left(r\right) = g\left(r\right)\rho_0 \tag{2.34}$$

that is, $g(r)$ is a measure of how much different is $\rho(r)$ from $\rho_0$ because of interactions among different particles. Equivalently, $g(r)$ is the relative probability of finding a particle at a distance $r$ from the origin. If the origin is fixed on another particle, this probability can be related to the interaction between the two particles by using the Boltzmann distribution law. That is, the probability of finding two particles at a distance $r$ at equilibrium can be expressed by:

$$g\left(r\right) = e^{-\phi(r)/k_B T} \tag{2.35}$$

where $k_B$ is the Boltzmann constant and $\phi(r)$ is the so called *potential of mean force* [106]. Only two non interacting particles in vacuum have $\phi(r) = 0$ and $g(r) = 1$ for all $r$. At variance, even two non interacting particles in a system of $N$ particles have a non zero $\phi(r)$ due to entropic contributions. In fact, as a rule $\phi(r)$ has a free energy character and it can be dependent on temperature. Let us suppose that in a solid system given $r = r_0$, $g(r_0)$ is a local maximum in a neighbourhood of $r_0$; if in such interval the radial distribution function can be approximated by a Gaussian function, that is

$$\exists\, \varepsilon > 0 : g\left(r\right) \approx e^{-\frac{(r-r_0)^2}{2\sigma^2}} \;\; \forall\, r \in \left(r_0 - \varepsilon, r_0 + \varepsilon\right), \tag{2.36}$$

the mean force potential $\phi(r)$ can be approximated by a harmonic potential with harmonic constant $k$ which is approximately independent on temperature in solids; in this way, the radial distribution function becomes

$$g\left(r\right) = e^{-\frac{k(r-r_0)^2}{2k_BT}}. \tag{2.37}$$

By equating Equation 2.35 with Equation 2.36, we can derive the following linear relation between $\sigma^2$ and the temperature $T$:

$$\sigma^2\left(T\right) = \frac{k_B}{k}T \tag{2.38}$$

that is valid if Equation 2.34 holds and allows one to estimate the mean force constant $k$.

Since the radial distribution function describes how atoms are arranged in space, it is ordinary used to evaluate how many atoms of $A$ kind are there in a spherical shell of thickness $dr$ at a distance $r$ from a $C$ one. In this way, $g(r)$ can be calculated straightforwardly from the molecular dynamical trajectory as

$$g_{A-C}\left(r\right) = \frac{\left\langle \sum_{ij} \delta\left(r_{ij} - r\right)\right\rangle}{\rho_0 V} \tag{2.39}$$

where $\delta(r_{ij}-r)$ is the Dirac's delta, $r_{ij}$ is the distance between the $i$-th atom of $A$ kind and the $j$-th atom of $C$ kind and the average $\langle\cdots\rangle$ is done over the number of timesteps of the whole trajectory.

If $g_{A-C}\left(r\right)$ is evaluated between atomic centres of the same kind (i.e. $A = C$) and approximation 2.36 holds, then $\sigma^2$ is an estimation of the mean square displacement from the equilibrium position of a given atom; from it, the $B$ *atomic temperature factor* [107], called also *Debye-Waller factor*, can be estimated, this being

$$B = 8\pi^2\langle(r - r_0)^2\rangle, \tag{2.40}$$

supposed to be the same for those atoms of the same kind in a given structure.

Another important physical quantity that can be calculated from molecular dynamics trajectories is the *self-diffusion constant* for an atom which is essentially free to move throughout the system; in our simulations, this will be the hydrogen atom. Using the results on Brownian motion, the self diffusion constant, or diffusion coefficient, is related to the mean square displacement of the atom through the following linear relation as a function of the time $t$:

$$\left\langle\left|r\left(t\right) - r\right|^2\right\rangle = 6Dt \tag{2.41}$$

where the $\langle\cdots\rangle$ denotes an ensemble average and $r$ is the position at time origin. Ensemble average can be substituted by a time average if the ergodic hypothesis holds.

For particle moving in a liquid D can be related to particle mobility $\mu$ through the Einstein relation $D = \mu k_B T$. Thus, the problem of knowing D becomes the development of a model for mobility. Another way to build a model for diffusion coefficient is to recognize that macroscopic proton diffusion in a protonic conducting material is a thermally activated process. Once a proton concentration gradient has been established inside the material, protons can move in the opposite way of the concentration gradient to establish uniform concentration. This motion is hindered by forces acting on the hydrogen. Such forces are exerted by surrounding atoms and depend on the system geometry and on the involved atomic species. In other words activation of diffusion motion requires an amount of energy which can be considered independent of temperature. In protonic conduction process, this amount of energy is the one needed by the proton in order to jump from one oxygen atom to another. This amount of energy is called *activation energy* for the overall diffusion process.

For an activated process, at fixed temperature and if the whole system is at the equilibrium, the diffusion coefficient has the form

$$D\left(T\right) = D_0 \exp\left(-E_a/k_B T\right) \tag{2.42}$$

where $E_a$ is the activation energy for the diffusion process. By taking the logarithm of both side of Equation 2.42, the relation can be rewritten as

$$\ln D\left(T\right) = \ln D_0 - \frac{E_a}{k_B}\frac{1}{T} \tag{2.43}$$

underlining the linear relation between the logarithm of the diffusion coefficient $D(T)$ and the inverse of the absolute temperature $T$. Calculating the mean square displacement from the trajectory obtained by the simulation and using Equation 2.41, it is possible to evaluate the activation energy $E_a$ for the diffusion process and the pre-exponential factor $D_0$, that is a measure of the diffusion if no activation energy is needed or in the limit $T \to +\infty$.

A different way of calculating the activation energy $E_a$ of a process is given by the *Arrhenius equation*, that bounds the dependence of the rate constant $k$ of a chemical reaction to the absolute temperature $T$:

$$k\left(T\right) = k_0 \exp\left(-E_a/k_B T\right) \tag{2.44}$$

in a form analogous to that one of Equation 2.42. For our purposes the reaction is the proton hopping and $E_a$ is the energy barrier that the proton must overcome in order to jump from one oxygen atom to another one. The pre-exponential factor $k_0$ contains the information on how many attempts to overcome the barrier can be successful according to its geometrical environment. In other words, $k_0$ is a measure of the activation entropy for the proton hopping.

Taking always as reference the proton hopping process, reaction rate $k$ is related to the proton resident time $\tau$ on a stable site through the following relation:

$$k = \frac{1}{\tau}; \tag{2.45}$$

so, for our analysis, Equation 2.44 can be rewritten as

$$\tau\left(T\right) = \tau_0 \exp\left(E_a / k_B T\right). \tag{2.46}$$

Proceeding as for Equation 2.43:

$$\ln \tau\left(T\right) = \ln \tau_0 + \frac{E_a}{K_B} \frac{1}{T} \tag{2.47}$$

obtaining a linear relation between the logarithm of the residence time $\tau(T)$ and the inverse of the absolute temperature $T$. Analysing dynamics trajectories, it is possible to calculate the residence time $\tau$ for each of the simulation temperature $T$ and, from Equation 2.47, evaluate the activation energy $E_a$ and the pre-exponential factor $\tau_0$.

# Chapter 3

# The $BaCeO_3$ and $BaZrO_3$ Perovskite Systems

Great interest is addressed towards $BaCeO_3$ and $BaZrO_3$ perovskites materials because of their potential as electrolyte materials in several electrochemical devices [23, 24]. $BaCeO_3$ and $BaZrO_3$ derivatives are regarded as ones of the most promising materials, because of their chemical features together with high proton conductivity [20]. Research efforts were thus addressed to understand the elementary processes involved in protonic phenomena related to these materials, mostly to improve their stability and efficiency in working temperatures ranging between 600 and 1100 K.

$BaCeO_3$ undergoes a sequence of phase transitions [78]: it transforms from $Pmcn$ to $Incn$ space group at 563 K, then, after further tilting of the oxygen octahedra, this last phase becomes $F3\bar{2}/n$ at 673 K up to 1173 K, at which the structure becomes cubic with space group $Pm\bar{3}m$. The width of the phase can change according to the dopant content. $BaZrO_3$ crystalline structure, instead, has a cubic $Pm\bar{3}m$ symmetry, not showing any phase transitions after temperature changing [108, 109].

Calculated proton conductivities from data on proton concentrations and mobilities (see Figure 3.1) allow to compare the title materials with similar solid oxide protonic conductors, and show that $BaCeO_3$ derivatives are among the best proton-conducting oxides.

The first elements that allow to understand the origin of such characteristics must be searched in the mechanism responsible of protonic carriers formation in perovskite materials.

As we saw about chemical reaction 1.2 for the incorporation of protonic defects, a water molecule is split into a hydroxide ion and a proton. The enthalpy of this reaction has been studied in different works [34, 110, 111]; it seems that hydration enthalpy tends to become more exothermic with decreasing electronegativity of the cations interacting with the lattice oxygens. In particular, an increase of the B-site cation electronegativity corresponds

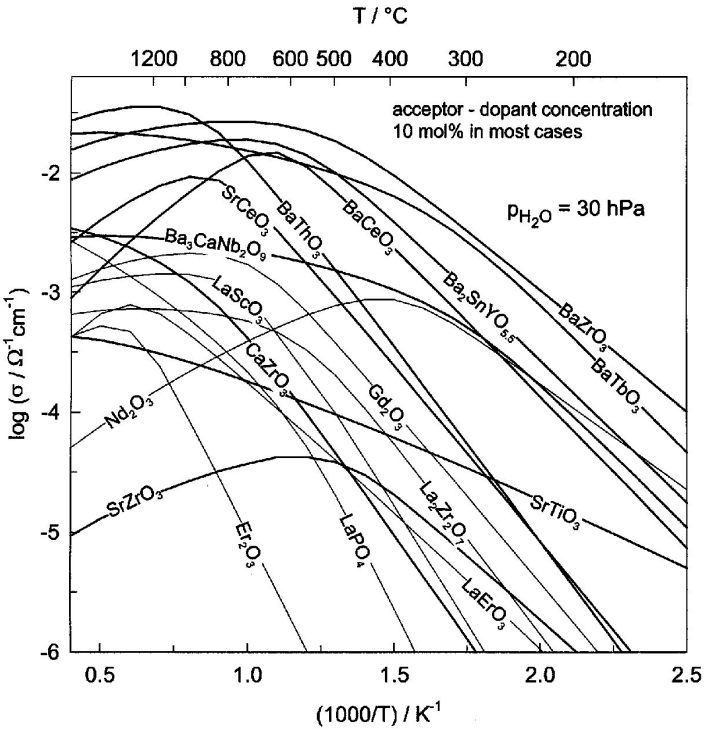


Figure 3.1: Protonic conductivities of various kinds of proton conducting oxides as reported in [20] (redrawn).

to a decrease of the equilibrium constant of the hydration reaction 1.2, in the order cerate, zirconate, stannate, niobate, titanate [15].

At a first sight, the thermodynamics of the formation of protonic defects is affected by the dopant concentration only when the dopant changes the electron density of the surrounding oxygens, as it was supposed for Y:$BaZrO_3$ [31]; on the other hand, computational works on the same or similar compounds [35, 81] infer the role of the geometrical structure of the doped octahedron environment, as experimental data on Y:$BaZrO_3$ with Y concentrations up to 60% seem to point out [112]. Thermogravimetrical analysis on Y:$BaCeO_3$with different doping percentages show similar trends for different yttrium content: samples exposed to laboratory air hydrate within 24 hours, while measurements of water absorption in dry and wet $H_2$ show hysteresis between 200 and 500 °C and the maximum amount of absorbed water is retained at room temperature [113]. The presence of protonic defects also at low temperature and without dopant is allowed because the tetravalent cation in this compound can have +3 charge valence as suggested in luminescence experiments in which $^2D \rightarrow 4F_{5/2}$ and $^2D \rightarrow 4F_{7/2}$ transitions of the $Ce^{3+}$ have been observed [114].

If electronegativity seems to stabilize protonic defects, the stability with respect the presence of acidic gases such as $CO_2$ and $SO_2$ has the opposite trend, while it is less affected by reduction of the crystallographic symmetry [20]. For example, $BaCeO_3$ and $SrCeO_3$ show the same stability against carbonate formation, while protonic defects are better incorporated in $BaCeO_3$ than in $SrCeO_3$ which have a stronger orthorhombic distortion; analogously, Y:$BaZrO_3$ compared with $BaZrO_3$, show a higher proton stabilization than in the case of Sc:$SrTiO_3$ and Y:$BaCeO_3$, this dopant leaving unaltered the cubic $BaZrO_3$ structure at any concentrations [112], as inferred also by ab initio atomistic simulations on it [115, 116, 117].

Proton is usually described outside the $BO_6$ octahedron, forming a highly bent hydrogen bond [15, 78, 79, 118, 119]. This probably because the positively charged B-site cation avoids the formation of linear hydrogen bond and favour the distortion of the protonated octahedron, increasing the activation energy for proton hopping; this consideration is supported by comparing structural and dynamic features in Y:$BaCeO_3$ and Y:$SrCeO_3$ [120], in which proton specializes the equivalent oxygen positions in the cubic structure, changing the electron density distribution and the configuration energy with respect to the unprotonated structure. Although it is commonly accepted that the chemical match of the dopant does not affect the diffusion of the proton [20], simulations on Y,In:$BaCeO_3$ [84] highlight the relevance of the dopant electronic contribution to the electronic structure of the whole system.

Proton preferential structural site can be different at different temperatures also for the same compound. NMR data on $BaCe_{1-x}Y_xO_{3-\delta}$ [121] show a split of the hyperfine line of $^1H$ at increasing temperature, pointing out to formation of two different sites for the proton while, this was not observed for the protonated $SrCe_{0.95}Y_{0.05}O_{3-\delta}$; this was put in correspondence with the transition phase of the Y:$BaCeO_3$. Nonetheless, different oxygen sites seem to be present for some protonated doped compounds that own only one structural oxygen site in the corresponding unprotonated structure. Infrared experiments has been done on Ga, In and Y doped zirconates of Ca, Sr and Ba, revealing more than one structural site for the proton for different dopant atoms [122]; among these, a relevant case is that one of Y:$BaZrO_3$ derivatives: the proton preferred structural oxygens are two despite the structure is cubic. In this last case, proton can be used as a probe for the local arrangement of the doped octahedra, supporting the model of Y clustering for Y doped $BaCeO_3$ and $BaZrO_3$ perovskites (see chapters 4, 5 and 6) [116].

Concerning the transport mechanism, it is almost fairly recognized that rotational diffusion and hopping between two nearest neighbour oxygen atoms are the two main features of the proton transport throughout the material. Computational simulations [123, 35, 119] has already shown that the rate-limiting step is the hopping event, since rotational diffusion has

been shown owing low activation barrier; this is confirmed also by QENS or IR experiments on hydrated compounds [33, 122]. Proton transfer between oxygens implies breaking and forming of more than two hydrogen bonds, since the proton can "see" up to eight oxygen atoms. Depending on the kind of perovskite, the hydrogen transfer can occur between oxygens belonging to the same octahedron or to two different octahedra surrounding the same A cation: the mechanism is called *intra-octahedral* or *inter-octahedral* in the first and in the second case, respectively. In a sketched view, one or the other mechanism occurs according to the size of the cell, with the intra-octahedral one most likely for larger lattice constants [8, 124].

In ideal conditions, protonic concentration is equal to the dopant one: increasing the dopant concentration should lead to a higher incorporation of protonic defects, thus improving the conductivity of the material. This indeed leads, in general, to a reduction of the proton mobility, because doping induces local or crystalline distortions, lowering structural symmetries that are thought to be fundamental for the phonon assisted hydrogen transfer. As an example, indium can enter into $BaZrO_3$ structure in concentrations up to 75%, nonetheless affecting in a dramatic way protonic conductivity of this material [125]. On the other hand, Y:$BaZrO_3$, for Y concentration up to 20%, show high proton mobility, high proton solubility and high stability against the presence of $CO_2$ in the reaction environment, unlike its Y:$BaCeO_3$ counterpart [20].

Samples prepared with different synthesis methods show different conductivity behaviours. For example, gel-to-crystallite technique favours the presence of oxygen defects in doped $BaTiO_3$ samples and conductivity depends also on the environment in which the samples has been prepared before measurements, i.e. from its hydro-thermal history [126]. On the other hand, in Y:$BaZrO_3$ samples, synthesis methods affect mainly the grain conductivity, likely through the dopant distribution on the grain surface or the grain size, while bulk contributions change in a more complex way [127, 128].

## 3.1 Computational Models of $BaCeO_3$ and $BaZrO_3$ Derivatives

One of the most adopted approaches for the computational study of systems derived from $BaCeO_3$ is that one of Islam and co-workers [36, 79, 81, 129]. Simulations on crystalline structures are based on the Born model in which potential energy is partitioned into coulombic long range terms and couple of Buckingham potentials

$$V_{ij} = A_{ij} \exp\left(\frac{-r}{\rho_{ij}}\right) - \frac{C_{ij}}{r^6} \tag{3.1}$$

for the short range part, where $A_{ij}$, $\rho_{ij}$ and $C_{ij}$ are parameters assigned

according to the characteristics of the interaction between $i$ and $j$ ions. If the lattice contains charged defects, it is necessary that the potential can reproduce the polarizability. The *shell* model gives a simple description of this effect [130]: electronic cloud is divided into a core component, made by the nucleus and the internal electrons, and a valence one (*shell*), bounded to the first through a harmonic force.

The most used methodology to model a defect is that one proposed by Mott and Littleton [131]. The part of the lattice surrounding the defect is divided into two regions, including more than 200 atoms, while the external region extend up to infinity. The energy of the system is, in this case, calculated using the *mean field* approach. In this, interaction energies are scaled with the occupancy $x$ of the site: it is defined a *hybrid atom* $(1-x)\,Ce^{4+}$ and $xM^{3+}$ in which M is the substituent of the tetravalent cation coordinating the oxygen octahedron. Thus, the interaction between the hybrid atom and the oxygen ones can be expressed as

$$V_{hybrid} = (1-x)\,V_{Ce^{4+}\ldots O^{2-}} + xV_{M^{3+}\ldots O^{2-}} \tag{3.2}$$

while O−H interaction is modelled using an attractive Morse potential

$$V(r) = D\{1-\exp^{-\beta(r-r_0)}\}^2 \tag{3.3}$$

where $D$, $\beta$ and $r_0$ have been developed for this purpose [132].

Besides the empirical approach discussed above, *ab initio* methods have also been used for both $BaCeO_3$ and $BaZrO_3$ perovskite systems [31, 36, 123, 133, 134, 135, 136]. These are based on LCAOs in the Kohn-Sham scheme within LDA or GGA approximations. The model geometry for such calculations are supercells up to 3x3x3 unit cells of the starting diffraction resolved structures, to which Periodic Boundary Conditions have been applied.

### 3.1.1 $BaCeO_3$ Ab Initio Models

The starting geometries of the model systems for $BaCeO_3$ derivatives investigated in this work, have been chosen after preliminary calculations [137]. These geometries are clusters of atoms extracted from the orthorhombic crystalline structures refined by neutron diffraction data and belonging to the *Pmcn* space group [78]. In order to avoid cutoff truncation outcomes affecting the calculated properties of the B-site local environment, large crystal fragments of suitable geometry were chosen in order to build two different model clusters. The first geometry, with stoichiometry X:$Ba_8Ce_{26}O_{62}$, takes into account the substitution of only one tetravalent cation, while the second, with general composition XZ:$Ba_{12}Ce_{22}O_{61}H_2$, involves the substitution of two cerium atoms, both belonging to vicinal octahedra — see figures 3.2 and 3.3. Since now on, they will be called *single substitution* and *double substitution* model respectively.

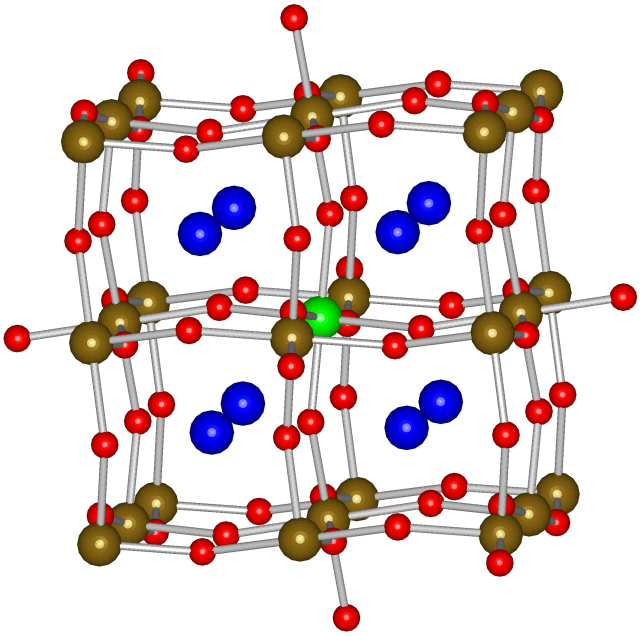

Figure 3.2: X:$Ba_8Ce_{26}O_{62}$ fragment for the single substitution model: Ba, Ce and O centres are in blue, brown and red respectively; the X site (X=Ce,Y,In,Gd) inside the central octahedral moiety is in green.

The composition of the fragment X:$Ba_8Ce_{26}O_{62}$ with X=Ce corresponds to a null-charged singlet state $Ba_8Ce_{26}O_{62}$ system, attributing to the involved atoms the formal charges that they have in the crystalline structure. The doped fragments are considered as hydrated, i.e. without any oxygen vacancies, and they were calculated with a multiplicity equal to $1|e|$ and a resulting charge equal to $-1|e|$. The latter is saturated in the simulations that include the protonic species.

Along the calculations, the positions of the barium atoms and of the centres included in the $XO_6$ octahedral moiety of the starting fragments have been optimized, keeping fixed to the crystalline structure coordinates the remaining species belonging to the external frame.

Figure 3.4 shows the detail of the $Ba_8XO_6$ moiety, that was relaxed along the optimizations. PBC were not applied to the simulation on $BaCeO_3$ and its derivatives, avoiding the typical ordered structural replicas characterizing the periodic applications. The average crystal structure observed by diffraction is produced by insertion of dopants in the B-sites of barium cerate and depends on the dopant concentration. Therefore, it is assumed that in the present model, the $Ba_8XO_6$ central cluster relaxes in the environment of the average structure experimentally observed, with the rigid external

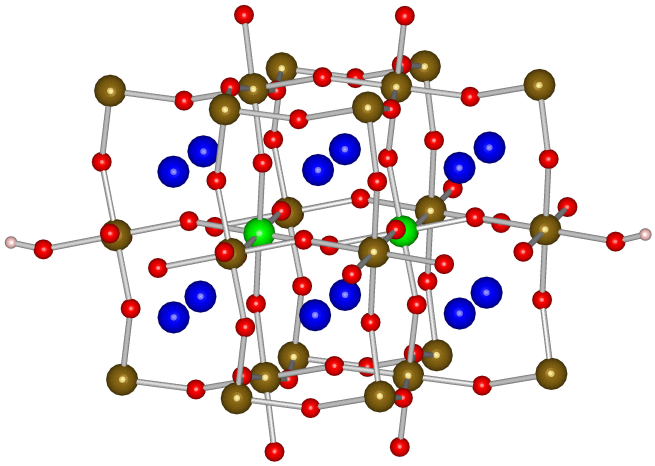

Figure 3.3: XZ:$Ba_{12}Ce_{22}O_{61}H_2$ fragment for the double substitution model: Ba, Ce, O and H centres are in blue, brown, red and white respectively; the X and Z sites (X,Z=Ce,Y) inside each of the central octahedral moiety are in green.

frame bringing in an average way the interaction with the matrix.

The fragment XZ:$Ba_{12}Ce_{22}O_{61}H_2$ has been built to explore the effect of a double yttrium substitution into two adjacent octahedra. As for the cluster described above, the stoichiometry has been chosen in such a way that the system has a null charge if the formal charges of the atoms are those of the crystalline structures by setting X=Z=Ce; moreover, the geometry shape allows to study the relaxation of the environment of two adjacent octahedra, i.e. the moiety $XZBa_4O_{11}$ — see figure 3.5, embedded in a rigid cage reproducing the mean properties of the crystal as for the single octahedron model.

In both substitutional models, the octahedral protonated environment has been studied by adding one hydrogen atom to the atomic moieties to be relaxed, so building a protonated model for the corresponding hydrated compounds — see figures 3.6 and 3.7.

The Gaussian03 suite of programs [138] was employed to perform the calculations in the frame of the HF paradigm [139], by setting X=Ce,Y,In or Gd as octahedral cation in the single octahedron model, and by choosing X,Z=Ce,Y in the double substitution model. In detail, HF energy functional has been employed for the geometry optimizations, after the Gaussian03 standard convergence criteria. Moreover, the SCF component of each calculation was performed by a linear minimum search method, followed, if needed by quadratic minimum search methods [140]. Unless expressly stated, the multiplicity of the systems was fixed to 1, so considering closed

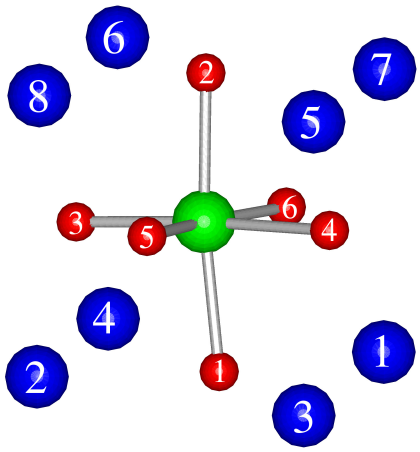


Figure 3.4: $Ba_8XO_6$ moiety of the single substitution model. The colour legend is the same as in Figure 3.2.

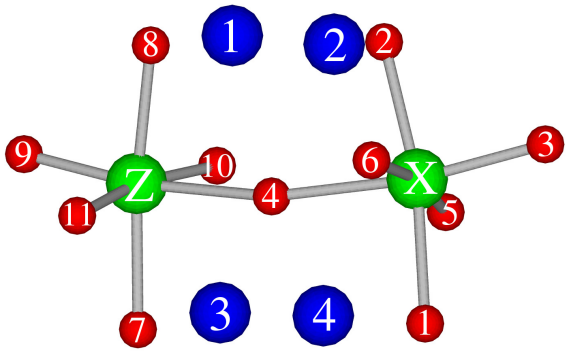


Figure 3.5: $XZBa_4O_{11}$ moiety of the double substitution model. The colour legend is the same as in Figure 3.3.

shell systems.

In the calculations of the geometric and energetic properties of the single and double substitution model fragments, the O atoms belonging to the central octahedra and the external cage were described by the 6-31+G(d,p) [141, 142] and 3-21G [143, 144, 145, 146, 147] basis set respectively. The 6-31+G(d,p) basis set was used to describe also the hydrogen atom in the protonated models. The CRENBL ECP pseudopotential was used for describing the Ba atom, while the SBKJC VDZ ECP was used for the internal octahedral cation (i.e. the $XO_6$ moiety of the atoms to be optimized), unless otherwise specified in the corresponding results chapter 4. These basis sets have been chosen after preliminary calculations performed to balance the

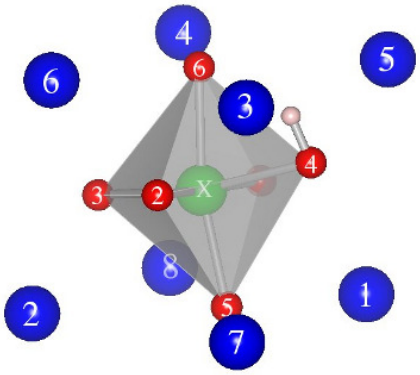


Figure 3.6: $Ba_8XO_6H$ moiety of the single substitution protonated model. The white sphere represents the hydrogen atom; the colour of the other atomic centres follow the colour convention as in Figure 3.2.

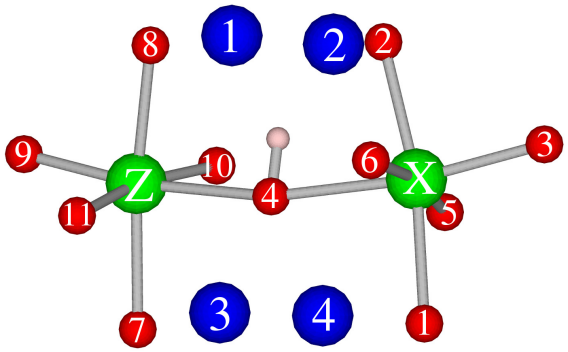


Figure 3.7: $Ba_4XZO_{11}H$ moiety of the double substitution protonated model. The colour legend is the same as in Figure 3.3.

reliability of the results with the computational resources at our disposal [84].

### 3.1.2 $BaZrO_3$ Ab Initio Models

The model systems used to study $BaZrO_3$ derivatives with ab initio approaches are $3 \times 3 \times 3$ and $4 \times 3 \times 3$ supercells (see figures 3.8 and 3.9) built according to the crystalline structure as refined in neutron diffraction experiments and belonging to $Pm\bar{3}m$ cubic space group.

In order to study the Y-doped octahedral environment, the doped structures have been built by substituting one or two zirconium atoms in the starting geometries with corresponding yttrium ones. In particular, in $3 \times 3 \times 3$ supercells, only one zirconium atom has been replaced with an yttrium one,

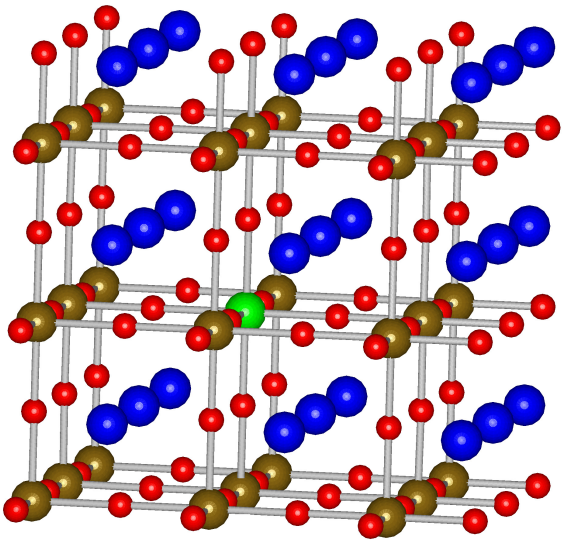

Figure 3.8: Cubic $Pm\bar{3}m$ 3x3x3 supercell of X:$BaZrO_3$: Ba, Zr and O atoms are represented by blue, brown and red spheres respectively; the X site (X=Zr,Y) is in green.

while in $4 \times 3 \times 3$ $BaZrO_3$ supercells, both single and double substitutions have been taken into account. Double substitutions have been realized by replacing two nearest neighbour zirconium atoms each by an yttrium one. Structural rearrangements around one oxygen vacancy have been studied using doped $3 \times 3 \times 3$ and $4 \times 3 \times 3$ supercells, by removing one oxygen atom from the Y first neighbour shell as shown in Figure 3.10.

Local modifications induced after hydration have been explored by using model geometries built by adding one hydrogen atom to the undoped and Y-doped optimized structures. In this case, before the calculation, the hydrogen atom was added in such a way that it can be thought as bound to one of the octahedral oxygen atoms, forming *i*) an O−H distance of 1.1 Å, *ii*) a planar angle of 80.0°with the oxygen to which is bound and the nearest octahedral cation, and, finally, *iii*) a dihedral angle of 17.0°with the oxygen to which is bound, the nearest octahedral cation and the oxygen atom forming a hydrogen bond with it.

Along the calculations, the charge of the systems was fixed to zero except for the structures with one oxygen vacancy, for which different charge values have been considered (from -2 to +2 $|e|$). Moreover, the multiplicity of each system was chosen to be the lowest allowed according to the number of electrons present in the system.

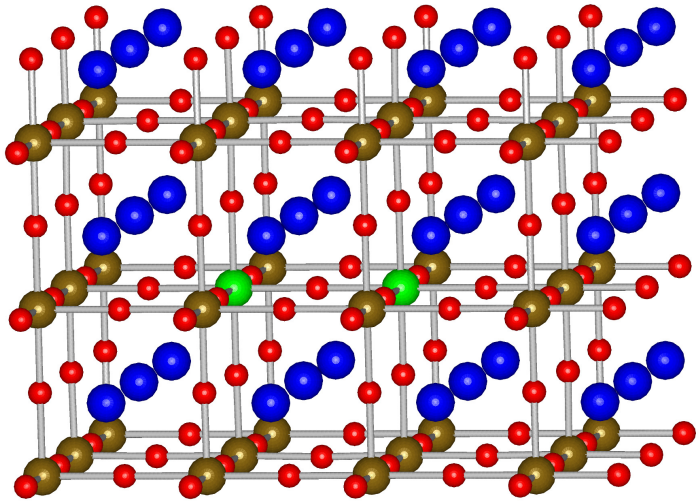

Figure 3.9: Cubic $Pm\bar{3}m$ 4x3x3 supercell of X:$BaZrO_3$: Ba, Zr and O atoms are represented by blue, brown and red spheres respectively; the X and Z sites (X,Z=Zr,Y) are in green.

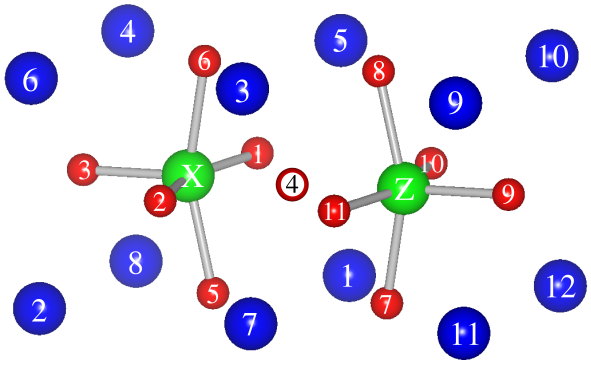


Figure 3.10: Octahedral environment of either $3 \times 3 \times 3$ and $4 \times 3 \times 3$ cubic $Pm\bar{3}m$ XZ:$BaZrO_3$: X=Zr,Y and Z=Zr for $3 \times 3 \times 3$ supercells, while X,Z=Zr,Y for $4 \times 3 \times 3$ supercells. The colour legend is the same as in Figure 3.9; the red circle with label "4" represents either one oxygen atom or one oxygen vacancy, depending on the model to which it is referred.

SIESTA package [148] has been used to perform geometrical optimizations, within DFT-LDA approximation, with the CA energy functional [149]. The Ba and O atoms were described with the basis set optimized for the $BaTiO_3$ perovskite structure [150], while Zr and Y atom basis sets were optimized in $BaZrO_3$ and $Y_2O_3$ systems. All the atomic positions are optimized,

while the lattice vectors are kept fixed. Periodic boundary conditions are used throughout all these calculations.

### 3.1.3 $BaZrO_3$ Molecular Dynamics Models

Besides the ab initio simulations, pure and Y-doped barium zirconate has been also studied by Molecular Dynamics approach, using the Reax Force Field as recently developed for Y:$BaZrO_3$ systems [151].

The model starting structures are $4 \times 3 \times 3$ supercells of cubic $Pm\bar{3}m$ $BaZrO_3$ as resolved by neutron diffraction data [108] and they are geometrically identical to the $4 \times 3 \times 3$ clusters used for the ab initio simulations on the same compound – see Figure 3.9.

In order to simulate the Y-doped compound, one or two zirconium atoms has been substituted by corresponding yttrium ones, while proton diffusion has been studied through protonated structures obtained by adding one proton to the doped and undoped ones.

MD simulations have been carried out at various temperatures: 100, 250, 500, 750, 1000 and 1250 K with a simulation time of 2 ns, applying Periodic Boundary Conditions to the model clusters.

# Chapter 4

# $BaCeO_3$ Derivatives Ab Initio Results

As described in subsection 3.1.1, single and double substitution models have been considered, starting from the crystalline orthorhombic *Pmcn* structure. The results obtained with each model will be presented as grouped for protonated and unprotonated systems, comparing the different structures and discussing the features characterizing them.

## 4.1 Single Substitution Model

The here proposed approach should give locally un-constrained results [152] on the studied octahedral environment, although it introduces structural and electronic constrains on the surrounding fixed framework. Notwithstanding this, as we will show, the considered fragment is however large enough and these border restrictions are not affecting the local properties of the central $Ba_8XO_6$ moiety.

### 4.1.1 Unprotonated Fragments

Unprotonated fragments will be considered invariantly with all the oxygen sites occupied, i.e. without any oxygen vacancies, since the hydrated average structure is taken into account.

**Undoped Fragment.** In order to investigate the structural rearrangements after substitution of the tetravalent octahedral cation (i.e. Ce) with a trivalent one, for the $Ba_8XO_6$ moiety the dopant atom X was chosen to be Y, In and Gd. In Table 4.1, the main geometrical features of the experimental and optimized $Ba_8CeO_6$ moiety are reported.

The sets of oxygen atoms {O5, O1, O6, O2}, {O4, O6, O3, O5} and {O3, O1, O4, O2} single out three different planes containing the central Ce

Table 4.1: Relevant geometrical parameters characterizing the central octahedron environment of the undoped orthorhombic, *Pmcn* $BaCeO_3$, fragment.

| distances[a]/ Å | NPD[b] | EXAFS[c] | Ce0[d] | Ce1[d] |
|---|---|---|---|---|
| Ce−O1 | 2.25 | — | 2.27 | 2.24 |
| Ce−O2 | 2.25 | — | 2.27 | 2.24 |
| Ce−O3 | 2.24 | — | 2.28 | 2.24 |
| Ce−O4 | 2.24 | — | 2.28 | 2.24 |
| Ce−O5 | 2.25 | — | 2.28 | 2.24 |
| Ce−O6 | 2.25 | — | 2.28 | 2.24 |
| <Ce−O>[e] | 2.25 | 2.27 | 2.28 | 2.24 |
| Ce−Ba1 | 3.91 | — | 3.80 | 3.83 |
| Ce−Ba2 | 3.77 | — | 4.00 | 3.87 |
| Ce−Ba3 | 3.69 | — | 3.74 | 3.68 |
| Ce−Ba4 | 3.84 | — | 3.83 | 3.78 |
| Ce−Ba5 | 3.84 | — | 3.83 | 3.78 |
| Ce−Ba6 | 3.69 | — | 3.74 | 3.68 |
| Ce−Ba7 | 3.77 | — | 4.00 | 3.87 |
| Ce−Ba8 | 3.91 | — | 3.80 | 3.83 |
| <Ce−Ba>[e] | 3.80 | 3.81 | 3.84 | 3.79 |
| angles / ° | NPD | EXAFS | Ce0 | Ce1 |
| O1−Ce−O5 | 89.0 | — | 91.3 | 90.1 |
| O2−Ce−O3 | 91.6 | — | 89.7 | 90.8 |
| O3−Ce−O5 | 90.4 | — | 90.5 | 91.4 |

[a] For the atomic labelling see Figure 3.4. [b] Neutron powder diffraction parameter values as determined at liquid helium temperature in [118]. These geometrical parameters were also used as starting input in the optimizations whose results are summarized in the Ce0 and Ce1 columns. [c] Results at liquid nitrogen temperature reported by [85] [d] The Ce0 and Ce1 labels refer to the SBKJC VDZ ECP and CRENBL ECP basis sets used for the Ba atoms, respectively. [e] Mean values of the corresponding atomic distances.

cation, both before and after the calculations. In each of these planes, two couples of oxygen atoms, together with the Ce one, individuate two incident lines, making two opposite-to-the-vertex pair of angles. Since no constraint are imposed to the optimized coordinates, the results demonstrate that the atomic arrangement of the central cluster fits into the average long-range structure determined by neutron diffraction experiments, without large local distortion. Comparisons with other calculations show good agreement with

the Ce−O found distances [79].

**Y-doped Fragment.** Structural modifications after inserting Y into the structure, have been investigated by also describing the dopant atom with the Stuttgart RSC 1997 ECP pseudopotential and basis set [153, 154, 155], giving a description more accurate than the SBKJC VDZ ECP ones. With this choice, four model systems has been considered, named CS1, CS2, CS3 and CS4, as shown in Table 4.2.

By using CS1, we intended to investigate the effect of a higher level basis set on the inner atom of the central octahedron, with the charge and multiplicity state unchanged with respect to those employed for the CR system. On the other hand, with CS2 model we investigate the effect of changing the multiplicity state, imposing the triplet state to the Y:$Ba_8Ce_{26}O_{62}$ fragment. By CS3 approach, we analysed the effect of a larger atom cluster optimization, by relaxing also the positions of the Ce atoms directly linked to the O atoms of the central octahedron. Finally, we also considered a bisubstituted fragment, 2 Y:$Ba_8Ce_{25}O_{62}$, which was treated by CS1 approach. The geometrical features found for angles and distances opposite to the Ce vertex in the $CeO_6$ octahedron still hold for all the yttrium-doped structures here considered.

The use of a higher level basis set for the Y atom in the CS1 approach did not carried significant variation on the optimized geometrical parameters, while on the whole, results are in a satisfying agreement with experimental values. The models disregards some inferences originating by EXAFS analysis [86]. These suggested that structural vacancies, not considered in the model may occur. Despite this, it is interesting to notice that both the experimental and the computational results agree in pointing out a slight contraction of the barium shell toward the yttrium species.

The two sets of Y−O distances observed by EXAFS [86] and attributed to an axial elongation of the $YO_6$ octahedron, were not reproduced by the computational approaches. The length inhomogeneity could be experimentally produced by the structural vacancy defects above or by other local distortion not taken into consideration by the models so far described. The Y−O distance inhomogeneity is present at temperatures as high as 773 K, also under very different hydration conditions [86]. Furthermore, the relaxation of a larger atom cluster ($Ba_8YCe_6O_6$ instead of $Ba_8YO_6$) of the CS3 simulation did not increase the reliability of the optimization.

The 2 Y model was investigated in order to find a possible origin of the bimodal distribution pointed out by the EXAFS results, which were not reproduced by any of the CSn single Y considered models. To this purpose, considering the structure optimized by the CS1 approach, at first we performed a preliminary calculation in which the position of the second yttrium (introduced by substitution of the Ce atom linked to O4) and its octahe-

Table 4.2: Relevant geometrical parameters characterizing the central octahedron environment of the Y-doped orthorhombic, *Pmcn* Y:$BaCeO_3$, fragment.

| distances[a]/ Å | EXAFS[b] | SB[c] | CR[c] | CS1[d] | CS2[d] | CS3[d] | 2Y[e] |
|---|---|---|---|---|---|---|---|
| Y−O1 | — | 2.32 | 2.28 | 2.28 | 2.28 | 2.25 | 2.26 |
| Y−O2 | — | 2.32 | 2.28 | 2.28 | 2.28 | 2.25 | 2.28 |
| Y−O3 | — | 2.31 | 2.27 | 2.27 | 2.28 | 2.25 | 2.20 |
| Y−O4 | — | 2.31 | 2.27 | 2.27 | 2.28 | 2.25 | 2.37 |
| Y−O5 | — | 2.33 | 2.28 | 2.28 | 2.27 | 2.26 | 2.28 |
| Y−O6 | — | 2.33 | 2.28 | 2.28 | 2.27 | 2.26 | 2.30 |
| <Y−O>[f] | 2.26 | 2.32 | 2.28 | 2.28 | 2.28 | 2.25 | 2.28 |
| Y−Ba1 | — | 3.72 | 3.77 | 3.77 | 3.81 | 3.64 | 3.56 |
| Y−Ba2 | — | 3.91 | 3.80 | 3.80 | 3.80 | 3.67 | 3.87 |
| Y−Ba3 | — | 3.67 | 3.62 | 3.62 | 3.55 | 3.47 | 3.56 |
| Y−Ba4 | — | 3.75 | 3.73 | 3.72 | 3.76 | 3.62 | 3.78 |
| Y−Ba5 | — | 3.75 | 3.73 | 3.72 | 3.76 | 3.62 | 3.55 |
| Y−Ba6 | — | 3.67 | 3.62 | 3.62 | 3.55 | 3.47 | 3.63 |
| Y−Ba7 | — | 3.91 | 3.80 | 3.80 | 3.80 | 3.67 | 3.81 |
| Y−Ba8 | — | 3.72 | 3.77 | 3.77 | 3.81 | 3.64 | 3.82 |
| <Y−Ba>[f] | 3.76 | 3.76 | 3.73 | 3.73 | 3.73 | 3.60 | 3.70 |
| angles / ° | EXAFS | SB | CR | CS1 | CS2 | CS3 | 2Y |
| O1−Y−O5 | — | 88.9 | 89.9 | 89.9 | 89.3 | 91.6 | 90.5 |
| O2−Y−O3 | — | 89.5 | 89.1 | 90.9 | 90.4 | 89.3 | 92.5 |
| O3−Y−O5 | — | 90.3 | 90.9 | 90.9 | 91.3 | 91.6 | 95.1 |

[a] For the atomic labelling see Figure 3.4. [b] Results at 120 K reported by [86]. [c] The SB and CR labels refer to the SBKJC VDZ ECP and CRENBL ECP basis sets employed for the Ba atoms, respectively.
[d] In the CSn calculations the Y atom was treated by the Stuttgart RSC 1997 ECP basis set: in the CS1 and CS2 calculations closed-shell singlet-state and open-shell triplet-state systems were considered while in the CS3, closed-shell, calculation the Ce atoms linked to the O atoms of the central octahedron were also relaxed. [e] The 2 Y:$Ba_8Ce_{25}O_{62}$ system was treated as the mono substituted CR Y:$Ba_8Ce_{26}O_{62}$ one. The second yttrium atom is linked to the first one through the O4 atom.
[f] Mean values of the corresponding atomic distances.

dral oxygen environment were allowed to optimize then, starting from the locally optimized structure, the central octahedron and the barium atoms were relaxed as usual. By this procedure, the sets of oxygen planes {O5, O1, O6, O2}, {O4, O6, O3, O5} and {O3, O1, O4, O2}, and the characteristic symmetry around yttrium inside the central octahedron were as expected lost.

Analysing the results on the 2 Y system above, it is possible to attempt

a rationalization of the Y−O bimodal distance set, around 2.33 and 2.23 Å, with weight 2/3 and 1/3 respectively, determined by the EXAFS approaches applied to Y:$BaCeO_3$ derivatives [86]. As a matter of fact, three characteristic Y−O distances, with different statistical weights, can be recognized in the 2 Y data in Table 4.2: 2.20, 2.30 and 2.40 Å, being the longest and the shortest distance on the same line including the two Y atoms present in the 2 Y:$Ba_8Ce_{26}O_{62}$ fragment. From this result, we could infer that the experimental Y−O distance distribution could be given by a bimodal spread originated by the clustering of the Y−O−Y local arrangements.

**In-doped Fragment.** In contrast with yttrium, that has a solubility limit of $\sim$ 15%, indium can be inserted into the barium cerate matrix in any amount, producing eventually a change in the symmetry of the In:$BaCeO_3$ mixed oxide. At low indium concentration, the doped oxide is still orthorhombic, with space group *Pmcn*.

Relevant distances and angles of the *Pmcn* In:$BaCeO_3$ fragment and corresponding experimental findings are reported in Table 4.3

The In0 approach shows that both the In−O and In−Ba distances should be characterized by specific distributions. Increasing the level of the In basis set (aug-cc-pV5Z-PP basis set is supplied for In in AUG calculation), only one In−O distance is singled out, satisfactory in agreement with the experimental trend [156].

Like for the other calculated doped and undoped systems, the geometrical features concerning pairs of angles and distances opposite to the In atom still hold, when the aug-cc-pV5Z-PP are employed. Finally, AUG approach is able to capture the larger shrinking of the octahedral oxygens and the surrounding barium atoms on the indium one respect to the yttrium atom, as found by EXAFS experiments on doped $BaCeO_3$ derivatives [156].

**Gd-doped Fragment.** Octahedral trivalent cation environment in gadolinium-doped barium cerate has been studied by choosing X=Gd for the $BaXO_6$ moiety to be optimized. We performed geometrical relaxations with different basis set and pseudopotential used for the gadolinium atom: Stuttgart RSC 1997 ECP and Stuttgart RSC ANO/ECP [159], setting to 0 and 1 the charge and multiplicity values, respectively. A simulation with a null charge and a triplet spin state was also performed with Stuttgart RSC 1997 ECP pseudopotential and basis set, in order to explore possible open-shell effects. Moreover, to take into account correlation effects, without increasing the computational cost, a third geometrical optimization was performed, following ONIOM prescriptions [160]. In the last case, Gd:$Ba_8Ce_{26}O_{62}$ fragment was fractioned into two layers: the $Ba_8GdO_6$ and the $Ce_{26}O_{56}$ fragments. The former (model system), corresponding to the central octahedron environment, was treated at B3LYP level [161, 162, 163],

Table 4.3: Relevant geometrical parameters characterizing the central octahedron environment of the In-doped orthorhombic, *Pmcn* In:$BaCeO_3$, fragment.

| distances[a]/ Å | EXAFS[b] | In0[c] | AUG[d] |
|---|---|---|---|
| In−O1 | — | 2.13 | 2.20 |
| In−O2 | — | 2.13 | 2.20 |
| In−O3 | — | 2.23 | 2.20 |
| In−O4 | — | 2.23 | 2.20 |
| In−O5 | — | 2.26 | 2.22 |
| In−O6 | — | 2.26 | 2.22 |
| <In−O>[e] | 2.16 | 2.21 | 2.21 |
| In−Ba1 | — | 3.68 | 3.70 |
| In−Ba2 | — | 3.75 | 3.75 |
| In−Ba3 | — | 3.52 | 3.53 |
| In−Ba4 | — | 3.67 | 3.67 |
| In−Ba5 | — | 3.67 | 3.67 |
| In−Ba6 | — | 3.52 | 3.53 |
| In−Ba7 | — | 3.75 | 3.75 |
| In−Ba8 | — | 3.68 | 3.70 |
| <In−Ba>[e] | 3.64 | 3.65 | 3.66 |
| angles / ° | EXAFS | In0 | AUG |
| O1−Y−O5 | — | 89.9 | 90.1 |
| O2−Y−O3 | — | 90.6 | 89.7 |
| O3−Y−O5 | — | 90.7 | 89.9 |

[a] For the atomic labelling see Figure 3.4.
[b] Results at liquid nitrogen temperature reported by [156]. [c] The In0 labels refer to the calculation performed by using the CRENBL ECP basis set for the Ba atoms. [d] In the AUG calculation the In atom was treated by the aug-cc-pV5Z-PP basis set as reported in https://bse.pnl.gov/bse/portal [157, 158].
[e] Mean values of the corresponding atomic distances.

while the latter (real system) was treated at HF level. In this last calculation, the Stuttgart RSC 1997 ECP basis set and pseudopotential was used for the Gd atom.

Gd−O distance values, calculated with the Gd0, Gd1 and Gd2 approaches (see table 4.4), show narrow distributions round one mean value, lower than that one observed in EXAFS measurements [164]; the discrepancy is removed in the ONIOM calculation. On the other hand, the spreading

Table 4.4: Relevant geometrical parameters characterizing the central octahedron environment of the Gadolinium-doped orthorhombic, *Pmcn* Gd:$BaCeO_3$, fragment.

| distances[a]/ Å | EXAFS[b] | Gd0[c] | Gd1[c] | Gd2[c] | ONM[d] |
|---|---|---|---|---|---|
| Gd−O1 | — | 2.17 | 2.16 | 2.19 | 2.28 |
| Gd−O2 | — | 2.17 | 2.16 | 2.19 | 2.28 |
| Gd−O3 | — | 2.16 | 2.18 | 2.19 | 2.30 |
| Gd−O4 | — | 2.16 | 2.18 | 2.19 | 2.30 |
| Gd−O5 | — | 2.21 | 2.19 | 2.19 | 2.32 |
| Gd−O6 | — | 2.21 | 2.19 | 2.19 | 2.32 |
| <Gd−O>[e] | 2.32 | 2.18 | 2.18 | 2.19 | 2.30 |
| Gd−Ba1 | — | 3.78 | 3.80 | 3.82 | 3.78 |
| Gd−Ba2 | — | 3.84 | 3.84 | 3.84 | 3.79 |
| Gd−Ba3 | — | 3.61 | 3.62 | 3.78 | 3.56 |
| Gd−Ba4 | — | 3.78 | 3.73 | 3.78 | 3.73 |
| Gd−Ba5 | — | 3.78 | 3.73 | 3.68 | 3.78 |
| Gd−Ba6 | — | 3.61 | 3.62 | 3.68 | 3.56 |
| Gd−Ba7 | — | 3.84 | 3.84 | 3.82 | 3.73 |
| Gd−Ba8 | — | 3.78 | 3.80 | 3.82 | 3.79 |
| <Gd−Ba>[e] | 3.54 | 3.75 | 3.75 | 3.78 | 3.71 |
| angles / ° | EXAFS | Gd0 | Gd1 | Gd2 | ONM |
| O1−Gd−O5 | — | 89.9 | 89.8 | 90.1 | 88.3 |
| O2−Gd−O3 | — | 90.1 | 90.4 | 90.6 | 89.7 |
| O3−Gd−O5 | — | 90.6 | 91.1 | 90.8 | 90.3 |

[a] For the atomic labelling see Figure 3.4. [b] Results at 25K reported in [164]. [c] In Gd0 and Gd1 label calculations the Gd atom was treated by the Stuttgart RSC/ANO and Stuttgart RSC 1997 basis set respectively, in which close-shell systems were considered while in Gd2 calculation an open-shell system was considered describing Gd atom with Stuttgart RSC 1997 pseudopotential and basis set.
[d] In ONM calculation, the optimized $Ba_8GdO_6$ model system was treated at B3LYP level while the remaining $Ce_{26}O_{56}$ real system was treated at HF level; the basis sets and the multiplicity of the system were the same as in Gd1 calculation.
[e] Mean values of the corresponding atomic distances.

of the Gd−Ba distance values carried out in all calculations, allow to single out a bimodal distribution, whose mean values of 3.56 and 3.76 Å found with ONIOM simulation are different from the corresponding experimental values; nonetheless, they reasonably reproduce the statistical weight of 2/8 and 6/8 for the shorter and longer Gd−Ba distances found in the cited experimental work, describing also the increase of volume of the $GdO_6$ octa-

hedron and the contraction of the barium coordination shell compared with the undoped case.

In a computational work on $BaCeO_3$ derivatives [84], the ONIOM approach was used to investigate the possible structural modifications induced on the octahedral environment by the correlation effects for the cerium atom, being this one a lanthanide; as shown, significative differences in the Ce−O distances were found when the basis set describing the barium atom was improved within the HF scheme, while the ONIOM calculation gave the same results of the low level one. Since correlation is known to shrink bonds in materials of this kind, these results must be checked to ensure the reliability of the model, despite the agreement with experimental findings*.

### 4.1.2 Protonated Fragments

Structural modifications induced after hydration of $BaCeO_3$ perovskite compounds have been studied by considering structures containing one hydrogen atom. Starting from the optimized geometries of the models discussed in the preceding section, one proton has been added into the structure, as if bound to the oxygen labelled as 4 in Figure 3.6. The proton position before performing the geometrical optimizations is set the same for all the fragments here discussed: O4−H distance, H−O4−X angle and H−O4−O2−O6 dihedral angle were set to 1.10 Å, 80.0°and 17.0°respectively. This configuration is the starting point for the research of one of the proton stable positions near the octahedral site. In order to do this, proton coordinates has been left free to optimized without any restraints.

**Undoped Fragment.** Since protonic defects are mainly present in doped structures (see section 1.5), this model is intended to be a possible description of a portion of the crystal far from the substitutional point defect, i.e. the environment of an octahedral undoped site, far from a doped one.

As starting configuration, the optimized atomic positions of Ce1 geometry has been considered (see Table 4.1) together with the same pseudopotentials and basis set; then, the coordinates of the $Ba_8CeO_6H$ moiety have been relaxed. Relevant distances and angles so obtained are reported in Table 4.5, together with the undoped reference structure.

The Ce−O distances produce a strong deformation of the octahedral site, ranging between 2.13 and 2.38 Å. Comparing these results with those ones found for the unprotonated system, we found that the octahedral volume remains nearly the same, while the Ce−Ba distances increase, leading to an expansion of the proton environment; in particular, the perturbation on the distances Ce−O3, Ce−O4 and Ce−O6 is stronger compared to the other Ce−O ones. Due to the little value of the H−O4−Ce−O6 dihedral

*Thanks to Prof. L. Seijo for having point out this comment.

Table 4.5: Relevant geometrical parameters characterizing the central octahedron environment of the protonated undoped orthorhombic, *Pmcn* $BaCeO_3H$, fragment.

| distances[a]/ Å | Ce1[b] | Ce1H[c] | Ce1H-TS[d] |
|---|---|---|---|
| Ce−O1 | 2.24 | 2.20 | 2.19 |
| Ce−O2 | 2.24 | 2.22 | 2.23 |
| Ce−O3 | 2.24 | 2.13 | 2.10 |
| Ce−O4 | 2.24 | 2.38 | 2.30 |
| Ce−O5 | 2.24 | 2.21 | 2.17 |
| Ce−O6 | 2.24 | 2.29 | 2.40 |
| <Ce−O>[e] | 2.24 | 2.24 | 2.23 |
| Ce−Ba1 | 3.83 | 4.21 | 4.19 |
| Ce−Ba2 | 3.87 | 3.79 | 3.70 |
| Ce−Ba3 | 3.68 | 3.77 | 3.79 |
| Ce−Ba4 | 3.78 | 3.82 | 3.86 |
| Ce−Ba5 | 3.78 | 3.89 | 3.88 |
| Ce−Ba6 | 3.68 | 3.65 | 3.71 |
| Ce−Ba7 | 3.87 | 4.08 | 4.26 |
| Ce−Ba8 | 3.83 | 3.87 | 3.79 |
| <Ce−Ba>[e] | 3.79 | 3.89 | 3.90 |
| O4−H | 1.10 | 0.95 | 1.01 |
| angles[f]/ ° | Ce1 | Ce1H | Ce1H-TS |
| H−O4−Ce | 80.0 | 86.1 | 66.7 |
| H−O4−O2−O6 | 17.0 | 37.7 | 20.9 |

[a] For the atomic labelling see Figure 3.6.
[b] Geometrical parameters of the Ce1 system as presented in Table 4.1, used as starting input in the optimizations whose results are summarized in the Ce1H column. Values are reported for comparison purposes. [c] Optimized values for the hydrogenated system with the proton in the stable position. [d] Calculated parameters for the system with the proton in a transition-like state along the hopping path. [e] Mean values of the corresponding atomic distances. [f] Planar and dihedral angle values of the specified atoms are reported. For the Ce1 system, values are a starting guess for proton position (see the text).

angle (13.6°), we can regard to the proton as nearly lying onto the plane individuated by O4−Ce−O6 atoms and we can call as *planar* the induced distortion, inferring a certain directionality of the proton perturbation. At last, the O4−Ce−O2, O4−Ce−O6 and O2−Ce−O6 angles have smaller val-

ues than the starting ones.

This optimized geometry was used as starting point for a further calculation, intended to investigate the features of the proton environment during the hopping event. The starting position of the hydrogen atom was chosen like if it were about in a median position between two oxygen atoms, in order to search for a likely transition state along the transfer path. In this aim, the initial O2−H, O4−H, O6−H and Ce−H distances were set to 2.25, 1.56, 1.60 and 1.96 Å respectively. During the calculation, the position of the proton was kept fixed, while the $Ba_8CeO_6$ cluster were left free to optimize; in this way, we don't impose any constraints to the protonic transfer path to be investigated. This choice, in our opinion, is a valid alternative to that one of keeping fixed all the coordinates of all the atoms and searching for a transition state by sampling the potential energy surface using the proton as a probe, especially if we take into account the computational cost (time and resources) needed to get enough samples at the calculation level here discussed. The results carried out with this approach are summarized in the columns Ce1H-TS shown in the Table 4.5. Comparing the distances with those found for Ce1H system, it turns out that the octahedral volume remains nearly the same as well as the Ce−Ba mean distance, with the increased Ce−Ba3 distance due to the presence of the proton between them (see Figure 3.6). Compared with the Ce1H system, Ce−O distances undergoes a further planar distortion, while the Ce−O axial ones are not changed; moreover, Ce−O3, Ce−O4 and Ce−O5 distances are shorter whereas Ce−O4 and Ce−O6 seem to have exchanged their role in stabilizing proton position, being now the former shorter than the latter.

O4−Ce−O2, O4−Ce−O6 and O2−Ce−O6 angles have even smaller values than the starting ones, as well as the H−O2−O4−O6 dihedral angle: globally, the oxygen geometrical configuration is further distorted toward the proton position, while the volume of the proton environment, e.g. the $Ba_8CeO_6$ moiety, remains unchanged.

**Y-doped Fragment.** Y-doped protonated octahedral environment has been studied using the computational model CS1 of the corresponding unprotonated system (see Table 4.2). Geometrical optimizations has been performed as usual, carrying out the results briefly summarized in Table 4.6

Similarly to what we found for the undoped protonated systems, the distances between the octahedral cation and the oxygen atoms surrounding it show a strong deformation ranging from 2.15 and 2.34 Å. Compared with the corresponding undoped structure Ce1H, these findings show that the overall octahedral volume remains almost the same while the Y−Ba distances, in average, increase, obtaining again an expansion of the proton environment. The Y−O3 and Y−O4 distances are longer and shorter than the starting

Table 4.6: Relevant geometrical parameters characterizing the central octahedron environment of the protonated Y-doped orthorhombic, *Pmcn* Y:$BaCeO_3H$, fragment.

| distances[a]/ Å | CS1[b] | CS1H[c] | CS1H-TS[d] | CS1H-TS2[e] |
|---|---|---|---|---|
| Y−O1 | 2.28 | 2.26 | 2.23 | 2.23 |
| Y−O2 | 2.28 | 2.28 | 2.30 | 2.32 |
| Y−O3 | 2.27 | 2.15 | 2.12 | 2.18 |
| Y−O4 | 2.27 | 2.34 | 2.27 | 2.29 |
| Y−O5 | 2.28 | 2.24 | 2.20 | 2.12 |
| Y−O6 | 2.28 | 2.29 | 2.38 | 2.32 |
| <Y−O>[f] | 2.28 | 2.26 | 2.25 | 2.24 |
| Y−Ba1 | 3.77 | 4.11 | 4.06 | 3.95 |
| Y−Ba2 | 3.80 | 3.73 | 3.64 | 3.72 |
| Y−Ba3 | 3.62 | 3.65 | 3.68 | 3.50 |
| Y−Ba4 | 3.72 | 3.72 | 3.76 | 3.82 |
| Y−Ba5 | 3.72 | 3.78 | 3.78 | 3.67 |
| Y−Ba6 | 3.62 | 3.59 | 3.64 | 3.73 |
| Y−Ba7 | 3.80 | 4.06 | 4.25 | 4.10 |
| Y−Ba8 | 3.77 | 3.71 | 3.65 | 3.68 |
| <Y−Ba>[f] | 3.73 | 3.79 | 3.81 | 3.77 |
| O4−H | 1.10 | 0.95 | 1.01 | 2.26 |
| angles[g]/ ° | CS1 | CS1H | Ce1H-TS | CS1H-TS2 |
| H−O4−Ce | 80.0 | 76.7 | 64.8 | 55.41 |
| H−O4−O2−O6 | 17.0 | 29.63 | 18.4 | 14.18 |

[a] For the atomic labelling see Figure 3.6. [b] Geometrical parameters of the CS1 system as presented in Table 4.2, used as starting input in the optimizations whose results are summarized in the CS1H column. Values are reported for comparison purposes. [c] Optimized values for the hydrogenated system with the proton in the stable position. [d] Calculated parameters for the system with the proton in the transition-like state along the hopping path. [e] Relevant geometrical parameters for the system with the proton nearly at the end of the transfer path. [f] Mean values of the corresponding atomic distances. [g] Planar and dihedral angle values of the specified atoms are reported. For the CS1 system, values are a starting guess for proton position (see the text).

ones respectively, showing again a strong planar perturbation of the Y−O distances as found for the corresponding undoped protonated system. Moreover, the H−O4−O2−O6 optimized dihedral angle results smaller than that one of the optimized Ce1H system.

Using the same protocol for the Ce1H-TS calculation of the paragraph above, we used this optimized geometry as a starting point for a further cal-

culation in the aim to study the local environment of the protonated doped site in $YBaCeO_3$ perovskite during proton migration. The initial O2−H, O4−H, O6−H and Y−H distances were set to 2.29, 1.56, 1.57 and 1.93 Å respectively. As for Ce1H-TS simulation, we don't impose any constraints to the transfer path to be investigated, trying to optimize the ratio between the computational cost and the amount of informations needed to study a proton transfer path. The results are shown in the Table 4.6.

Inspecting the obtained values, it comes out that all but Y−O2 and Y−O6 distances are shorter than the starting ones, resulting the Y−O6 distance the most elongated; moreover the O4−Y−O2, O4−Y−O6 and O2−Y−O6 angles and the H−O2−O4−O6 dihedral angle have smaller values than the starting ones. All Y−O starting and final distances, except those concerning O1 and O2, have almost the same value of the corresponding undoped systems CS1H and CS1H-TS; furthermore, for each couple of systems with the same octahedral cation, the differences between the corresponding H and H-TS systems are almost the same and with the same sign, except for the H−O2−O4−O6. This last one, results larger for the Ce1H than the CS1H model, acquiring practically the same value in the corresponding H-TS systems. Concerning the Y−Ba distances, a significantly increasing of the Y−Ba3 distance is found, being the Ba3 atom the nearest one to the proton, leaving unaltered the volume of the $Ba_8YO_6$ moiety. Finally, it is worthy to note that X−O distances in Ce1H-TS and CS1H-TS systems have very close values, suggesting that the proton, at that point of the transfer path, rearranges X−O distances in the same way, regardless of the octahedral cation species.

Starting from the last optimized configuration (CS1H-TS), we performed a further geometrical optimization, choosing for the proton, as starting point, a mean position along a probable path toward the closest O6 oxygen atom. As before, only the $Ba_8YO_6$ moiety was left free to optimize, keeping fixed the starting proton position. The results are shown in the column CS1H-TS2 in Table 4.6.

In this last simulation, all the Y−O distance values changed except for the Y−O1 and Y−O2 that maintain nearly the values they had at the beginning of the optimization. In particular, if we compare the resulting Y−O distance values with those of the CS1H system, the distances are rearranged like if O6 and O4 oxygen atoms exchanged their position, as well as the O3 and O5 atoms, while the Y−O2 and Y−O1 distances slightly change, increasing the former, since O2 and H atoms lie on the same halfspace individuated by the O4−Y−O6 atoms.

Following this point of view, also the respective angles result exchanged, being the O2−Y−O6 angle smaller than the O4−Y−O2 one, while the O2−Y−O6 angle have almost the same value obtained with the first YH calculation; the same consideration hold for the H−O2−O4−O6 dihedral angle, being this value of 14°. Among the Y−Ba distances, only the Y−Ba3

changes significantly, being the Ba3 the nearest one to the proton, not affecting the volume of the protonated site.

**In-doped Fragment.** The AUG model for indium doped barium cerate is the one that better reproduce the geometrical features of this system; for this reason, this has been used as starting geometry to study the proton influence of an In-doped octahedral site, by performing one geometrical optimization as already discussed about the other protonated systems, whose results are reported in Table 4.7 Similarly to what we found for the protonated systems discussed since now, the distances between the octahedral cation and the oxygen atoms surrounding it show a strong deformation ranging from 2.03 to 2.27 Å. Comparing these values with those ones obtained for the corresponding unprotonated system, we find, once again, that the overall octahedral volume keeps almost the same value while the Y−Ba distance, in average, increases. Furthermore, a strong planar perturbation of the In−O distances appears, leaving unaltered the In−O1 and In−O2 axial distances. The longest and the shortest In−O distances are again the In−O4 and In−O3 ones, and the In−Ba3 distance value results the most enlarged among the In−Ba distances; accordingly, after inserting the proton, the volume of the proton environment increase. The O4−In−O2, O4−In−O6 and O2−In−O6 angles have smaller values than the starting ones, following the same trend of the corresponding values in the geometrical optimizations showed above. The H−O2−O4−O6 optimized dihedral angle results smaller than the corresponding one in the undoped and Y-doped structures.

**Gd-doped Fragment.** Modifications induced by the presence of one proton on a Gd-doped site have been studied by using the model Gd1 of the corresponding unprotonated geometry. Starting from this configuration, one proton has been added to the structure following the general prescriptions described in the introduction to this section, then the positions of $Ba_8GdO_6H$ moiety have been relaxed by setting the charge and multiplicity values at -1 and 1 respectively. Relevant distance and angle values so obtained are reported in the column Gd1−H of the Table 4.8. Although Gd1−H model has been built starting from the Gd1 one, that does not reproduce the experimental geometrical features of the system, calculations on it can be used as a probe to understand if correlation effects, found for Gd1 system, can be neglected when one proton lies near a Gd-doped site.

The Gd−O distances found are spread over a wide range from 2.06 to 2.32 Å. Comparing these values with the corresponding ones of the starting model, Gd−O mean distance remains almost the same, keeping nearly constant the octahedral volume, while the Gd−Ba mean distance increase, expanding the proton surrounding environment as for the other already analysed protonated systems. Inserting one proton into the structure, a strong

Table 4.7: Relevant geometrical parameters characterizing the central octahedron environment of the protonated In-doped orthorhombic, *Pmcn* In:$BaCeO_3$, fragment.

| distances[a]/ Å | AUG[b] | AUG-H[c] |
|---|---|---|
| In−O1 | 2.20 | 2.18 |
| In−O2 | 2.20 | 2.21 |
| In−O3 | 2.20 | 2.03 |
| In−O4 | 2.20 | 2.27 |
| In−O5 | 2.22 | 2.14 |
| In−O6 | 2.22 | 2.26 |
| <In−O>[d] | 2.21 | 2.18 |
| In−Ba1 | 3.70 | 4.05 |
| In−Ba2 | 3.75 | 3.68 |
| In−Ba3 | 3.53 | 3.57 |
| In−Ba4 | 3.67 | 3.63 |
| In−Ba5 | 3.67 | 3.71 |
| In−Ba6 | 3.53 | 3.49 |
| In−Ba7 | 3.75 | 4.05 |
| In−Ba8 | 3.70 | 3.60 |
| <In−Ba>[d] | 3.66 | 3.72 |
| O4−H | 1.10 | 0.95 |
| angles[e]/ ° | AUG | AUG-H |
| H−O4−Ce | 80.0 | 73.0 |
| H−O4−O2−O6 | 17.0 | 25.15 |

[a] For the atomic labelling see Figure 3.6.
[b] Geometrical parameters of the AUG system as presented in Table 4.3, used as starting input in the optimizations whose results are summarized in the AUG-H column. Values are reported for comparison purposes.
[c] Optimized values for the hydrogenated system with the proton in the stable position. [d] Mean values of the corresponding atomic distances.
[e] Planar and dihedral angle values of the specified atoms are reported. For the AUG system, values are a starting guess for proton position (see the text).

planar perturbation of the Gd−O distances occurs, leaving unaltered the Gd−O1 and Gd−O2 axial distances. Like what we found for the other protonated doped structures, the O4−Gd−O2, O4−Gd−O6 and O4−Gd−O6

Table 4.8: Relevant geometrical parameters characterizing the central octahedron environment of the protonated Gd-doped orthorhombic, *Pmcn* Gd:$BaCeO_3$, fragment.

| distances[a]/ Å | Gd1[b] | Gd1-H[c] | Gd2[b] | Gd2-H[d] |
|---|---|---|---|---|
| Gd−O1 | 2.16 | 2.15 | 2.19 | 2.30 |
| Gd−O2 | 2.16 | 2.16 | 2.19 | 2.38 |
| Gd−O3 | 2.18 | 2.06 | 2.19 | 2.16 |
| Gd−O4 | 2.18 | 2.32 | 2.19 | 2.44 |
| Gd−O5 | 2.19 | 2.14 | 2.19 | 2.30 |
| Gd−O6 | 2.19 | 2.23 | 2.19 | 2.32 |
| <Gd−O>[e] | 2.18 | 2.18 | 2.19 | 2.31 |
| Gd−Ba1 | 3.80 | 4.19 | 3.82 | 4.20 |
| Gd−Ba2 | 3.84 | 3.76 | 3.84 | 3.76 |
| Gd−Ba3 | 3.62 | 3.74 | 3.78 | 3.75 |
| Gd−Ba4 | 3.73 | 3.77 | 3.78 | 3.81 |
| Gd−Ba5 | 3.73 | 3.85 | 3.68 | 3.86 |
| Gd−Ba6 | 3.62 | 3.62 | 3.68 | 3.68 |
| Gd−Ba7 | 3.84 | 4.06 | 3.82 | 4.07 |
| Gd−Ba8 | 3.80 | 3.81 | 3.82 | 3.87 |
| <Gd−Ba>[e] | 3.75 | 3.85 | 3.78 | 3.87 |
| O4−H | 1.10 | 0.95 | 1.10 | 0.95 |
| angles[f]/ ° | Gd1 | Gd1-H | Gd2 | Gd2-H |
| H−O4−Ce | 80.0 | 82.3 | 80.0 | 73.1 |
| H−O4−O2−O6 | 17.0 | 34.2 | 17.0 | 25.7 |

[a] For the atomic labelling see figure Figure 3.4.
[b] Geometrical parameters of the Gd1 and Gd2 systems as presented in Table 4.4, used as starting input in the optimizations whose results are summarized in the Gd1-H and Gd2-H column. Values are reported for comparison purposes.
[c] Optimized values for the hydrogenated system with the proton in the stable position; for this system, charge and multiplicity have been set at -1 and 1, respectively.
[d] Optimized values for the hydrogenated system with the proton in the stable position; for this system, charge and multiplicity have been set at 0 and 2, respectively.
[e] Mean values of the corresponding atomic distances.
[f] Planar and dihedral angle values of the specified atoms are reported. For the Gd1 and Gd2 systems, values are a starting guess for proton position (see the text).

angles have smaller values than the starting ones, while the H−O2−O4−O6 optimized dihedral angle is larger than the corresponding one in the other

protonated doped models and comparable to the value it has in the protonated undoped system.

In order to deepen the study on the influence of the proton on the Gd-doped octahedral environment, we performed a further geometrical optimization, starting from the Gd2 model, and setting the charge and multiplicity values at 0 and 2 respectively. The system built in this way has been called Gd2-H and relevant distances and angles obtained are reported in the corresponding column in the Table 4.8.

In the same way as the just discussed closed shell calculation, the features of the Gd−O distances hold, with Gd−O4 and Gd−O3 the longest and shortest ones. Comparing these results with the Gd1-H calculation, the Gd−Ba mean distance appears to be almost the same; however, Gd−O distances increase expanding the octahedral site and producing the same effect when Gd substitutes for cerium in unprotonated systems.

As found for the other protonated doped systems, the X−O1 and X−O2 distances (i.e. the axial ones) have nearly the same value both before and after inserting the proton into the structure; since their mean value for Gd2-H system (2.34 Å) is the same found in EXAFS experiment [164], we can infer that, in presence of one proton in the Gd-doped octahedral environment, correlation effects, relevant for the unprotonated system, do not contribute in a significant way to the determination of the dopant local geometry.

### 4.1.3 Electronic Population Analysis

In order to deepen our insight into the electronic characteristics of the $Ba_8XO_6$ moiety and to shed light on the effects of the dopant species on the corresponding local electronic properties, we applied C-SPA/P-DOS analysis and *M-ca* approach on the *Pmcn* $X{:}Ba_8Ce_{26}O_{62}$ fragments, on systems treated at the same level of calculation, namely the Ce1, CR and In0 ones, in the hypothesis that local electronic changes could be related to changes in the protonic conduction properties.

$X{:}Ba_8Ce_{26}O_{62}$ fragment was clustered to form four sets of atomic species to be simultaneously analysed: *i*) the $Ba_8XO_6$ moiety, *ii*) the $Ba_8$ atomic cluster, *iii*) the X species and *iv*) the $O_6$ atomic cluster of the central octahedron. The $\rho$ *vs.* $\varepsilon$ curves of these atomic groups are reported in Figure 4.1 with the bar representation of the $X{:}Ba_8Ce_{26}O_{62}$ fragment eigenstates. The $\rho$ curves represent the orbital contribution of a given atomic set, among those considered, to the MOs characterizing the $Ba_8XO_6$ central moiety, while the abscissa $\varepsilon$ fits the energy range considered.

An energy range, close to the HOMO region and interesting the $Ba_8XO_6$ central moiety of the $X{:}Ba_8Ce_{26}O_{62}$ fragment, is analysed in the following. At first, it should be noticed that, in the considered energy limits, the eigenvalue ranges of the whole $X{:}Ba_8Ce_{26}O_{62}$ fragment, individuated by the red bars, are roughly coincident with the P-DOS peak widths of the selected

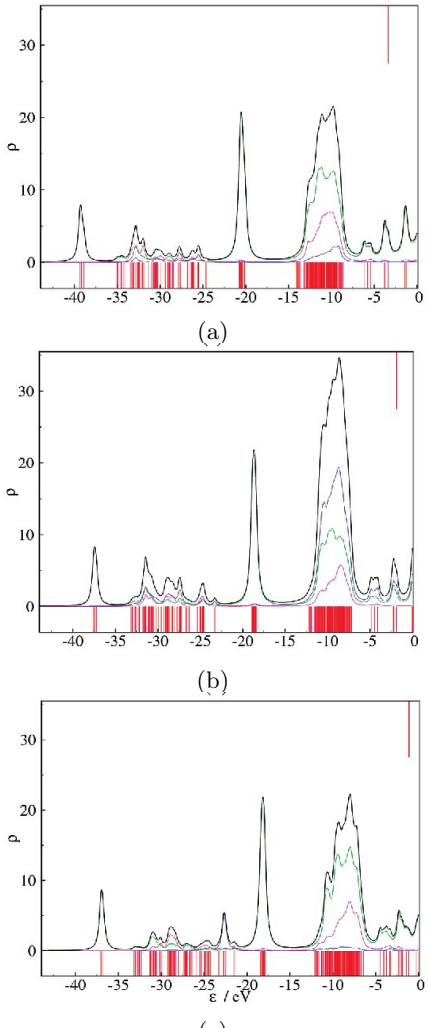


Figure 4.1: C-SPA/P-DOS analysis of the X:$Ba_8Ce_{26}O_{62}$ fragment: orbital contribution of atomic sets, included in the $Ba_8XO_6$ central cluster ($Ba_8$ group: green line; X atom: blue line; $O_6$ group: purple line; $Ba_8XO_6$ moiety: black line), to the $Ba_8\Xi O_6$ MOs against energy values, $\rho$ *vs.* $\varepsilon$: (a) undoped, (b) Y-doped, (c) In-doped *Pmcn* systems. The red bars individuate the $i$ eigenstates of the whole X:$Ba_8Ce_{26}O_{62}$ fragment. The $\rho$ lines are obtained by a convolution of fixed-width Lorentzian curves centred on the energy bin used in the DOS analysis, being the height proportional to the weight of the AO set contribution in the bin. The red line on the top shows the border between HOMO and LUMO.

atomic sets belonging to the $Ba_8XO_6$ moiety. Moreover, the presence of two characteristic peaks can at first be observed in Figure 4.1. These are centred at about -38.0 and -19.9 eV and correspond to MOs almost entirely

constructed with the $Ba_8$ atomic orbitals, independently of the X cation.

Concerning the Y-doped system, it can be noticed that the yttrium together with the barium and oxygen AOs are the main contributors to the MOs corresponding to the eigenvalues in the range -15.0 ÷ -6.0 eV. Conversely, in the undoped systems, the cerium atom of the central octahedron clearly gives a smaller contribution to the MOs in this energy range as well as in the remaining range here analysed. Interestingly, the MOs related to the eigenvalues in the range starting from ca. -6.0 eV up to the HOMO region are entirely attributable to the barium AOs in the undoped systems while in the Y-doped system, the same MOs seem to be produced by a mixing of barium and yttrium AOs. The C-SPA/P-DOS plot of the In0 system seems to strictly resemble that of the undoped system, being however the indium AO contribution mainly centred at ca. -22.7 eV, where the MOs seem to be entirely determined by the same indium AOs.

Moreover, the substitution of cerium with yttrium atoms seems to localize a negative charge on the doped sites [86]. Following the *M-ca* procedure, this characteristic is plainly captured by our calculations, which show a decrease (towards negative values) of the Mulliken charge on the Y-substituted site by about -2 au, referring to the same calculations used for the C-SPA/P-DOS analysis.

Interestingly, this effect is not observed in the In-doped fragment, which conversely is characterized by an increase, ca. +0.4 au, of positive charge on the indium site in respect of the undoped one. Therefore, with the caution that has to be deserved in considering and comparing Mulliken charges, we can infer an opposite local behaviour of In-doped and Y-doped materials. The speculation above is supported by the observation that all the saturated oxygens but the octahedral ones, have very similar Mulliken charge, irrespective of the X:$Ba_8Ce_{26}O_{62}$ fragment considered, while the average Mulliken charge of the oxygens on the central octahedron has a characteristic behaviour oppositely related to that of the charge of the central atom inside it. The average charge difference on the oxygens surrounding yttrium and indium, taking as zero the average charge of the oxygens neighbouring cerium, is indeed ca. +0.2 and -0.2 au. These findings are indeed in agreement with a higher local basicity of the $XO_6$ moiety, in the case of In with respect to Y derivatives. The considerations above and the inspection of Figure 4.1, allow us to explain the larger miscibility and the lower conductivity of indium respecting yttrium atoms in the $BaCeO_3$ perovskite structures [86, 156].

Concerning the miscibility, it can be argued that indium, although inducing local shrinking distortions, caused by its smaller size, could be introduced in the $BaCeO_3$ materials in any amount since its AOs seems to behave like those of the Ce atom – see the Ce- and In- contribution to the large peak around 10 eV in Figure 4.1. An opposite behaviour is conversely shown by the yttrium centre that strongly interacts with the neighbouring

oxygen and barium atoms and induces local isotropic expansion of the surrounding octahedron environment (see section 4.1.1). This could contribute to the experimentally observed structural instability, producing un-mixing phenomena in the Y:$BaCeO_3$ compounds [85].

With respect to the conductivity, it can be inferred that the contraction of the central octahedron including the dopant, observed in the case of the In:$BaCeO_3$ derivatives, should cause a reduced ability in the proton transport. This fact coupled with the higher electron charge, determined by *M-ca*, on the oxygens surrounding the indium atom in respect to the yttrium one, easily could explain the reduced conductivity of the In-doped materials [86, 156], since the smaller doped octahedron should have limited exchange capability with neighbouring octahedrons (even more limited if the latter were also doped and as a consequence smaller) while the higher negative charge should even increase the resistance of the proton diffusion from the same In-doped octahedrons. Moreover, a proton moving from one oxygen of the latter to one of an undoped octahedron has to overcome an unfavourable charge gradient — protons have actually to move towards more positive sites — at variance with the event involved in the proton displacement from the oxygens of the Y-doped to the oxygens of the undoped octahedrons. This is in agreement with the interpretation proposed in [20] which directly relates the conductivity of a doped $BaCeO_3$ material to the basicity variations of the oxygen octahedral environments.

Summarizing, the oxygen net, own of the $BaCeO_3$ perovskite derivatives, defines a complex allocation matrix for the structural protons. This allows one to hypothesize the existence of an extended conformational space, defining the proton placement in the X:$BaCeO_3$ material bulk. However, it is already possible to hypothesize that preferred placements on oxygen site in the octahedral arrangement — in the order: $InO_6 > CeO_6 > YO_6$ — as well as preferential inter-octahedral diffusion way — in the order: $YO_6 \rightarrow CeO_6 > CeO_6 \rightarrow CeO_6 > InO_6 \rightarrow CeO_6$ — can prevail for protons belonging to $BaCeO_3$ perovskite derivatives.

Final considerations deserve the un-mixing phenomena characterizing the Y:$BaCeO_3$ materials [86]. Figure 4.1 reports the $\rho$ *vs.* $\varepsilon$ plot of the 2 Y:$Ba_8Ce_{26}O_{62}$ fragment. The main characteristics concern the presence of two broad bands in the ranges -40 ÷ -35 eV and -28 ÷ -10 eV, respectively and the shift to lower energy values of the bands that we attributed to effects produced by the barium AOs. In fact, the two broad bands have the same properties — specifically a large mix of Ba, O, and Y AOs — of the band centred at ca. -10 eV already found when considering the mono-doped Y fragment. More interestingly, a remarkable contribution of the lateral Y atom is also found in these bands. Of course, a symmetric behaviour, here not shown, of the central Y AOs is observed on the MOs formed by yttrium, barium and oxygen atoms defining the lateral Y atom environment. These interactions, in presence of high percentage of yttrium atoms in barium cer-

ate matrices, reinforce the structural instability mentioned above and could be straightforwardly related to the occurrence of $YO_6$ moieties' clustering, which could induce the experimentally observed un-mixing phenomena of the Y:$BaCeO_3$ derivatives, with production of yttrium and barium oxide species [86].

## 4.2 Double Substitution Model

Following the suggestions given by the results obtained with the unprotonated Y:$BaCeO_3$ models discussed in the preceding section, the *Double Substitution Model* is intended in the aim to investigate the possible local clustering of the Y atom in substituting for the Ce one. As for the *Single Substitution Model*, it will be shown that constraints on electronic and geometric structure do not compromise the reliability of the results. Since only undoped and Y-doped moieties will be investigated, the computational outcomes will be grouped by distinguishing between protonated and unprotonated structures only, highlighting how the structural features change after progressive substitutions.

### 4.2.1 Unprotonated Fragments

The choice to consider CeCe, CeY and YY:$Ba_{12}Ce_{22}O_{61}H_2$ systems is related to their representation ability of the different environments that should characterize Y-doped $BaCeO_3$ materials. The experimental structure parameters used to start the calculation on the XZ:$Ba_{12}Ce_{22}O_{61}H_2$ fragments were determined at room-temperature by neutron powder diffraction (NPD) [118]. Relevant relaxed distances and angles obtained after optimizations are reported in Table 4.9.

Concerning the CeCe systems (i.e. X=Z=Ce), the three oxygen atom sets {O1, O3, O2, O4}, {O1, O5, O2, O6}, {O4, O6, O3, O5} individuate three different crossing planes that include into their intersection the central cerium atom, both before and after the calculations. In each of these planes, two couples of oxygen atoms, together with the cerium atom, single out two incident lines, making two opposite-to-the-vertex pair of angles. The same holds true for the three sets {O4, O10, O9, O11}, {O7, O10, O8, O11}, {O7, O4, O8, O9} of oxygen centres. This result shows that the calculated atomic arrangements of the central clusters fit, as previously reported, into the average long-range structure experimentally determined by diffraction analysis, without introducing large distortion. Inspecting 4.9, we see that, despite the presence of two short values (X−O3 = Z−O9 = 2.12 Å), the calculated Ce−O distances are in agreement with the experimental ones.

As a matter of fact, molecular dynamics simulations performed on yttrium-doped barium zirconate perovskites (see chapter 6), also show a characteristic local anisotropy around the zirconium centres [117]. However, the

Table 4.9: Relevant geometric parameters characterizing the $XZBa_4O_{11}$ environment of the unprotonated orthorhombic *Pmcn* Y:$BaCeO_3$ calculated models.

| distances[a]/ Å | CeCe[b] | YY[b] | CeY[b] | distances[a]/ Å | CeCe[b] | YY[b] | CeY[b] |
|---|---|---|---|---|---|---|---|
| X−Ba1 | 3.65 | 3.54 | 3.59 | Z−Ba1 | 3.82 | 3.69 | 3.78 |
| X−Ba2 | 3.80 | 3.72 | 3.75 | Z−Ba2 | 3.83 | 3.82 | 3.82 |
| X−Ba3 | 3.91 | 3.74 | 3.93 | Z−Ba3 | 3.75 | 3.65 | 3.76 |
| X−Ba4 | 3.77 | 3.67 | 3.68 | Z−Ba4 | 3.70 | 3.58 | 3.62 |
| <X−Ba>[c] | 3.78 | 3.67 | 3.74 | <Z−Ba>[c] | 3.78 | 3.68 | 3.74 |
| X−O1 | 2.24 | 2.34 | 2.29 | Z−O4 | 2.26 | 2.29 | 2.22 |
| X−O2 | 2.24 | 2.28 | 2.27 | Z−O7 | 2.26 | 2.33 | 2.29 |
| X−O3 | 2.12 | 2.16 | 2.23 | Z−O8 | 2.24 | 2.29 | 2.24 |
| X−O4 | 2.27 | 2.28 | 2.31 | Z−O9 | 2.12 | 2.17 | 2.14 |
| X−O5 | 2.28 | 2.26 | 2.28 | Z−O10 | 2.28 | 2.28 | 2.30 |
| X−O6 | 2.27 | 2.33 | 2.29 | Z−O11 | 2.27 | 2.35 | 2.24 |
| <X−O>[c] | 2.24 | 2.27 | 2.28 | <Z−O>[c] | 2.24 | 2.28 | 2.24 |
| <XZ−Ba>[d] | 3.78 | 3.68 | 3.74 | <XZ−O>[d] | 2.24 | 2.28 | 2.26 |

[a] The reported atomic labelling is coherent with that of Figure 3.5. [b] Geometric parameters that characterize the XZ:$Ba_{12}Ce_{22}O_{61}H_2$ fragments, being XZ=CeCe, CeY and YY. [c] Average values calculated on homonym distance parameters. The corresponding averaged EXAFS values are shown in Tables 4.1 and 4.2 [85].
[d] Average values calculated on the distance parameters involving, separately, either Ba or O atoms and both the X and Z. The corresponding averaged NPD values [118] are reported in Table 4.1. It is, in passing, recalled that the NPD crystallographic analysis cannot distinguish between yttrium and cerium atoms [165, 84].

shortest Zr−O distances, isolated at 3K and corresponding to the Ce−O ones present in the title Y:$BaCeO_3$ derivatives, already disappear at 77K. As a consequence, the distance anisotropy, characterizing the surrounding environments of the zirconium centres, is removed [117]. The shortest distances characterizing different perovskite materials, and namely Y:$BaCeO_3$ derivatives, could hence disappear because of the occurrence of thermal motions. In the present case this fact could contribute to reproduce the found experimental Ce−O values. The Ba−Ce distances are arranged according to a bimodal distribution centred at around 3.68 and 3.82 Å. The first set of distances is characterized by the presence of the X−Ba4 and Z−Ba1 interactions while the second one by the remaining six Ba−Ce interactions. Both the average values and their relative weights (i.e. 1:3) are in very well agreement with the corresponding parameters found by the EXAFS experiments (see note *c* in Table 4.9).

As mentioned in the preceding sections, also the Y−O distances, present in the Y:$BaCeO_3$ materials, experimentally showed distinctive bimodal distributions [86]. In order to find a possible origin of this feature, we already

proposed a Y-doped model (see paragraph **Y-doped fragments** in section 4.1.1), in which two clustered yttrium atoms were each other bound by one bridge oxygen centre. The present model is actually characterized by the same Y−O−Y moiety but, in addition, shows larger local details around the octahedral yttrium centres; hence, it can be considered, as already stated, an extension of the former model.

In this, both the octahedral centres of the XZ:$Ba_{12}Ce_{22}O_{61}H_2$ fragment were yttrium atoms (i.e. X = Z = Y) while the inner $XZBa_4O_{11}$ moiety was optimized inside a surrounding rigid cage. Relevant distances are shown in Table 4.9. Three characteristic Y−O distances can be recognized, at about 2.17, 2.28 and 2.34 Å. These distance values show relative weight of 1/6, 3/6 and 2/6, respectively. As argued for the shortest Ce−O distance, found in the CeCe:$Ba_{12}Ce_{22}O_{61}H_2$ fragment, the short and the medium Y−O distances characterizing the YY:$Ba_{12}Ce_{22}O_{61}H_2$ fragment, due to thermal motion, could together contribute to define the weight of the shorter Y−O distance of the experimentally found bimodal distribution.

In this case, the calculated average distances (2.25 and 2.34 Å) as well as their relative weights (4/6 and 2/6) would result in excellent agreement with the EXAFS findings (see note *c* in Table 4.9). The Ba−Y distances are spread in the range 3.54÷3.82 Å, showing a mean value of 3.68 Å. The slight disagreement with the experimental values (see notes *c* and *d* of Table 4.9) can be explained by taking into account the geometric and stoichiometric characteristics of the XZ:$Ba_{12}Ce_{22}O_{61}H_2$ fragments (see Figures 3.3 and 3.7). In fact, in the analysis of the YY system only the four central Ba atoms are considered in evaluating the average Ba−Y distance. Whereas, a more correct evaluation should at least involve the consideration of the two sets of four Ba atoms at the left and at the right side of the X and Z centres, respectively. These are in-between Ce and Y atoms and are fixed in the YY fragment. For this reason the characteristics of the Ba−Y distances will deserve a deeper discussion and will be reexamined considering the following CeY fragment.

The latter, built by substituting one of the Ce atoms of the inner octahedra with one Y atom (i.e. X = Y, Z = Ce), mimics local arrangements of the border zone characterizing Y-doped sites. As usual, a partial geometric optimization was performed in order to study the local changes induced on the structure. The starting geometry was unchanged with respect to those of the previous calculations. Significant calculated distances are reported in Table 4.9. The average <Ce−O> value (2.24 Å) is the same as that we already found for the CeCe system, but with a larger spread of the value. Moreover, the first oxygen coordination shell of the Y atoms resulted more expanded than that characterizing the Ce atoms, present in the other inner octahedron of the same fragment. In particular, the Y−O distances are distributed in a range varying from 2.23 to 2.31 Å while the average distance is equal to 2.28 Å. However, the Y−O distance spread does not allow one to

single out an unambiguous bimodal distribution, as conversely suggested by the EXAFS data collected on the Y:$BaCeO_3$ systems [86]. It has conversely to be stressed that the interesting geometric property already observed for the CeCe fragment, regarding the pair of opposite-to-the-vertex angles, is still holding in the CeY system.

Finally, the EXAFS Ba−Ce distances are better reproduced by the CeCe than the CeY system. This result, as previously discussed, has to be connected to the double substituted systems here studied, hence to the fact that the CeCe fragment are, for statistical reasons, more suitable than the CeY fragment for analysing the Ba−Ce distances. On the contrary, as before prefigured in discussing the YY fragment, the Ba−Y distances, as evaluated by the CeY fragment, are well arranged in a wide range according to a single distribution centred around 3.74 Å, in agreement with the single Ba−Y distance found by EXAFS experiments on Y:$BaCeO_3$ materials.

### 4.2.2 Protonated Fragments.

Suitably modified XZ:$Ba_{12}Ce_{22}O_{61}H_2$ fragments were also employed to analyse the effects of the proton on the environment of the octahedral centres. In these structures one of the two hydrogen atoms was removed from the original position and placed close to the O4 centre. In starting the optimization, the O4−H distance, H−O4−X planar angle and H−O4−X−O2 dihedral angle were set to 0.95 Å, 80.0°and 45.0°, irrespective of the protonated system considered. Relevant distances and angles obtained after the optimizations, also including the hydrogen coordinate relaxation, are reported in Table 4.10.

The analysis of the latter shows that when the proton is included in the inner octahedra environment of the fragments, it modifies to some extent the starting local geometric arrangements (i.e. those of the unprotonated fragments). In particular, the values of the X−O and Z−O distances of the CeCe systems were changed, especially along the X−O4−Z moiety. Indeed, the X−O4 and Z−O4 distances increased whereas the opposite ones - that is the X−O3 and Z−O9 distances - similarly to the X−O5 and Z−O8 distances, decreased. As a result, the volume of the $XZO_{11}$ inner octahedra in the CeCe fragment resulted almost unchanged in agreement with analogous behaviours that have been observed in studying single octahedron models of protonated $BaCeO_3$ fragments [117]. Also the X−Ba and Z−Ba distances increased, in this way, expanding the surrounding barium coordination shell, characterizing the CeCe system. The main structural distortions discussed above for the CeCe system also affect the protonated YY and CeY systems.

However, in the CeY fragment as well as for the CeCe one, the octahedral volume remains unchanged while in the YY fragment the distribution of the Y−O distances were centred, as for the homonym unprotonated fragment, around the values found by the EXAFS analysis [86]. With respect to this,

Table 4.10: Relevant geometric parameters characterizing the $XZBa_4O_{11}$ environment of the protonated orthorhombic *Pmcn* Y:$BaCeO_3$ calculated models.

| distances[a]/ Å | CeCe | YY | CeY | distances[a]/ Å | CeCe | YY | CeY |
|---|---|---|---|---|---|---|---|
| X−Ba1 | 3.84 | 3.79 | 3.78 | Z−Ba1 | 4.00 | 3.94 | 3.95 |
| X−Ba2 | 3.97 | 3.92 | 3.94 | Z−Ba2 | 4.05 | 3.97 | 4.01 |
| X−Ba3 | 4.05 | 3.86 | 4.05 | Z−Ba3 | 3.86 | 3.72 | 3.87 |
| X−Ba4 | 3.87 | 3.80 | 3.81 | Z−Ba4 | 3.80 | 3.70 | 3.74 |
| <X−Ba>[b] | 3.93 | 3.84 | 3.89 | <Z−Ba>[b] | 3.93 | 3.83 | 3.89 |
| X−O1 | 2.18 | 2.31 | 2.26 | Z−O4 | 2.40 | 2.37 | 2.41 |
| X−O2 | 2.23 | 2.25 | 2.28 | Z−O7 | 2.24 | 2.30 | 2.25 |
| X−O3 | 2.10 | 2.14 | 2.13 | Z−O8 | 2.20 | 2.24 | 2.21 |
| X−O4 | 2.40 | 2.37 | 2.37 | Z−O9 | 2.04 | 2.09 | 2.06 |
| X−O5 | 2.18 | 2.22 | 2.25 | Z−O10 | 2.26 | 2.27 | 2.26 |
| X−O6 | 2.26 | 2.30 | 2.28 | Z−O11 | 2.26 | 2.34 | 2.23 |
| <X−O>[b] | 2.22 | 2.26 | 2.26 | <Z−O>[b] | 2.23 | 2.27 | 2.24 |
| <XZ−Ba>[c] | 3.93 | 3.84 | 3.89 | H−X[d] | 2.44 | 2.43 | 2.33 |
| <XZ−O>[c] | 2.23 | 2.26 | 2.24 | H−Z[d] | 2.48 | 2.47 | 2.58 |
| angles[a]/ ° | CeCe | YY | CeY | angles[a]/ ° | CeCe | YY | CeY |
| H−O4−X | 81.3 | 82.1 | 75.8 | H−O4−Z | 83.8 | 83.4 | 89.5 |
| H−O4−X−O2 | 4.9 | 8.0 | 8.0 | — | — | — | — |

[a] For the indexing of distances and angles, see Figure 3.5.
[b] Average values calculated on homonym distance parameters. The corresponding averaged EXAFS values are shown in Tables 4.1 and 4.2 [85]. [c] Average values calculated on the distance parameters involving, separately, either Ba or O atoms and both the X and Z centres. For corresponding experimental parameter references, see Tables 4.1 and 4.2 [118] [d] In the optimizations of the protonated systems, one of the external hydrogen atoms present in the XZ:$Ba_{12}Ce_{22}O_{61}H_2$ fragment (see Figure 3.3) is placed close to the O4 centre of the $XZO_{11}$ moiety (see Figure 3.7) and relaxed with the latter.

it has to be stressed that the bimodal distribution, corresponding to the protonated fragments, is characterized by a large spread of the distance values that is also in agreement with the large Debye-Waller factor reported in [86].

Finally, the H−O4−Z and H−O4−X angles as well as the H−O4−X−O2 dihedral angles are quite similar irrespective of the considered system; in particular, due to the small dihedral angle value found for the different XZ systems, we can regard the proton as lying onto the plane individuated by the O4, X and O2 centres, an effect of the directionality of the O−H bond embedded in the local octahedral environment.

### 4.2.3 Electronic Population Analysis

In order to deepen our insight into the electronic properties of the $XZBa_4O_{11}$ moiety and to analyse the effects of the yttrium centres on its local environment, we performed C-SPA/P-DOS and *M-ca* analyses on the calculated *Pmcn* XZ:$Ba_{12}Ce_{22}O_{61}H_2$ fragment, hypothesizing that local electronic rearrangements could be related to changes in the protonic conduction. The XZ:$Ba_{12}Ce_{22}O_{61}H_2$ fragment was clustered to form seven sets of atomic species to analyse simultaneously: *i*) the $XZBa_4O_{11}$ moiety, *ii*) the $Ba_4$ atomic cluster in-between the central octahedra, *iii*) the X and *iv*) Z cations, *v*) the O4 centre, and finally the clusters *vi*) $O_X$ and (vii) $O_Z$ formed by the central octahedral oxygen atoms — except for the O4 centre — around the X and Z cation, respectively.

The $\rho$ vs. $\varepsilon$ curves of Figures 4.2 and 4.3 represent the orbital contribution of a given atomic set to the MOs of the XZ:$Ba_{12}Ce_{22}O_{61}H_2$ fragment while the abscissa values fit the energy range considered. The involved atomic sets are either those of the systems *i*) - *vii*), belonging to the $XZBa_4O_{11}$ moiety, or that of the whole XZ:$Ba_{12}Ce_{22}O_{61}H_2$ fragment. It should be, at first, noticed that the eigenvalue ranges individuated by the grouped red bar sets that characterize the XZ:$Ba_{12}Ce_{22}O_{61}H_2$ fragment peaks are nearly coincident, irrespective of the XZ system, with the P-DOS peak widths of the *i*) - *vii*) atomic sets, which belong to the $XZBa_4O_{11}$ moiety. The presence of two sharp peaks can be also observed for all the different systems; they are centred at about -39.0 and -20.0 eV. These correspond to MOs almost entirely attributable to the $Ba_4$ cluster and are always present regardless of the considered protonated and unprotonated XZ system. Another common feature of the C-SPA curves concerns the $O_X$ and (vii) $O_Z$ orbital contributions, which in any case overlap (see Figures 4.2 and 4.3). The findings above show that both the octahedral sites are electronically similar, hence anisotropic effects can be excluded for the different model clusters.

Concerning the YY system, we see that for eigenvalues ranging from -16.0 to -5.0 eV, both the yttrium atoms, together with the $Ba_4$ moiety, represent the main contributors to the corresponding MOs range; on the contrary, in the CeCe system, the cerium atoms of the inner octahedra give a smaller contribution to MOs in that energy range. In the latter system, MOs running in the interval included between about -5.0 eV and the HOMO region are entirely attributable to the barium AOs while in both the systems containing yttrium, the Y and Ba AOs mix together, producing MOs in the same energy range. These last features, together with the characteristic barium peaks, were already observed for eigenvalues in the same energetic region characterizing *single substitution model* fragments.

The C-SPA of the protonated and unprotonated systems show quite similar behaviour. However, a characteristic small peak, caused by the AO

contribution of the $Ba_4$ moiety and of the O4 centre, can be observed for all the protonated XZ fragment at ca. -17.5 eV. In fact, the insertion of the hydrogen atom into the $XZO_{11}$ inner octahedral environment would seem to modify the orbital contribution of just the $Ba_4$ moiety and the O4 centre, producing a MO finger-print for the protonated systems in the eigenvalue interval ranging in-between -20.0 and -16.0 eV. In passing, it is here recalled that an analogous behaviour have been also observed in protonated and unprotonated *single substitution model* structures [117].

It was already argued that the substitution of cerium with yttrium atoms in perovskite materials localize an increased electronic density around the Y-doped sites [86]. According to the *M-ca* procedure, this feature, as shown by 4.11, is captured by the CeY and YY systems, which actually show a decrease towards more negative values of the Mulliken charge on the oxygen atom placed in-between the X and Z centres when at least one of these is an yttrium atom. Table 4.11 reports the Mulliken charges of the atoms that have mainly modified the C-SPA curves of the protonated with respect to the unprotonated XZ:$Ba_{12}Ce_{22}O_{61}H_2$ fragments, i.e. the O4 atom — and for completeness the remaining oxygen atoms of the central octahedra —, the barium atoms in-between the octahedra and the hydrogen that characterizes the protonated systems. Interestingly, the analysis of the oxygen environments characterizing the XZ systems allowed us to fix local charge configurations, able to drive proton diffusion in the title materials [84].

Table 4.11 clearly points that the different XZ systems are characterized by homogeneous charge behaviours. The unprotonated CeCe system, as an example, shows equal values irrespective of the oxygen centre considered. A similar situation also holds for the unprotonated CeY and YY systems, besides a characteristic rise of the negative charge values that can be observed for the X−O−Z bridging O4 centres. It is interesting to notice that the average oxygen charge present in the external-frame is very close to -1.4 au, as found for the oxygens of the inner octahedra in the CeCe system, both in the unprotonated and protonated systems and irrespective of the nature of the X and Z centres; this contributing to validate the here proposed models. As expected, the distribution of the charges in the barium centres show a more isotropic behaviour in the system not containing Y atoms. This fact shows the ability of the doping atoms to modify both the local structural properties and the corresponding local electronic environments.

The introduction of hydrogen in the central octahedra, corresponding to the formation of the protonated models, clearly produces changes in the charge distribution of the oxygen atoms. In particular, while we can notice a decrease of the absolute value in the O4 atom for all the systems, the hydrogen charges resulted higher of ca. 0.1 au in the YY with respect to the CeY and CeCe systems. Besides the changes on the O4 atoms, the remaining oxygen centres of the fragments are not very affected by the introduction of the hydrogen into the $XZO_{11}$ inner octahedra and the average value of

Table 4.11: Mulliken charges of relevant atomic centres, characterizing the $XZBa_4O_{11}$ environment of the unprotonated and protonated orthorhombic *Pmcn* Y:$BaCeO_3$ calculated models.

| atomic centre[a] | CeCe[b] | YY[b] | CeY[b] |
|---|---|---|---|
| Ba1 | 0.2 \| 0.0 | 0.9 \| 0.1 | 0.0 \| -0.1 |
| Ba2 | 0.1 \|-0.2 | 0.1 \|-0.1 | 0.2 \|-0.1 |
| Ba3 | 0.1 \| 0.0 | 0.9 \| 0.9 | 0.7 \| 0.6 |
| Ba4 | 0.2 \| 0.4 | 1.2 \| 1.0 | 1.0 \| 0.8 |
| O1 | -1.4 \|-1.4 | -1.4 \|-1.4 | -1.4 \|-1.3 |
| O2 | -1.4 \|-1.4 | -1.4 \|-1.5 | -1.4 \|-1.5 |
| O3 | -1.4 \|-1.4 | -1.5 \|-1.3 | -1.5 \|-1.3 |
| O4 | -1.4 \|-0.9 | -1.8 \|-0.9 | -1.6 \|-0.8 |
| O5 | -1.4 \|-1.3 | -1.4 \|-1.4 | -1.4 \|-1.4 |
| O6 | -1.4 \|-1.3 | -1.4 \|-1.3 | -1.4 \|-1.3 |
| O7 | -1.4 \|-1.4 | -1.4 \|-1.3 | -1.4 \|-1.4 |
| O8 | -1.4 \|-1.4 | -1.4 \|-1.4 | -1.4 \|-1.4 |
| O9 | -1.4 \|-1.3 | -1.4 \|-1.3 | -1.4 \|-1.3 |
| O10 | -1.4 \|-1.3 | -1.4 \|-1.3 | -1.4 \|-1.3 |
| O11 | -1.4 \|-1.4 | -1.4 \|-1.4 | -1.4 \|-1.4 |
| H | — \| 0.3 | — \| 0.4 | — \|0.3 |

[a] The reported atomic labelling is coherent with that of 3.7. [b] The vertical bar employed for the value representation distinguishes between the Mulliken charges of the unprotonated (left) and protonated (right) model.

the Mulliken charges of the protonated XZ systems remains quite similar to that of the unprotonated ones.

Taking into consideration the charge distributions that characterize the different XZ systems, it is possible to infer hypotheses on the hydrogen diffusion mechanism occurring in the Y-doped $BaCeO_3$ materials. In doing this, we hypothesize that a large amount of di-yttrium (clustered) sites are formed in the Y-doped $BaCeO_3$ materials and we assume, as already stated, that the different XZ systems are representative of different local situations in the same materials. The mimicking ability of the YY fragment in reproducing the experimental structural evidences concerning the bimodal $Y-O$ distance distribution is, in our opinion, a plausible reason to state the first inference while the second is supported by the homogeneous oxygen charge behaviour, own of the external-frame of the different fragments, that is coherent with the local properties of the CeY and CeCe systems.

The findings reported in Table 4.11 — and in particular the relative charge value characterizing the O4 with respect to the neighbouring {O5, O6, O10, O11} horizontal and {O1, O2, O7, O8} vertical oxygens — see

Figure 3.5, show that the hydrogen centre can diffuse in the bulk being, in any case, favoured by the present charge gradients, independently of the considered $XZO_{11}$ inner octahedra pairs, i.e. CeCe, CeY and YY. Hence, it is clear that the intra-octahedral diffusions should be always allowed, irrespective of the nature of the metallic centre inside the octahedron. Whereas, the inter-octahedral diffusions, which clearly are also not prevented by opposite charge gradients, should have lower occurrence probabilities due to the larger distance "jump" needed [35, 124].

The local charge density variations, connected to the local basicity rearrangements, [166] occurring in the material bulk and their influence on the proton diffusion deserve a final comment. It has been reported that the local basicity of the sites could play an important role in driving the conductivity phenomena of the Y-doped $BaCeO_3$ perovskite materials [84, 166]. At variance with this, by the *M-ca* approach summarized in table 4.11 and admitting that the hydrogen diffusivity mostly occur by intra-octahedral motions, it seems that the local and static charge gradients, produced by the clustering of the defects introduced with the doping procedure, are not able to affect the hydrogen diffusion. This peculiarity actually would occur because the hydrogen centres during the diffusion processes should be in any case able to dynamically change their neighbouring environments and the surrounding oxygen properties leaving, however, unchanged the hydrogen diffusion ability, because of the favourable and almost isotropic charge gradients always occurring in the intra-octahedral O→O jumps.

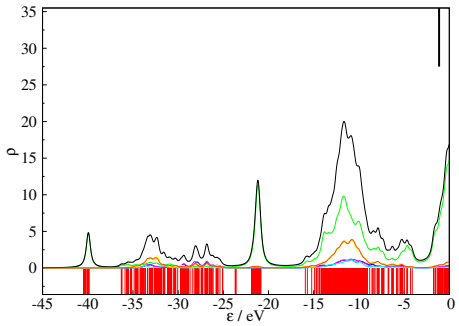


(a)

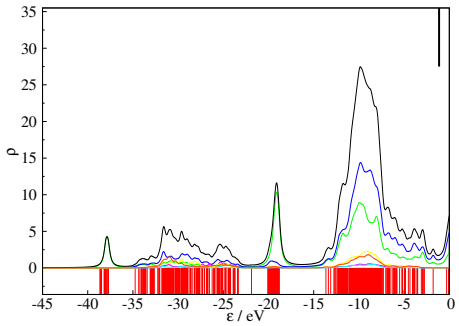


(b)

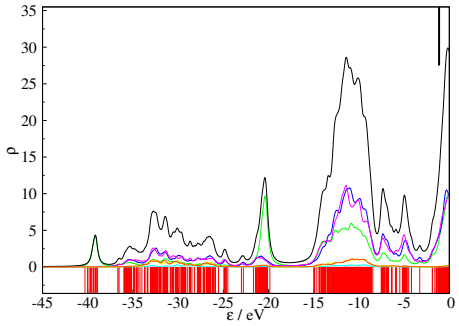


(c)

Figure 4.2: C-SPA/P-DOS analysis of the XZ:$Ba_{12}Ce_{22}O_{61}H_2$ fragments when hydrogen is not embedded in the framework, XZ = CeCe (a), CeY (b), YY (c): orbital contribution of atomic sets included in the $XZBa_4O_{11}$ moiety to the MOs of the same moiety against energy values, ($\rho$ vs. $\varepsilon$). $Ba_4$ group, green line; X atom, blue line; Z atom, purple line; O4 atom, light blue line; $O_X$ moiety, red line; $O_Z$ moiety, yellow line; $XZBa_4O_{11}$ cluster: black line. The red bars individuate the eigenstates of the whole XZ:$Ba_{12}Ce_{22}O_{61}H_2$ fragment. The $\rho$ lines are obtained by a convolution of fixed-width Lorentzian curves centred on the energy bin used in the DOS analysis, being the height proportional to the weight of the AO set contribution in the bin. The black segment on the top individuates the HOMO-LUMO edge.

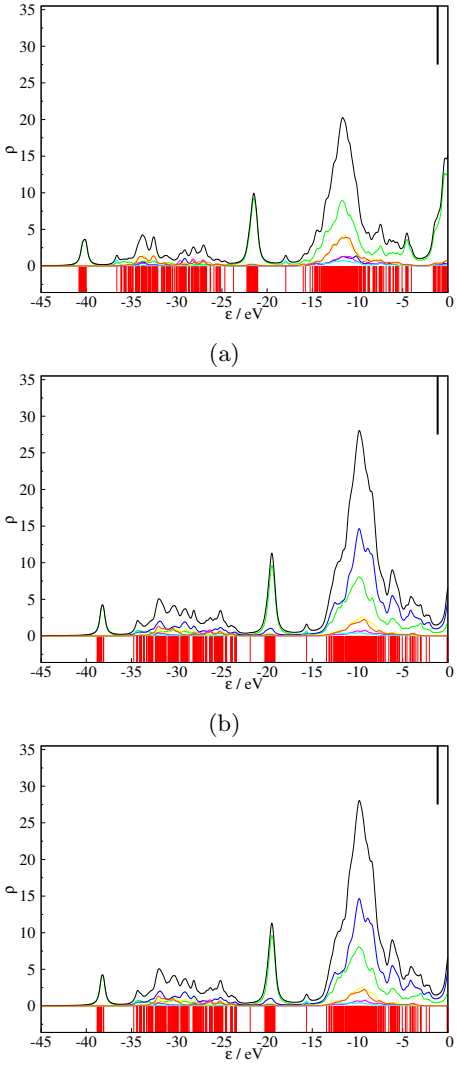


Figure 4.3: C-SPA/P-DOS analysis of the XZ:$Ba_{12}Ce_{22}O_{61}H_2$ fragments when hydrogen is embedded in the framework, XZ = CeCe (a), CeY (b), YY (c): orbital contribution of atomic sets included in the $XZBa_4O_{11}$ moiety to the MOs of the same moiety against energy values, ($\rho$ vs. $\varepsilon$). $Ba_4$ group, green line; X atom, blue line; Z atom, purple line; O4 atom, light blue line; $O_X$ moiety, red line; $O_Z$ moiety, yellow line; $XZBa_4O_{11}$ cluster: black line. The no influential H orbital contribution is not reported. The red bars individuate the eigenstates of the whole XZ:$Ba_{12}Ce_{22}O_{61}H_2$ fragments. The $\rho$ lines are obtained by a convolution of fixed-width Lorentzian curves centred on the energy bin used in the DOS analysis, being the height proportional to the weight of the AO set contribution in the bin. The black segment on the top individuates the HOMO-LUMO edge.

# Chapter 5

# $BaZrO_3$ Derivatives Ab Initio Results

The crystallographic phase of the $BaZrO_3$ is cubic over a wide range of temperatures, as observed in chapter 3, keeping the symmetries of the space group $Pm\bar{3}m$ even when a high percentage of yttrium is inserted into the structure [112]. Starting from the suggestions given by preceding results on Y:$BaCeO_3$ (see relative sections in chapter 4 and [84]), Y:$BaZrO_3$ perovskitic system have been investigated also in the aim to understand if the inferred yttrium local clustering is a characteristic feature of the yttrium as a substituent for the tetravalent cation in perovskite materials.

Preliminary calculations were made in order to optimize simulation parameters together with the basis sets for Zr and Y. In the following, results* will be grouped according to the size of the supercell used along the calculations, discussing also the corresponding protonated structures; the atom labelling used along the sections refers to the one depicted in Figure 3.10.

## 5.1 BZO and BZH Models

Undoped barium zirconate was initially studied by means of a $3 \times 3 \times 3$ and $4 \times 3 \times 3$ supercell of $BaZrO_3$, showed in Figure 3.8 and in Figure 3.9. Optimized positions of all the atoms of both supercells reproduced all the starting experimental values together with the geometrical features of the octahedral environment deserved to the $Pm\bar{3}m$ space group. Since PBC were applied and no constraints are imposed to the coordinates of all the atoms in the supercell, this result make us confident that the atomic arrangement de-

*Results presented in this chapter have been obtained by means of the computational resources of the "Centre d'Investigació en Nanociéncia i Nanotecnologia" (CIN2, CSIC-ICN, Barcelona – Spain) within the collaboration with the "Theory and Simulation Group", where I was kindly introduced by Prof. Pablo Ordejón, head of the group, during my visit in Barcelona.

scribe quite well the long range structure determined by neutron diffraction experiments without introducing any kind of geometrical distortions.

In order to model protonic defects into the bulk of the Y:$BaZrO_3$ crystalline structure, far from a doped site, the $4 \times 3 \times 3$ supercell system has been considered: one hydrogen atom has been added to this undoped optimized structure, bound to the O7 and according to the general geometrical prescription stated in subsection 3.1.2; then, this starting structure was left to relax. Relevant distances and angles of the proton environment resulted from the performed geometrical optimization are reported in BZH column of Table 5.1; in this, X=Z=Zr.

In the BZH model, the O4−H bond forms an angle of 23.4°with the plane containing the O7, O11 and O4 oxygen atoms; moreover, it lies in the plane individuated by the {O4, X, O5} set of atoms, containing also the O3, O6, O8, Z, O9 and O7 ones. Comparing the X−O and Z−O distances of the BZH model with those ones in the unprotonated reference structure (BZO), it can be readily seen that the distances involving the atoms in the plane are affected by the presence of the proton while the ones out of this plane result unchanged. So, also in this case as we found for the protonated $BaCeO_3$ systems (sections 4.1.2 and 4.2.2), we can call as *planar* the distortion induced by the proton; accordingly, distances lying in and out of the individuated plane will be referred as *planar* and *axial distances*, respectively. Despite the oxygen octahedron round the Z cation results distorted, its overall volume remains unchanged and no tilting is observed respect to the other unprotonated octahedra. Similarly, the Z−Ba distances are more affected than the X−Ba ones, however not changing the Ba first shell volume round the Z cation. These geometrical outcomes show how the modifications induced by the proton to the surrounding undoped environment are strictly local ones, essentially involving only the proton nearest neighbour atoms.

## 5.2 3x-YBZ Models

The dopant effect on the octahedral geometry was investigated by the 3x-YBZ model structures, built by using the geometry of the undoped $BaZrO_3$ model where one zirconium atom has been substituted by an yttrium one. After Y-doping, oxygen vacancies are created into the $BaZrO_3$ perovskite structure (see section 1.5); in the present model, all the oxygen sites are fully occupied, so describing a saturated oxygen vacancies doped compound.

Experimentally [109], only one value is reported for each of the Zr−O and Zr−Ba distances in undoped $BaZrO_3$, being these ones 2.10 and 3.63 Å respectively. Comparing these values with those ones reported for the present 3x-YBZ model (see Table 5.2), the octahedral cation first coordination shell results more expanded round the Y atom, slightly modifying that one of its Zr atoms first neighbours.

Table 5.1: Relevant distance and angle values for the unprotonated and protonated BZO and BZH systems.

| distances[a]/ Å | BZO[b] | BZH[b] | distances[c]/ Å | BZH |
|---|---|---|---|---|
| X−O1 | 2.08 | 2.08 | Z−O10 | 2.08 |
| X−O2 | 2.08 | 2.08 | Z−O11 | 2.08 |
| X−O3 | 2.08 | 1.98 | Z−O9 | 2.00 |
| X−O4 | 2.08 | 2.20 | Z−O4 | 2.17 |
| X−O5 | 2.08 | 2.12 | Z−O7 | 2.08 |
| X−O6 | 2.08 | 2.05 | Z−O8 | 2.07 |
| <X−O>[d] | 2.08 | 2.09 | <Z−O>[d] | 2.08 |
| X−Ba1 | 3.61 | 3.82 | Z−Ba1 | 3.77 |
| X−Ba2 | 3.61 | 3.60 | Z−Ba11 | 3.59 |
| X−Ba3 | 3.61 | 3.68 | Z−Ba3 | 3.67 |
| X−Ba4 | 3.61 | 3.57 | Z−Ba10 | 3.57 |
| X−Ba5 | 3.61 | 3.68 | Z−Ba5 | 3.67 |
| X−Ba6 | 3.61 | 3.57 | Z−Ba9 | 3.59 |
| X−Ba7 | 3.61 | 3.82 | Z−Ba7 | 3.77 |
| X−Ba8 | 3.61 | 3.61 | Z−Ba12 | 3.59 |
| <X−Ba>[d] | 3.61 | 3.67 | <X−Ba>[d] | 3.65 |
| angles[e]/ ° | BZO | BZH | angles[e]/ ° | BZH |
| H−O4−X | — | 80.5 | H−O7−Z | — |
| H−O4−X−O5 | — | 0.1 | H−O7−Z−O4 | — |
| H−O4−O2−O5 | — | 23.4 | H−O7−O11−O4 | — |

[a] X−O and X−Ba distance values between the X cation and its first neighbour oxygen and barium atoms; X=Z for the considered systems. For the atom labelling see Figure 3.10. [b] Results for $4 \times 3 \times 3$ supercells calculations: unprotonated (BZO) and protonated (BZH) $BaZrO_3$ model systems. [c] Z−O and Z−Ba distance values between the Z octahedral cation and its first neighbour oxygen and barium atoms: Z=Zr for the considered systems. For the atom labelling see Figure 3.10. The order of the labelling has been chosen following the correspondence occurring between the Z first neighbours and the X ones, by considering the plane individuated by the {Ba3, Ba5, Ba1, Ba7} set of atoms as a symmetry plane for the moiety shown in Figure 3.10. [d] Mean values of the corresponding atomic distances. [e] Relevant planar and dihedral angles formed by the hydrogen atom with its three nearest neighbours cation and oxygen atoms.

Taking as reference the Figure 3.10, the sets of oxygen atoms {O2, O4, O1, O3}, {O2, O5, O1, O6} and {O3, O5, O4, O6} single out three orthogonal planes containing the Y atom; in each of these planes, two couple of oxygen atoms, together with the Y one, individuate two incident lines, making two opposite-to-the-vertex pair of angles, that, in this case, are all

Table 5.2: Relevant distance values with their statistical weight characterizing the Y-doped octahedron environment of the unprotonated 3x-YBZ systems.

| 3x-YBZ[a] | X−O[b]/ Å | Z−O[b]/ Å |
|---|---|---|
| No vacancy | 6x2.17 | 1x2.01, 5x2.08 |
| Vacancy, -2 | 1x2.22, 4x2.16 | 1x2.10, 4x2.08 |
| Vacancy, -1 | 1x2.22, 4x2.16 | 1x2.09, 4x2.08 |
| Vacancy, 0 | 1x2.14, 4x2.16 | 1x2.01, 4x2.08 |
| Vacancy, +1 | 1x2.08, 4x2.17 | 1x1.93, 4x2.07 |
| Vacancy, +2 | 1x2.08, 4x2.17 | 1x1.93, 4x2.07 |
| 3x-YBZ | X−Ba[c]/ Å | Z−Ba[c]/ Å |
| No vacancy | 8x3.59 | 4x3.61, 4x3.60 |
| Vacancy, -2 | 4x3.57, 4x3.63 | 4x3.61, 4x3.63 |
| Vacancy, -1 | 4x3.57, 4x3.62 | 8x3.62 |
| Vacancy, 0 | 4x3.63, 4x3.64 | 4x3.67, 4x3.63 |
| Vacancy, +1 | 4x3.72, 4x3.65 | 4x3.76, 4x3.63 |
| Vacancy, +2 | 4x3.73, 4x3.65 | 4x3.75, 4x3.62 |

[a] 3x-YBZ systems with and without oxygen vacancy; each integer number refer to the charge value set for the corresponding oxygen deficient system. For reference, see Figure 3.10 where X=Y and Z=Zr for 3x-YBZ systems. [b] X−O and Z−O distance values between the X and Z octahedral cations and their first neighbour oxygen atoms.
[c] X−Ba and Z−Ba distance values between the X and Z atoms and their first neighbour barium atoms.

right ones (see Table 5.3). Furthermore, the doped octahedron does not show any tilt respect to the crystallographic axes. In this sense, the calculation show how the geometry of the oxygen octahedron coordinated by an Y atom is completely compatible with the $Pm\bar{3}m$ cubic structure, as reported by experimental data on Y:$BaZrO_3$[112].

The effect of one oxygen vacancy near a doped site was also taken into account. In order to describe this kind of system, the model structure has been created starting from the oxygen saturated 3x-YBZ system and removing one of the six[†] oxygen atoms surrounding the yttrium one; in particular, always taking Figure 3.10 as reference, the oxygen atom labelled as "4" has been removed. Several geometrical optimizations have been performed on

[†]Since the structure is cubic with the symmetries of $Pm\bar{3}m$ space group, all the oxygen sites are equivalent, irrespectively of the octahedral cation: neutron powder diffraction experiments are not able to distinguish between Y and Zr atom, being the experimental data refined on their relative abundance.

Table 5.3: Relevant angle values characterizing the Y-doped octahedron environment of the 3x-YBZ unprotonated systems.

| angles[a]/ ° | No vac.[b] | Vac.[c]-2 | Vac. -1 | Vac. 0 | Vac. 1 | Vac. 2 |
|---|---|---|---|---|---|---|
| O2−X−O3 | 90.0 | 87.9 | 87.9 | 95.0 | 100.7 | 100.7 |
| O2−X−O6 | 90.0 | 89.9 | 89.9 | 90.0 | 88.0 | 88.0 |
| O3−X−O6 | 90.0 | 87.9 | 88.0 | 95.0 | 100.7 | 100.7 |
| O11−Z−O9 | 89.7 | 91.0 | 91.2 | 95.5 | 100.6 | 100.6 |
| O11−Z−O8 | 90.0 | 89.9 | 90.0 | 89.5 | 88.0 | 88.0 |
| O9−Z−O8 | 90.0 | 91.0 | 91.2 | 95.5 | 100.6 | 100.6 |

[a] Angle values between the X and Z octahedral cations and their first neighbour oxygen atoms: X=Y and Z=Zr for 3x-YBZ systems; for the atom labelling, see Figure 3.10. [b] Results for 3x-YBZ system without any oxygen vacancies.
[c] Each "Vac. $n$" column refers to the oxygen deficient system whose charge value was set to $n$.

this system, differing for the net system charge chosen in the integer values range between -2 and +2 $|e|$. Corresponding results are reported in Tables 5.2 and 5.3.

In all the charged systems, the presence of one oxygen vacancy generates a bimodal distribution of the Y−O and Z−O distances, where Z is the other octahedral cation nearest to the vacancy, that, in these cases, is a Zr atom. The difference between the two mean values found for each of the Y−O and Y−Ba distances is lower for the neutral system while is more pronounced for high absolute charge values. Different trend is shown in the case of the Z cation. In the null charged system, the Z−O distance distribution is the same found for the saturated case; on the other hand, while a negative charge makes the distance values practically all the same, a positive charge enhances the difference between them. Similar trend is found for the Z−Ba distances, for which all the considerations done on the Y−O still hold.

Analysing the formation energy of the charged defect as described in Equation 2.33, the most stable system turns out to be the one with charge $+1|e|$. If we consider the formal charges assigned to each atom[‡], according to the 3x-YBZ geometry, the system owns a charge equal to $+1|e|$, as indeed it should be according to the results on the formation energy.

In all the optimized 3x-YBZ systems, both Y and Z cations lie on a line parallel to a crystallographic axis: the effect of the vacancy is to modify the positions of the nearest cations generating a displacement along one of the crystallographic axis, affecting mainly the distances between the octahedral cations and Ba atoms surrounding the vacancy. As a consequence, the Y−O3 and Z−O9 distances result strongly modified after a vacancy is created (see

[‡]For the Y:$BaZrO_3$ system, the formal charges are: Ba=$+2|e|$, Y=$+3|e|$, Zr=$+4|e|$ and O=$-2|e|$.

distances with statistical weight of 1 in Table 5.2), leaving almost unaltered all the others involving the remaining octahedral oxygens. Accordingly, the O−Y−O and O−Z−O right angles of the oxygen saturated structure result modified in such a way that the {O3, Y, Z, O9} set of atoms singles out a quaternary symmetry axis for all the 3x-YBZ systems (see Table 5.3).

## 5.3 4x-YBZ Models

**Unprotonated Systems.** In the aim to deeply investigate the local environment round a defect, the 4x-YBZ and 4x-2YBZ models have been built, extending the geometry of the 3x-YBZ preceding ones. Initially, undoped $BaZrO_3$ has been reproduced by means of an optimized $4\times3\times3$ supercell, as shown in Figure 3.9. The reliability of this starting model has been ensured by the ability to reproduce the geometrical features of the barium zirconate structure, result obtained without imposing any geometrical constraints and applying periodic boundary conditions.

The effect of zirconium substitution with an yttrium atom has been first analysed by means of the 4x-YBZ model, built using the undoped $BaZrO_3$ $4 \times 3 \times 3$ supercell where one zirconium atom has been substituted by an yttrium one. Since no oxygen vacancies have been considered in this first calculation, this system has been built in the aim to model the fully hydrated doped compound; moreover, comparisons with the corresponding 3x-YBZ model allow to investigate the effect of the cell size on the obtained results.

As shown in tables 5.4 and 5.5, the distance and angle values found are the same already individuated for the corresponding 3x-YBZ systems; moreover, using the labelling of Figure 3.10, the geometrical features of the planes individuated by the sets of atoms {O2, O4, O1, O3}, {O2, O5, O1, O6} and {O3, O5, O4, O6}, together with the opposite-to-the-vertex angles lying on them, still hold. Also the doped octahedron does not show any tilt, reproducing a doped environment compatible with the $Pm\bar{3}m$ cubic structure, as already observed for the smaller system (see section 5.2). This results show also that the oxygen saturated 3x-YBZ model is sized enough to catch the essential geometrical parameters for this kind of substitutional configuration.

Vacancy defect has been also considered with this model. Starting from the optimized oxygen saturated 4x-YBZ geometry, the oxygen labelled as "4" has been removed, building the model structure for the unhydrated compound. Since the vacancy is a charged defect for the Y:$BaZrO_3$perovskite structure (see Equation 1.2), geometrical optimizations performed on this systems differ for the net charge, chosen in the integer values range between -2 and +2 $|e|$. Relevant distances and angles obtained in the corresponding simulations are reported in tables 5.4 and 5.5.

As it was found for the 3x-YBZ systems with a vacancy, the Y−O and

Table 5.4: Relevant distance values with their statistical weight characterizing the Y-doped octahedron environment of the 4x-YBZ unprotonated systems.

| 4x-YBZ[a] | X−O[b]/ Å | Z−O[b]/ Å |
|---|---|---|
| No vacancy | 6x2.17 | 1x2.01, 5x2.08 |
| Vacancy, -2 | 1x2.14, 4x2.16 | 1x2.02, 4x2.07 |
| Vacancy, -1 | 1x2.20, 4x2.16 | 5x2.08 |
| Vacancy, 0 | 1x2.14, 4x2.16 | 1x2.02, 4x2.08 |
| Vacancy, +1 | 1x2.08, 4x2.17 | 1x1.94, 4x2.07 |
| Vacancy, +2 | 1x2.08, 4x2.17 | 1x1.94, 4x2.07 |
| 4x-YBZ | X−Ba[c]/ Å | Z−Ba[c]/ Å |
| No vacancy | 8x3.59 | 4x3.61, 4x3.60 |
| Vacancy, -2 | 4x3.63, 4x3.65 | 4x3.67, 4x3.63 |
| Vacancy, -1 | 4x3.58, 4x3.63 | 8x3.63 |
| Vacancy, 0 | 4x3.63, 4x3.64 | 4x3.67, 4x3.63 |
| Vacancy, +1 | 4x3.72, 4x3.64 | 4x3.76, 4x3.62 |
| Vacancy, +2 | 4x3.73, 4x3.64 | 4x3.76, 4x3.62 |

[a] 4x-YBZ systems with and without oxygen vacancy; each integer number refer to the charge value set for the corresponding oxygen deficient system. For reference, see Figure 3.10 where X=Y and Z=Zr for 4x-YBZ systems. [b] X−O and Z−O distance values between the X and Z octahedral cations and the corresponding first neighbour oxygen atoms. [c] X−Ba and Z−Ba distance values between the X and Z atoms and their corresponding first neighbour barium atoms.

Z−O distances are spread according to a bimodal distribution, where Z is the other octahedral cation nearest to the vacancy, that is a Zr atom. Also in these present cases, the differences between the two Y−O mean values are as more pronounced as higher the absolute charge values are; conversely, the difference between the Z−O mean distances is enhanced only by positive charge values of the whole system. The analysis of the formation energy for each charged defect indicates that, among those considered, the most stable system is the one with charge $+1|e|$, in agreement with the ideal stoichiometric charges (see footnote ‡ on page 91).

Finally, once again as in 3x-YBZ systems, in presence of one Y atom, the distance distributions and angle values between the oxygen atoms and their coordinating octahedral cation are distributed in such a way that the {O3, Y, Z, O9} set of atoms singles out a quaternary symmetry axis for all the 4x-YBZ systems. These results show that the 3x-YBZ models are sufficiently sized for describing a dopant geometrical configuration in which only

Table 5.5: Relevant angle values characterizing the Y-doped octahedron environment of the 4x-YBZ unprotonated systems.

| angles[a]/ ° | No vac.[b] | Vac.[c]-2 | Vac. -1 | Vac. 0 | Vac. 1 | Vac. 2 |
|---|---|---|---|---|---|---|
| O2−X−O3 | 90.0 | 95.5 | 91.8 | 95.0 | 101.3 | 101.3 |
| O2−X−O6 | 90.0 | 89.5 | 90.0 | 90.0 | 87.8 | 87.8 |
| O3−X−O6 | 90.0 | 95.5 | 91.8 | 95.0 | 101.3 | 101.3 |
| O11−Z−O9 | 89.7 | 95.5 | 92.6 | 95.5 | 101.0 | 101.1 |
| O11−Z−O8 | 90.0 | 89.5 | 89.9 | 89.5 | 87.9 | 87.9 |
| O9−Z−O8 | 90.0 | 95.5 | 92.5 | 95.5 | 101.0 | 101.1 |

[a] Angle values between the X and Z octahedral cations and their first neighbour oxygen atoms: X=Y and Z=Zr for 4x-YBZ systems; for the atom labelling, see Figure 3.10. [b] Results for 4x-YBZ system without any oxygen vacancies.
[c] Convention on "Vac. $n$" columns is the same as in Table 5.3.

one zirconium atom is substituted by an yttrium one, without introducing artificial numerical effects.

**Protonated Systems.** Structural rearrangements in hydrated Y:$BaZrO_3$ have also been studied by taking into account the presence of one proton in the dopant environment. In this aim, optimized structure of oxygen saturated 4x-YBZ model has been used as starting geometry to build the protonated model system. One proton has been added to the structure in such a way that it can be thought as bound to one of the oxygen atoms surrounding either an yttrium or a zirconium one. As previously observed (see footnote † on page 90 and discussion on unprotonated 4x-YBZ systems), according to the symmetries of $Pm\bar{3}m$ space group, in Y:$BaZrO_3$ all the oxygen sites are geometrically equivalent; nonetheless, the insertion of one yttrium atom into the crystalline matrix specializes some oxygen sites, at least because it makes different their coordination shells, and their features are as more enhanced as nearer the doped octahedron is. These features are highlighted in presence of a proton, that acts as a probe for their behaviour against a structural perturbation. In order to explore this kind of doped environment, and according to the size of our 4x-YBZ model, four oxygen distinct sites have been considered and corresponding four protonated 4x-YBZ model systems have been built: 4x-YBZ-H1, 4x-YBZ-H2, 4x-YBZ-H3 and 4x-YBZ-H4. In Figure 5.1, the four distinct oxygen sites are indicated by means of spheres with different colours and labelled according to the four models used to describe them. Therefore, 4x-YBZ-H1 model is intended to describe rearrangements of the structure when the proton lies in its stable position near one of the oxygen sites labelled as "1" and so on; analogously, the corresponding proton stable position will be called "H1".

Following the convention of Figure 3.10 with X=Y and Z=Zr, the first

two geometries of the 4x-YBZ-H1 and 4x-YBZ-H2 models have been obtained by placing the hydrogen atom near the O4 and O7 oxygen atom, respectively, and the whole systems was relaxed; relevant optimized distances and angles are reported in Table 5.6.

The description of the local environment of the proton in the 4x-YBZ-H3 and 4x-YBZ-H4 models concerns the portion of the $4 \times 3 \times 3$ supercell involving two zirconium atoms aligned with the yttrium one. Thus, in Figure 3.10, both X and Z octahedral cation are zirconium atoms and the O3 oxygen is bound to the yttrium atom not shown in the same figure. In these models, the corresponding starting geometries have been built by placing one hydrogen atom near the O4 and O7 oxygen atoms respectively; then, the structure was optimized. Geometrical parameters obtained with these two last models are shown in Table 5.7.

In all the protonated system considered, the proton lies in the plane individuated by the oxygen to which is bound, the nearest octahedral cation and the oxygen forming a hydrogen bond with it, as can be seen from the dihedral angle values showed in the corresponding tables. A common feature of all the protonated octahedra[§] is that the planar distances are distorted compared with the unprotonated case, being the longest ones those involving the octahedral cation and the two octahedral oxygens nearest to the proton; on the other hand, the axial distances keep their values practically unchanged, contributing, together with the planar distortion, in keeping almost unaltered the octahedral volume. An other common feature to all the 4x-YBZ-H$n$ systems is that the proton changes the distances of the octahedron in which resides without producing any tilt of it; conversely, the octahedron adjacent to the protonated one and containing the oxygen forming an hydrogen bond with the proton, undergoes a rotation round an axis perpendicular to the plane containing the proton and the cations of the two involved octahedra. The tilting of the Y coordinated octahedron is greater than in the case of the Zr one.

As observed above, the oxygen sites are not all strictly equivalent in Y:$BaZrO_3$ structure; despite this, in presence of a proton, the planar distances of the protonated octahedron are arranged in the same way, almost independently from the kind of octahedral cation. Let us consider the 4x-YBZ-H1 model. In this, the X−O planar distances of the protonated octahedron are arranged according to the relation X−O4>X−O5>X−O6>X−O3, being X−O4 the longest one. This behaviour is the same for all the remaining 4x-YBZ-H$n$ systems, making suitable correspondences among the oxygen atoms. The differences in the numerical values are due to the fact that the involved oxygen atoms do not belong to equivalent sites. In this

[§]Since the proton is bound to an oxygen O which always is a common vertex for two adjacent octahedra, each coordinated by a X and Z generic cation respectively, the X coordinated octahedron can be said *protonated* if the H−O−X angle is smaller than the H−O−Z one.

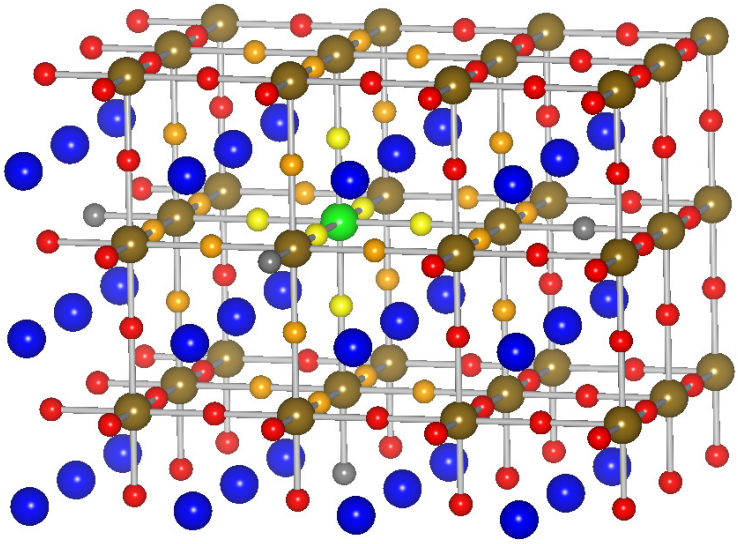

(a)

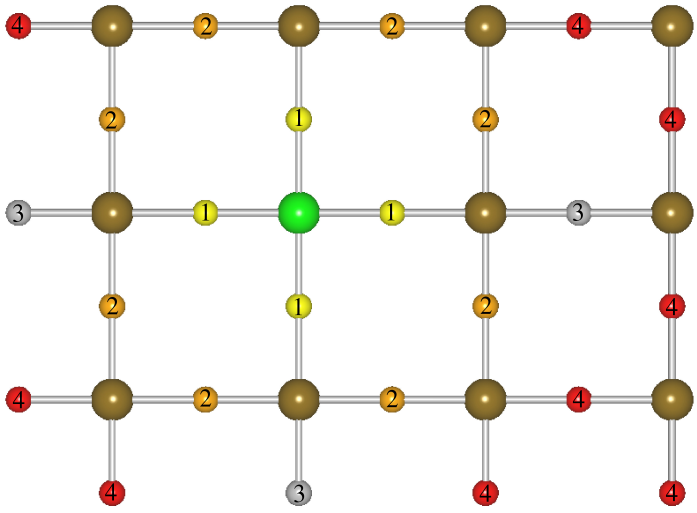


(b)

Figure 5.1: Positions of the oxygen distinct sites in 4x-YBZ models: blue, brown and green spheres represent the barium, zirconium and yttrium atoms, respectively; all the remaining spheres are oxygen atoms. Equivalent oxygen sites correspond to equally coloured spheres. The oxygen distinct sites have been numbered as in (b), where a particular section of the structure in (a) is shown.

Table 5.6: Relevant distance and angle values the Y-doped octahedron environment of the 4x-YBZ-H1 and 4x-YBZ-H2 protonated systems.

| distances[a]/ Å | 4x-YBZ-H1[b] | 4x-YBZ-H2[b] | distances[c]/ Å | 4x-YBZ-H1 | 4x-YBZ-H2 |
|---|---|---|---|---|---|
| X−O1 (1) | 2.16 | 2.17 | Z−O10 (2) | 2.08 | 2.08 |
| X−O2 (1) | 2.16 | 2.17 | Z−O11 (2) | 2.08 | 2.08 |
| X−O3 (1) | 2.10 | 2.21 | Z−O9 (3) | 2.01 | 2.04 |
| X−O4 (1) | 2.27 | 2.26 | Z−O4 (1) | 2.13 | 2.07 |
| X−O5 (1) | 2.24 | 2.18 | Z−O7 (2) | 2.08 | 2.24 |
| X−O6 (1) | 2.15 | 2.19 | Z−O8 (2) | 2.08 | 1.98 |
| <X−O>[d] | 2.18 | 2.20 | <Z−O>[d] | 2.08 | 2.08 |
| X−Ba1 | 3.82 | 3.61 | Z−Ba1 | 3.76 | 3.84 |
| X−Ba2 | 3.59 | 3.63 | Z−Ba11 | 3.58 | 3.68 |
| X−Ba3 | 3.65 | 3.63 | Z−Ba3 | 3.68 | 3.62 |
| X−Ba4 | 3.57 | 3.65 | Z−Ba10 | 3.59 | 3.57 |
| X−Ba5 | 3.65 | 3.63 | Z−Ba5 | 3.68 | 3.62 |
| X−Ba6 | 3.57 | 3.65 | Z−Ba9 | 3.59 | 3.58 |
| X−Ba7 | 3.81 | 3.61 | Z−Ba7 | 3.75 | 3.84 |
| X−Ba8 | 3.58 | 3.62 | Z−Ba12 | 3.58 | 3.68 |
| <X−Ba>[d] | 3.66 | 3.63 | <X−Ba>[d] | 3.65 | 3.68 |
| angles[e]/ ° | 4x-YBZ-H1 | 4x-YBZ-H2 | angles[e]/ ° | 4x-YBZ-H1 | 4x-YBZ-H2 |
| H−O4−X | 73.3 | — | H−O7−Z | — | 72.6 |
| H−O4−X−O5 | 0.37 | — | H−O7−Z−O4 | — | -0.2 |
| H−O4−O2−O5 | 16.0 | — | H−O7−O11−O4 | — | 17.2 |

[a] X−O and X−Ba distance values between the X cation and its first neighbours atoms; X=Y for the considered systems. The number in parenthesis next to each oxygen label is the label of the corresponding occupied oxygen site. For the atom and oxygen site labelling see Figures 3.10 and 5.1. [b] Results for the corresponding 4x-YBZ-H1 and 4x-YBZ-H2 calculations. [c] Z−O and Z−Ba distance values between the Z octahedral cation and its first neighbour oxygen and barium atoms: Z=Zr for the considered systems. The number in parenthesis next to each oxygen label is the label of the corresponding occupied oxygen site. For the atom and oxygen site labelling see Figures 3.10 and 5.1. The order of the labelling has been chosen as explained in note *c* of Table 5.1. [d] Mean values of the corresponding atomic distances. [e] Relevant planar and dihedral angles formed by the hydrogen atom with its three nearest neighbours cation and oxygen atoms.

Table 5.7: Relevant distance and angle values the Y-doped octahedron environment of the 4x-YBZ-H3 and 4x-YBZ-H4 protonated systems.

| distances[a]/ Å | 4x-YBZ-H3[b] | 4x-YBZ-H4[b] | distances[c]/ Å | 4x-YBZ-H3 | 4x-YBZ-H4 |
|---|---|---|---|---|---|
| X−O1 (2) | 2.08 | 2.09 | Z−O10 (4) | 2.08 | 2.08 |
| X−O2 (2) | 2.08 | 2.09 | Z−O11 (4) | 2.08 | 2.08 |
| X−O3 (1) | 1.94 | 2.02 | Z−O9 (3) | 1.99 | 2.03 |
| X−O4 (3) | 2.22 | 2.16 | Z−O4 (3) | 2.18 | 2.10 |
| X−O5 (2) | 2.13 | 2.09 | Z−O7 (4) | 2.09 | 2.22 |
| X−O6 (2) | 2.06 | 2.10 | Z−O8 (4) | 2.07 | 1.98 |
| <X−O>[d] | 2.09 | 2.09 | <Z−O>[d] | 2.08 | 2.08 |
| X−Ba1 | 3.82 | 3.62 | Z−Ba1 | 3.76 | 3.83 |
| X−Ba2 | 3.61 | 3.64 | Z−Ba11 | 3.59 | 3.69 |
| X−Ba3 | 3.69 | 3.64 | Z−Ba3 | 3.69 | 3.60 |
| X−Ba4 | 3.59 | 3.66 | Z−Ba10 | 3.59 | 3.58 |
| X−Ba5 | 3.69 | 3.61 | Z−Ba5 | 3.69 | 3.60 |
| X−Ba6 | 3.59 | 3.66 | Z−Ba9 | 3.59 | 3.58 |
| X−Ba7 | 3.82 | 3.62 | Z−Ba7 | 3.76 | 3.83 |
| X−Ba8 | 3.60 | 3.64 | Z−Ba12 | 3.59 | 3.70 |
| <X−Ba>[d] | 3.68 | 3.64 | <X−Ba>[d] | 3.66 | 3.68 |
| angles[e]/ ° | 4x-YBZ-H3 | 4x-YBZ-H4 | angles[e]/ ° | 4x-YBZ-H3 | 4x-YBZ-H4 |
| H−O4−X | 78.1 | — | H−O7−Z | — | 75.8 |
| H−O4−X−O5 | 0.1 | — | H−O7−Z−O4 | — | 0.1 |
| H−O4−O2−O5 | 20.7 | — | H−O7−O11−O4 | — | 19.6 |

[a] X−O and X−Ba distance values between the X cation and its first neighbours atoms; X=Zr for the considered systems. The number in parenthesis next to each oxygen label is the label of the corresponding occupied oxygen site. For the atom and oxygen site labelling see Figures 3.10 and 5.1. [b] Results for the corresponding 4x-YBZ-H3 and 4x-YBZ-H4 calculations. [c] Z−O and Z−Ba distance values between the Z octahedral cation and its first neighbour oxygen and barium atoms: Z=Zr for the considered systems. The number in parenthesis next to each oxygen label is the label of the corresponding occupied oxygen site. For the atom and oxygen site labelling see Figures 3.10 and 5.1. The order of the labelling has been chosen as explained in note *c* of Table 5.1. [d] Mean values of the corresponding atomic distances.
[e] Relevant planar and dihedral angles formed by the hydrogen atom with its three nearest neighbours.

way, the proton overlaps its ability to locally specialize the oxygen sites to their features due to the position they occupy in the structure. For this reason, the study of the unprotonated doped environment alone could not be sufficient to make predictions on its behaviour after proton defects are acquired by the structure.

The effect of this overlapping is better visualized if the energy differences among protonated systems are considered. In Figure 5.2, the energy of the 4x-YBZ-H4 system is taken as reference. The proton stablest position turns out to be near one of the oxygens surrounding the Y atom (O(1) sites); from these, the energy grows progressively as the proton jumps towards the O(2) and then to the O(3) site to finally reach the undoped zones (O(4) sites). In this pathway, the proton must overcome at least three energy barriers, one for each jump between two different oxygen sites; the number of barriers could become two if the O(1)→O(2)→O(4) path is followed but, actually they are much more if the jumps between equivalent sites are also taken into account. Looking at the Figure 5.1, it is clear that after substituting one zirconium atom with an yttrium one, the O(1), O(2) and O(3) oxygen sites are created besides the O(4) one already existing in the undoped $BaZrO_3$ structure, and they extend over a volume of about $3 \times 3 \times 3$ unit cells. Such volume is a sample of $BaZrO_3$ with about 4% of Y doping; this implies that, for higher yttrium percentages, the shell of O(1), O(2) and O(3) oxygen sites around an yttrium atom overlaps with others of the same kind, producing more than the four distinct oxygen sites found for the 4x-YBZ systems. Correspondingly, the number of different proton hopping barriers grows as more as higher is the yttrium content into the structure.

The relative energies of the 4x-YBZ-H$n$ systems give an idea on the stability of the proton position but nothing can be said about the height of each barrier the proton must overcome. Surely, the values must be higher than 0.04 eV and 0.17 eV, in order to have hopping events instead of simple diffusion between two H$n$ stable positions; moreover, if we take into account also the hopping events between equivalent sites, it is possible to estimate the role of entropy effects. Keeping in mind that the absolute energy values depend on the calculation method, the differences between the stabilization energies found for each of the here discussed systems are not enough alone to explain the activation energy of 0.43 eV, experimentally found for the overall process of protonic conduction [20]. A rough evaluation of other contributions can be done by considering further details of the protonated octahedron geometry.

The O−H bond distance is about 1.01 Å for all the here considered systems. Different behaviour is found for the planar and dihedral angle formed with the nearest neighbour atoms: the larger is the distance form the yttrium site, the larger is the corresponding value. The planar angle values range between 73.0 and 77.0°while the dihedral angles are in the 16÷20°range. Lower values correspond to stable sites that favour the intra-octahedral hopping

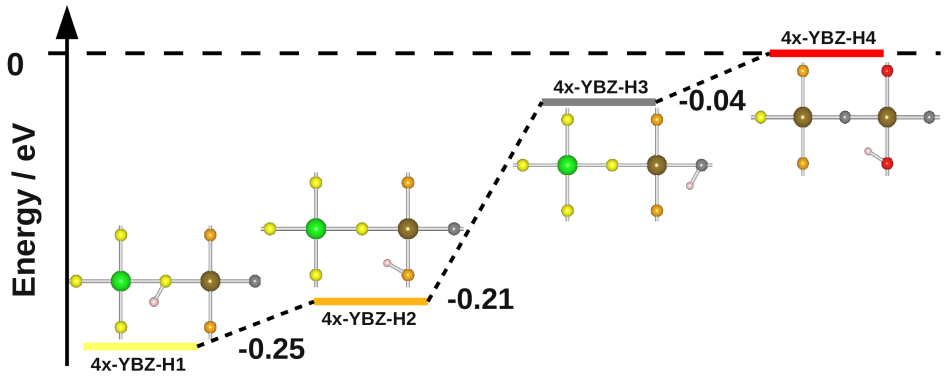


Figure 5.2: Energy diagram for 4x-YBZ-H$n$ systems. The energy of each system is referred to the one of the 4x-YBZ-H4 optimized structure. The insets show how the oxygen sites are arranged in the proton environment of the corresponding system; the colours used for the atomic positions follow the same convention of Figure 5.1.

within the same octahedron, and to higher (reorientation) barriers along that pathways leading to other external octahedral sites. If the energy barrier for the hopping event between two equivalent O(1) or O(2) oxygen sites is lower than the remaining ones, these sites constitute a trapping zone for the proton, being not able to go far from the yttrium and diffuse in the rest of the structure.

## 5.4 4x-2YBZ Models

**Unprotonated Systems.** Following the hints of the results obtained from the previous calculations on Y:$BaCeO_3$ (see chapter 4) and extending the 4x-YBZ models, the effects of zirconium substitution with yttrium atoms have been explored by the following 4x-2YBZ models. The geometry of these models have been built starting from a $4 \times 3 \times 3$ supercell of undoped $BaZrO_3$, substituting two first neighbour zirconium atoms with two yttrium ones.

Initially, no oxygen vacancy has been considered, in the aim to describe fully saturated systems. In order to investigate the effects of unbalanced charges that can be locally found in the doped octahedron environment [167], five geometrical optimizations have been performed on this systems, differing for the structure net charge chosen in the range of integer values between -2 and +2 $|e|$. In all the simulations, irrespective of the charge of the system, the Y$-$O distances found take all the same value. Taking as reference Figure 3.10, where X=Z=Y for all the 4x-2YBZ systems, we found

the following values: *i*) X−O3 and Z−O9, 2.16 Å; *ii*) X−O4 and Z−O4, 2.11 Å; *iii*) all the other X−O and Z−O distances relative to the remaining oxygen atoms used as reference, 2.17 Å; *iv*) all the X−Ba and Z−Ba distances, 3.59 Å. These results show how an excess or a defect of electronic charge does not affect the local geometrical features of the doped sites. Moreover, irrespective of the local excess or defect of charge, such yttrium configuration for zirconium substitution, that is a Y−O−Y local cluster, singles out a bimodal distance distribution for the Y−O distances, round the mean values of 2.11 and 2.17 Å respectively. Among the considered systems, according to the energy formation defect analysis as described in Equation 2.33, the most stable one is the system with charge -2$|e|$.

On the other hand, charge effects are prevailing when one oxygen vacancy is created by removing one of the oxygen atoms surrounding a doped octahedron. This has been investigated by performing structural relaxations on 4x-2YBZ models in which, as already done for the oxygen deficient 3x-YBZ and 4x-YBZ systems, the O4 oxygen atom has been removed from the structure, imposing to the systems the same charge values chosen for the oxygen saturated 4x-2YBZ systems just discussed; the relevant geometrical parameters are reported in Tables 5.8 and 5.9 as usual.

In all the 4x-2YBZ systems with one oxygen vacancy but that one with charge equal to -1, the spreading of the X−O and Z−O distances single out a bimodal distribution centred on 2.08 Å and 2.18 Å with statistical weight of 1/5 and 4/5 respectively; in both cases, among the considered atoms, the shorter distance is the one involving the oxygen atom farthest from the vacancy (i.e. O3 and O9). Similar consideration holds for the X−Ba and Z−Ba distances. From this results it turns out that, a charge of -1$|e|$ counterbalances the effect of the oxygen vacancy on the distances involving the octahedral cations. However, according the usual analysis on formation energy of charge defects, the most stable systems turns out to be the one with null charge. In all the analysed cases, the doped octahedra do not show any tilt with respect to the other undoped ones; in this way the {O3, X, Z, O9} aligned atoms individuate a four-fold axes of symmetry for the $Ba_{12}XO_5ZO_5$ moiety here considered, allowing it to be compatible with the experimental reported $Pm\bar{3}m$ cubic structure.

The discussed outcomes on unprotonated 4x-2YBZ models, are quite in agreement with the NPD data on Y:$BaZrO_3$, since, the distances and the found octahedra reciprocal orientation are in line with the features concerning the symmetry of the system; the presence of the X−O and Z−O shorter distance can be neglected in this comparison because this can disappear already at 77K (see chapter 6) and could be not resolved because of its small statistical weight. In this sense, these models describe quite well the averaged structure in experimental data. On the other hand, these outcomes need to be compared with local informations round dopant atoms (coming, for example from EXAFS experiments), that, to our knowledge, are still not

Table 5.8: Relevant distance values with their statistical weight characterizing the Y-doped octahedron environment of the 4x-2YBZ unprotonated systems.

| 4x-2YBZ[a] | X−O[b]/ Å | Z−O[b]/ Å |
|---|---|---|
| No vacancy | 1x2.11, 4x2.17, 1x2.16 | 1x2.11, 4x2.17, 1x2.16 |
| Vacancy, -2 | 1x2.08, 4x2.18 | 1x2.08, 4x2.18 |
| Vacancy, -1 | 1x2.14, 4x2.17 | 1x2.14, 4x2.17 |
| Vacancy, 0 | 1x2.08, 4x2.18 | 1x2.08, 4x2.18 |
| Vacancy, +1 | 1x2.08, 4x2.17 | 1x2.08, 4x2.17 |
| Vacancy, +2 | 1x2.08, 4x2.18 | 1x2.08, 4x2.18 |
| 4x-2YBZ | X−Ba[c]/ Å | Z−Ba[c]/ Å |
| No vacancy | 8x3.59 | 8x3.59 |
| Vacancy, -2 | 4x3.66, 4x3.73 | 4x3.73, 3x3.66 |
| Vacancy, -1 | 8x3.64 | 8x3.64 |
| Vacancy, 0 | 4x3.73, 4x3.64 | 4x3.72, 4x3.64 |
| Vacancy, +1 | 4x3.73, 4x3.64 | 4x3.73, 4x3.64 |
| Vacancy, +2 | 4x3.73, 4x3.65 | 4x3.73, 4x3.65 |

[a] 4x-2YBZ systems with and without oxygen vacancy; each integer number refer to the charge value set for the corresponding oxygen deficient system. The reference system, without any vacancies, has charge equal to zero and correspond to the null-charge 4x-2YBZ oxygen saturated model discussed in the present paragraph. For reference, see Figure 3.10 where X=Z=Y for these systems. [b] X−O and Z−O distance values between the X and Z octahedral cations and their corresponding first neighbour oxygen atoms. [c] X−Ba and Z−BA distance values between the X and Z atoms and their corresponding first neighbour barium atoms.

available; nonetheless, the 4x-2YBZ as the 4x-YBZ and 3x-YBZ models are a useful tool to make predictions on the proton environment, supporting the analysis of the classical dynamic simulations still performed on Y:$BaZrO_3$ perovskite system and presented in the next chapter 6.

Finally, a further oxygen saturated 4x-2YBZ model have been considered, in which two yttrium atoms substitute for two zirconium ones not belonging to adjacent octahedra (i.e. they are not first neighbours in their corresponding cation coordination shell), but they are aligned with a zirconium atom lying in-between them, forming a Y−O−Zr−O−Y configuration. This configuration can be visualized by considering the Figure 3.10, where X=Y, Z=Zr and the remaining not shown Y atom is bound to O9 in such a way that the {X, O4, Z, O9, Y} atoms are aligned. The geometrical optimization performed on this system yielded the following distance values: *i*) Y−O, 2x2.15, 4x2.17 Å; *ii*) Z−O, 2x2.02, 4x2.10 Å; *iii*) Y−Ba, 8x3.58; *iv*) Z−Ba, 8x3.60. Moreover, the Y and Z coordinated octahedra do not suffer

Table 5.9: Relevant angle values characterizing the Y-doped octahedron environment of the 4x-2YBZ unprotonated systems.

| angles[a]/ ° | No vac.[b] | Vac.[c]-2 | Vac. -1 | Vac. 0 | Vac. 1 | Vac. 2 |
|---|---|---|---|---|---|---|
| O2−X−O3 | 90.0 | 101.3 | 96.2 | 101.0 | 100.9 | 101.0 |
| O2−X−O6 | 90.0 | 87.8 | 89.3 | 87.9 | 88.0 | 87.9 |
| O3−X−O6 | 90.0 | 101.3 | 96.2 | 101.0 | 100.9 | 101.0 |
| O11−Z−O9 | 90.0 | 101.3 | 96.2 | 101.0 | 100.9 | 101.0 |
| O11−Z−O8 | 90.0 | 87.8 | 89.3 | 87.9 | 88.0 | 87.9 |
| O9−Z−O8 | 90.0 | 101.3 | 96.2 | 101.0 | 100.9 | 101.0 |

[a] Angle values between the X and Z octahedral cations and their first neighbour oxygen atoms: X=Z=Y for 4x-2YBZ systems; for the atom labelling, see Figure 3.10. [b] Results for 4x-2YBZ system without any oxygen vacancies.
[c] Convention on "Vac. $n$" columns is the same as in Table 5.3.

of any tilt with respect to the remaining undoped ones. These values are practically the same as those found for the oxygen saturated 3x-YBZ and 4x-YBZ models; thus, this last model show as the peculiar Y−O distance distribution of the doubly substituted 4x-2YBZ systems is lost when two yttrium atoms do not belong to the same first neighbour coordination shell of the octahedral cation. Because of the very little difference between the two Y−O mean distances, this configuration could be inferred only as an extrapolation if the two different Z−O distances are experimentally resolved. Anyway, since this system is intended to model a hydrated compound, the structural disorder due to the presence of protons and the thermal disorder would make hard to recognize this kind of configuration. Finally, it is here to be said, that this last geometrical configuration results more stable than the corresponding 4x-2YBZ, being their energy difference of 1.76 eV, leading one to choose the stablest geometry to describe the doped system. Nonetheless, the structure of the bulk as well as the grain kind (size, shape, composition and so on) strongly depend on the synthesis method and the details of the reactions that from the starting nanoclusters lead to the formation of the whole material [112, 127, 128, 168, 169].

**Protonated Systems.** The double zirconium substitution in 4x-2YBZ structures, although observe the symmetry of the $Pm\bar{3}m$ space group, specialize oxygen atomic positions present in the surrounding environment, in a more incisive way than a single substitution can do (see section 5.3). As a matter of fact, the oxygen sites keep all the geometrical equivalence but their features will be disclosed by their behaviour against a structural perturbation.

According to the configuration of the oxygen saturated 4x-2YBZ model, eight distinct oxygen sites have been individuated (see Figure 5.3) and cor-

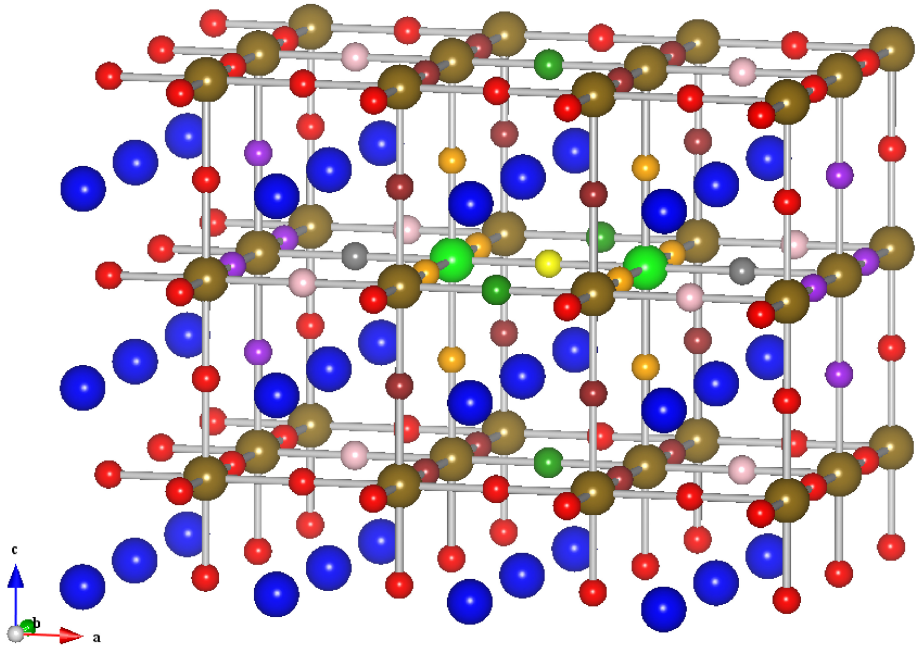


Figure 5.3: Positions of the oxygen distinct sites in 4x-2YBZ models: blue, brown and green spheres represent the barium, zirconium and yttrium atoms, respectively; all the remaining spheres are oxygen atoms. Equally coloured spheres correspond to equivalent oxygen sites. The oxygen distinct sites have been numbered as in Figures 5.4, 5.5 and 5.6.

responding eight protonated 4x-2YBZ model systems have been built. Following the convention adopted in section 5.3, the name of the models will be 4x-2YBZ-H$n$, where $n$ is an integer corresponding to the label of the oxygen site as depicted in Figures 5.4, 5.5 and 5.6, and H$n$ will be called the proton stable position near the O($n$) oxygen site.

The starting geometry for all the 4x-2YBZ-H$n$ protonated system is the one of the oxygen saturated null charged 4x-2YBZ structure, where one proton has been added near the O($n$) oxygen site, according to the general prescription described in subsection 3.1.2. Geometrical optimizations have been performed on these systems and the corresponding results are reported in Tables 5.10, 5.11, 5.12, 5.13.

In all the protonated systems, the proton lies in the plane individuated by the oxygen to which is bound, the nearest octahedral cation and the oxygen forming an hydrogen bond with it (see the dihedral angle values showed in the corresponding tables). Irrespective of the oxygen site near which the proton resides, the planar distances result distorted compared to the unprotonated case, and the longest are those involving the proton with the octahedral cation and the two nearest oxygen atoms. The axial

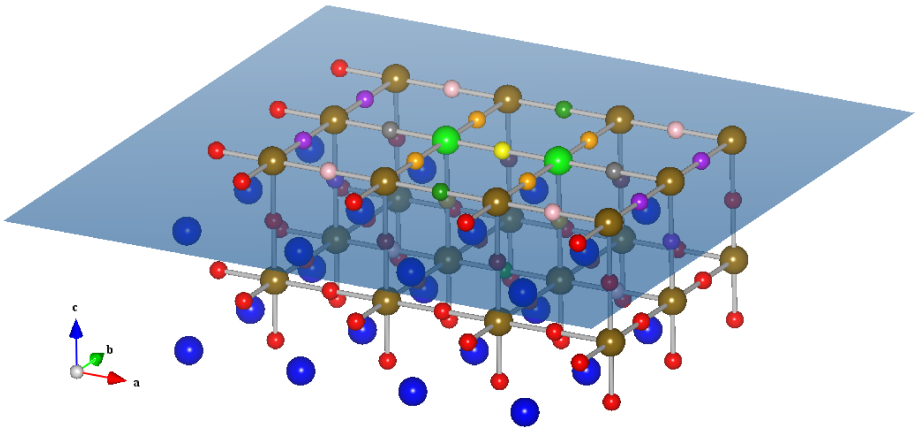


(a)

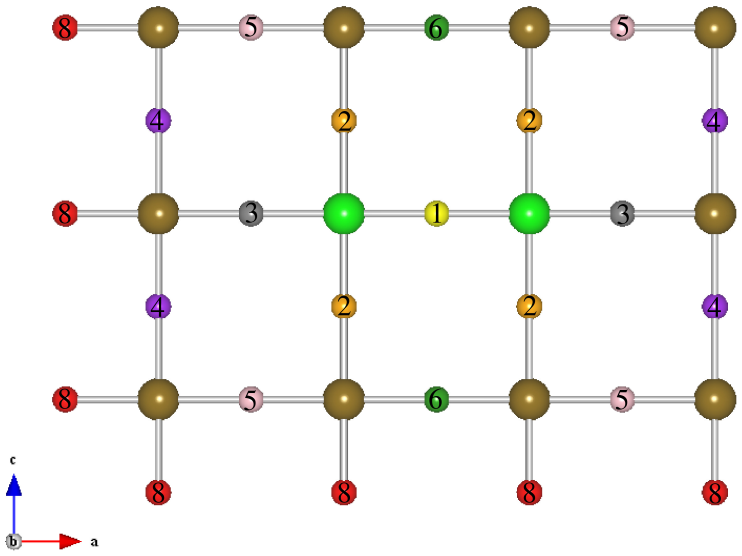


(b)

Figure 5.4: (a) Particular atomic plane of the 4x-2YBZ model geometry. (b) Numbering of the oxygen distinct sites contained in the atomic plane shown in (a). The colour legend is the same used as in Figure 5.3.

distances result unperturbed, maintaining unaltered the octahedral volume. In any of the considered cases, no tilting is observed for the octahedron containing the proton; conversely, the octahedron adjacent to the protonated one and containing the oxygen forming an hydrogen bond with the proton, rotates round an axis perpendicular to the plane containing the proton and the cations of the two involved octahedra. The tilting observed for the Y coordinated octahedra is greater than those for the Zr one. Finally, it must

be noted that in 4x-2YBZ-H8 system, the distances involving the octahedral atoms near the proton site are practically the same ones obtained with the undoped BZH model, showing that the O(8) oxygen site is equivalent to oxygens' one in the undoped BZH model.

Although the presence of yttrium atoms in the structure differentiate the oxygen sites, the planar distances perturbed by the proton are arranged in the same way almost independently from the kind of octahedral cation and from the kind of oxygen site. For example, the X−O planar distances of the 4x-2YBZ-H1 system are arranged in the order X−O4>X−O5>X−O6> >X−O3, with X−O4 the longest one; the same holds for all the remaining 4x-2YBZ-H$n$ systems, making the suitable correspondences among the oxygen atoms. Differences in numerical values reflect differences among those sites occupied by the protonated oxygen. The protonic perturbation is thus mixed with the features owned by each oxygen site due to the position they occupy in the structure. This mixing can be neglected only if a rough and not detailed analysis of the general features of the structure is required.

The features of each oxygen site can be also visualized by considering the diagram of the relative energies of the 4x-2YBZ-H$n$ models, shown in Figure 5.7. In this figure, the energy of each system, so each stable proton site, is represented by a bar coloured according to the convention used in Figures 5.4, 5.5 and 5.6, for labelling the oxygen sites. Each dashed line represents the intraoctahedral transfer pathway between two corresponding connected stable sites; the proton can go back and forth along the same path, overcoming, in general, energy barriers with different values (the energy landscape could not be symmetric along the hopping path). Furthermore, the number (multiplicity) of pathways connecting two particular stable sites depends on the local geometry of the involved sites; at the same time, the number of equivalent sites (with the same energy) reachable from a particular H$n$ stable position, is different for each of the considered cases. These are the configuration entropy contributions to the proton residence time on a particular site. So, for example, while eight O(2) sites are accessible from the O(1) one, for each O(2) site only one pathway is available for the O(2)→O(1) jump: despite the energies of both sites have almost the same value, it is more likely that the proton will spend more time near the oxygen occupying the O(2) position in the structure.

Giving a survey on the energy diagram, the stable proton sites can be grouped into three sets according to the differences between their energies. In this way, {H1, H2}, {H3, H4, H5, H6} and {H7, H8} sets of stable sites are individuated, being roughly 0.78, 0.56 and 0.14 eV the energy mean values within the same set, respectively. Let us call H(I), H(II) and H(III) the three groups of stable sites, in the same order they have been shown; according to the energy diagram in Figure 5.7, the relevant number of pathways connecting the three groups are: *i*) H(I)→H(II), 6; *ii*) H(II)→H(I), 9; *iii*) H(II)→H(III), 13; *iv*) H(III)→H(II), 10. Since the number of pathways

to go from a group to another is nearly the same to go back, the energy differences between stable sites play a major role in the proton diffusion with respect to one played by available pathways to go far from the oxygen shell round the yttrium atoms. It is here to be recalled that, besides the transfer pathways showed in the energy diagram of Figure 5.7, hopping events between two equivalent sites, whereas they are allowed[¶], increase proton residence time onto the same site, preventing it from escaping and diffusing towards other different oxygen sites. Therefore, the geometry of H(I) and H(II) groups of stable sites appear to act as a trap for the proton, producing one of the main contribution to the activation energy for the overall protonic conduction process across the material. Further details on this point will be inspected in the next chapter.

[¶]Since only intra-octahedral transfers are being considered, some stable sites do not have their equivalent one in their first coordination shell. It happens for H1, H3, H5 and H6 stable sites: one proton, for example, in H1 position cannot jump to a nearby H1 site since there are no intra-octahedral jumps that connect two H1 distinct sites.

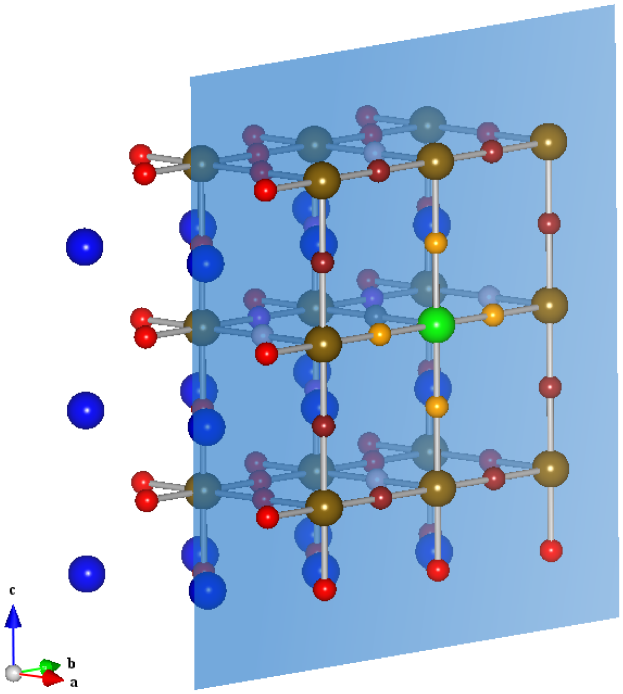


(a)

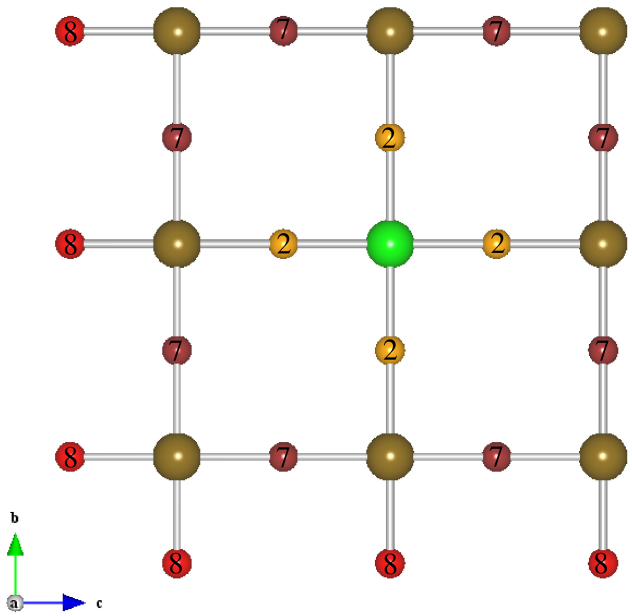


(b)

Figure 5.5: (a) Particular atomic plane of the 4x-2YBZ model geometry. (b) Numbering of the oxygen distinct sites contained in the atomic plane shown in (a). The colour legend is the same used as in Figure 5.3.

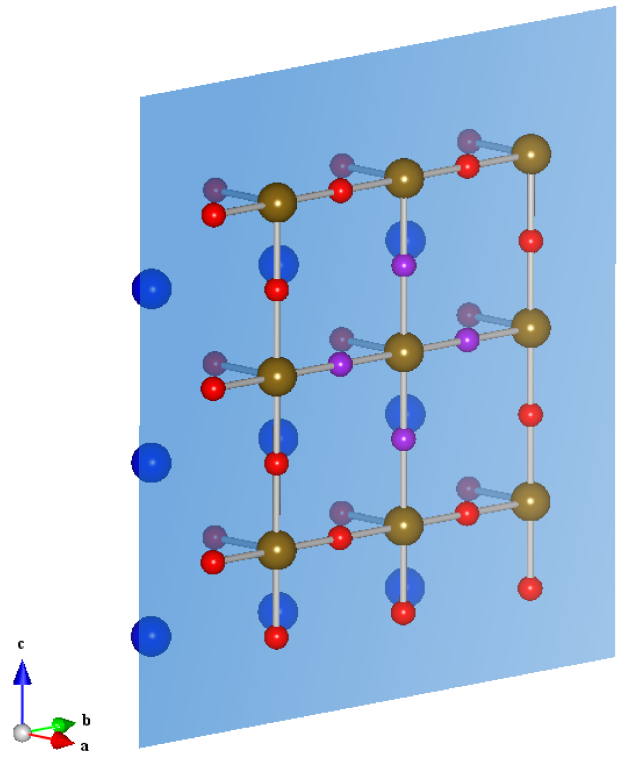


(a)

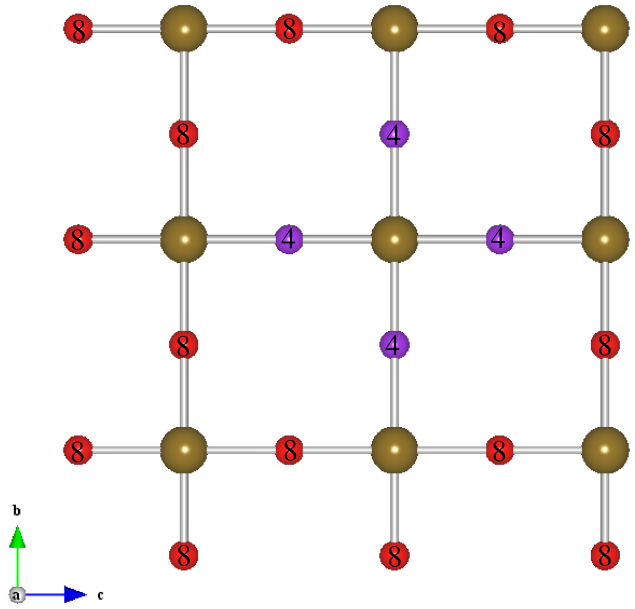


(b)

Figure 5.6: (a) Particular atomic plane of the 4x-2YBZ model geometry. (b) Numbering of the oxygen distinct sites contained in the atomic plane shown in (a). The colour legend is the same used as in Figure 5.3.

Table 5.10: Relevant distance and angle values the Y-doped octahedron environment of the 4x-2YBZ-H1 and 4x-2YBZ-H2 protonated systems.

| distances[a]/ Å | 4x-2YBZ-H1[b] | 4x-2YBZ-H2[b] | distances[c]/ Å | 4x-2YBZ-H1 | 4x-2YBZ-H2 |
|---|---|---|---|---|---|
| X−O1 (2) | 2.17 | 2.17 | Z−O10 (2) | 2.17 | 2.17 |
| X−O2 (2) | 2.17 | 2.17 | Z−O11 (2) | 2.17 | 2.17 |
| X−O3 (3) | 2.11 | 2.22 | Z−O9 (3) | 2.11 | 2.16 |
| X−O4 (1) | 2.23 | 2.21 | Z−O4 (1) | 2.23 | 2.21 |
| X−O5 (2) | 2.21 | 2.19 | Z−O7 (2) | 2.21 | 2.30 |
| X−O6 (2) | 2.17 | 2.21 | Z−O8 (2) | 2.17 | 2.10 |
| <X−O>[d] | 2.18 | 2.20 | <Z−O>[d] | 2.18 | 2.19 |
| X−Ba1 | 3.78 | 3.63 | Z−Ba1 | 3.77 | 3.83 |
| X−Ba2 | 3.57 | 3.64 | Z−Ba11 | 3.57 | 3.68 |
| X−Ba3 | 3.70 | 3.65 | Z−Ba3 | 3.68 | 3.60 |
| X−Ba4 | 3.57 | 3.66 | Z−Ba10 | 3.58 | 3.57 |
| X−Ba5 | 3.69 | 3.65 | Z−Ba5 | 3.68 | 3.60 |
| X−Ba6 | 3.57 | 3.67 | Z−Ba9 | 3.58 | 3.57 |
| X−Ba7 | 3.79 | 3.63 | Z−Ba7 | 3.77 | 3.83 |
| X−Ba8 | 3.57 | 3.64 | Z−Ba12 | 3.57 | 3.68 |
| <X−Ba>[d] | 3.66 | 3.65 | <X−Ba>[d] | 3.65 | 3.67 |
| angles[e]/ ° | 4x-2YBZ-H1 | 4x-2YBZ-H2 | angles[e]/ ° | 4x-2YBZ-H1 | 4x-2YBZ-H2 |
| H−O4−X | 83.8 | — | H−O7−Z | — | 68.2 |
| H−O4−X−O5 | 0.3 | — | H−O7−Z−O4 | — | 0.1 |
| H−O4−O2−O5 | 25.7 | — | H−O7−O11−O4 | — | 10.7 |

[a] X−O and X−Ba distance values between the X cation and its first neighbours atoms; X=Y for the considered systems. The number in parenthesis next to each oxygen label is the label of the corresponding occupied oxygen site. For the atom and oxygen site labelling see Figures 3.10 and 5.4.
[b] Results for the corresponding 4x-2YBZ-H1 and 4x-2YBZ-H2 calculations.
[c] Z−O and Z−Ba distance values between the Z octahedral cation and its first neighbour oxygen and barium atoms: Z=Y for the considered systems. The number in parenthesis next to each oxygen label is the label of the corresponding occupied oxygen site. For the atom and oxygen site labelling see Figures 3.10 and 5.4. The order of the labelling has been chosen as explained in note *c* of Table 5.1.
[d] Mean values of the corresponding atomic distances. [e] Relevant planar and dihedral angles formed by the hydrogen atom with its three nearest neighbours cation and oxygen atoms.

Table 5.11: Relevant distance and angle values the Y-doped octahedron environment of the 4x-2YBZ-H3 and 4x-YBZ-H4 protonated systems.

| distances[a]/ Å | 4x-2YBZ-H3[b] | 4x-2YBZ-H4[b] | distances[c]/ Å | 4x-2YBZ-H3 | 4x-2YBZ-H4 |
|---|---|---|---|---|---|
| X−O1 (2) | 2.17 | 2.17 | Z−O10 (4) | 2.08 | 2.08 |
| X−O2 (2) | 2.17 | 2.17 | Z−O11 (4) | 2.08 | 2.08 |
| X−O3 (1) | 2.07 | 2.15 | Z−O9 (8) | 2.00 | 2.03 |
| X−O4 (3) | 2.28 | 2.27 | Z−O4 (3) | 2.14 | 2.03 |
| X−O5 (2) | 2.25 | 2.19 | Z−O7 (4) | 2.08 | 2.25 |
| X−O6 (2) | 2.17 | 2.20 | Z−O8 (4) | 2.08 | 1.99 |
| <X−O>[d] | 2.18 | 2.19 | <Z−O>[d] | 2.08 | 2.08 |
| X−Ba1 | 3.84 | 3.61 | Z−Ba1 | 3.74 | 3.84 |
| X−Ba2 | 3.59 | 3.65 | Z−Ba11 | 3.58 | 3.68 |
| X−Ba3 | 3.68 | 3.63 | Z−Ba3 | 3.68 | 3.62 |
| X−Ba4 | 3.58 | 3.66 | Z−Ba10 | 3.59 | 3.57 |
| X−Ba5 | 3.68 | 3.63 | Z−Ba5 | 3.68 | 3.62 |
| X−Ba6 | 3.58 | 3.66 | Z−Ba9 | 3.58 | 3.58 |
| X−Ba7 | 3.84 | 3.61 | Z−Ba7 | 3.74 | 3.84 |
| X−Ba8 | 3.59 | 3.65 | Z−Ba12 | 3.58 | 3.68 |
| <X−Ba>[d] | 3.67 | 3.64 | <X−Ba>[d] | 3.65 | 3.69 |
| angles[e]/ ° | 4x-2YBZ-H3 | 4x-2YBZ-H4 | angles[e]/ ° | 4x-2YBZ-H3 | 4x-2YBZ-H4 |
| H−O4−X | 72.9 | — | H−O7−Z | — | 71.5 |
| H−O4−X−O5 | 0.1 | — | H−O7−Z−O4 | — | 0.1 |
| H−O4−O2−O5 | 14.5 | — | H−O7−O11−O4 | — | 16.1 |

[a] X−O and X−Ba distance values between the X cation and its first neighbours atoms; X=Y for the considered systems. The number in parenthesis next to each oxygen label is the label of the corresponding occupied oxygen site. For the atom and oxygen site labelling see Figures 3.10 and 5.4. [b] Results for the corresponding 4x-2YBZ-H3 and 4x-2YBZ-H4 calculations. [c] Z−O and Z−Ba distance values between the Z octahedral cation and its first neighbour oxygen and barium atoms: Z=Zr for the considered systems. The number in parenthesis next to each oxygen label is the label of the corresponding occupied oxygen site. For the atom and oxygen site labelling see Figures 3.10 and 5.4. The order of the labelling has been chosen as explained in note *c* of Table 5.1.
[d] Mean values of the corresponding atomic distances.
[e] Relevant planar and dihedral angles formed by the hydrogen atom with its three nearest neighbours cation and oxygen atoms.

Table 5.12: Relevant distance and angle values the Y-doped octahedron environment of the 4x-2YBZ-H5 and 4x-2YBZ-H6 protonated systems.

| distances[a]/ Å | 4x-2YBZ-H5[b] | 4x-2YBZ-H6[b] | distances[c]/ Å | 4x-2YBZ-H5 | 4x-2YBZ-H6 |
|---|---|---|---|---|---|
| X−O1 | (7) 2.08 | (2) 2.17 | Z−O10 | (7) 2.08 | (7) 2.09 |
| X−O2 | (7) 2.08 | (2) 2.17 | Z−O11 | (7) 2.08 | (7) 2.09 |
| X−O3 | (6) 2.00 | (2) 2.23 | Z−O9 | (8) 2.02 | (8) 2.06 |
| X−O4 | (5) 2.24 | (2) 2.24 | Z−O4 | (5) 2.15 | (2) 2.04 |
| X−O5 | (2) 2.08 | (1) 2.14 | Z−O7 | (4) 2.08 | (6) 2.21 |
| X−O6 | (8) 2.04 | (3) 2.21 | Z−O8 | (8) 2.08 | (5) 2.00 |
| <X−O>[d] | 2.09 | | <Z−O>[d] | 2.08 | |
| X−Ba1 | 3.83 | 3.62 | Z−Ba1 | 3.75 | 3.81 |
| X−Ba2 | 3.63 | 3.64 | Z−Ba11 | 3.59 | 3.68 |
| X−Ba3 | 3.67 | 3.63 | Z−Ba3 | 3.67 | 3.61 |
| X−Ba4 | 3.56 | 3.65 | Z−Ba10 | 3.58 | 3.57 |
| X−Ba5 | 3.67 | 3.64 | Z−Ba5 | 3.67 | 3.61 |
| X−Ba6 | 3.57 | 3.65 | Z−Ba9 | 3.59 | 3.57 |
| X−Ba7 | 3.83 | 3.62 | Z−Ba7 | 3.75 | 3.81 |
| X−Ba8 | 3.63 | 3.64 | Z−Ba12 | 3.59 | 3.68 |
| <X−Ba>[d] | 3.67 | 3.64 | <X−Ba>[d] | 3.65 | 3.67 |
| angles[e]/ ° | 4x-2YBZ-H5 | 4x-2YBZ-H6 | angles[e]/ ° | 4x-2YBZ-H5 | 4x-2YBZ-H6 |
| H−O4−X | 73.0 | — | H−O7−Z | — | 89.2 |
| H−O4−X−O5 | 0.1 | — | H−O7−Z−O4 | — | 0.0 |
| H−O4−O2−O5 | 16.9 | — | H−O7−O11−O4 | — | 25.7 |

[a] X−O and X−Ba distance values between the X cation and its first neighbours atoms; X=Zr for the 4x-2YBZ-H5 system while X=Y for the 4x-2YBZ-H6 one. For the atom labelling see Figure 3.10. [b] Results for the corresponding 4x-2YBZ-H5 and 4x-2YBZ-H6 calculations. The number in parenthesis next to each distance value is the label of the corresponding occupied oxygen site. For the oxygen site labelling see Figures 5.4, 5.5 and 5.6. [c] Z−O and Z−Ba distance values between the Z octahedral cation and its first neighbour oxygen and barium atoms: Z=Zr for the considered systems. For the atom labelling see Figure 3.10. The order of the labelling has been chosen as explained in note *c* of Table 5.1. [d] Mean values of the corresponding atomic distances. [e] Relevant planar and dihedral angles formed by the hydrogen atom with its three nearest neighbours cation and oxygen atoms.

Table 5.13: Relevant distance and angle values the Y-doped octahedron environment of the 4x-2YBZ-H7 and 4x-2YBZ-H8 protonated systems.

| distances[a]/ Å | 4x-2YBZ-H7[b] | 4x-2YBZ-H8[b] | distances[c]/ Å | 4x-2YBZ-H7 | 4x-2YBZ-H8 |
|---|---|---|---|---|---|
| X−O1 | (1) 2.11 | (8) 2.08 | Z−O10 | (6) 2.08 | (8) 2.08 |
| X−O2 | (3) 2.16 | (8) 2.07 | Z−O11 | (5) 2.08 | (5) 2.07 |
| X−O3 | (2) 2.21 | (8) 1.98 | Z−O9 | (8) 2.04 | (8) 2.00 |
| X−O4 | (2) 2.26 | (8) 2.20 | Z−O4 | (2) 2.07 | (8) 2.17 |
| X−O5 | (2) 2.18 | (8) 2.11 | Z−O7 | (7) 2.23 | (4) 2.07 |
| X−O6 | (2) 2.20 | (8) 2.05 | Z−O8 | (7) 1.99 | (8) 2.07 |
| <X−O>[d] | 2.19 | 2.08 | <Z−O>[d] | 2.08 | 2.08 |
| X−Ba1 | 3.61 | 3.82 | Z−Ba1 | 3.84 | 3.76 |
| X−Ba2 | 3.62 | 3.61 | Z−Ba11 | 3.67 | 3.61 |
| X−Ba3 | 3.63 | 3.67 | Z−Ba3 | 3.63 | 3.67 |
| X−Ba4 | 3.65 | 3.57 | Z−Ba10 | 3.57 | 3.59 |
| X−Ba5 | 3.64 | 3.68 | Z−Ba5 | 3.64 | 3.67 |
| X−Ba6 | 3.64 | 3.57 | Z−Ba9 | 3.56 | 3.59 |
| X−Ba7 | 3.60 | 3.83 | Z−Ba7 | 3.83 | 3.78 |
| X−Ba8 | 3.63 | 3.61 | Z−Ba12 | 3.68 | 3.60 |
| <X−Ba>[d] | 3.63 | 3.67 | <X−Ba>[d] | 3.68 | 3.66 |
| angles[e]/ ° | 4x-2YBZ-H7 | 4x-2YBZ-H8 | angles[e]/ ° | 4x-2YBZ-H7 | 4x-2YBZ-H8 |
| H−O4−X | — | 80.6 | H−O7−Z | 73.4 | — |
| H−O4−X−O5 | — | 0.3 | H−O7−Z−O4 | 0.5 | — |
| H−O4−O2−O5 | — | 23.9 | H−O7−O11−O4 | 17.3 | — |

[a] X−O and X−Ba distance values between the X cation and its first neighbours atoms; X=Y for the 4x-2YBZ-H7 system while X=Zr for the 4x-2YBZ-H8 one. For the atom labelling see Figure 3.10. [b] Results for the corresponding 4x-2YBZ-H7 and 4x-2YBZ-H8 calculations. The number in parenthesis next to each distance value is the label of the corresponding occupied oxygen site. For the oxygen site labelling see Figures 5.4, 5.5 and 5.6. [c] Z−O and Z−Ba distance values between the Z octahedral cation and its first neighbour oxygen and barium atoms: Z=Zr for the considered systems. For the atom labelling see Figure 3.10. The order of the labelling has been chosen as explained in note *c* of Table 5.1. [d] Mean values of the corresponding atomic distances. [e] Relevant planar and dihedral angles formed by the hydrogen atom with its three nearest neighbours cation and oxygen atoms.

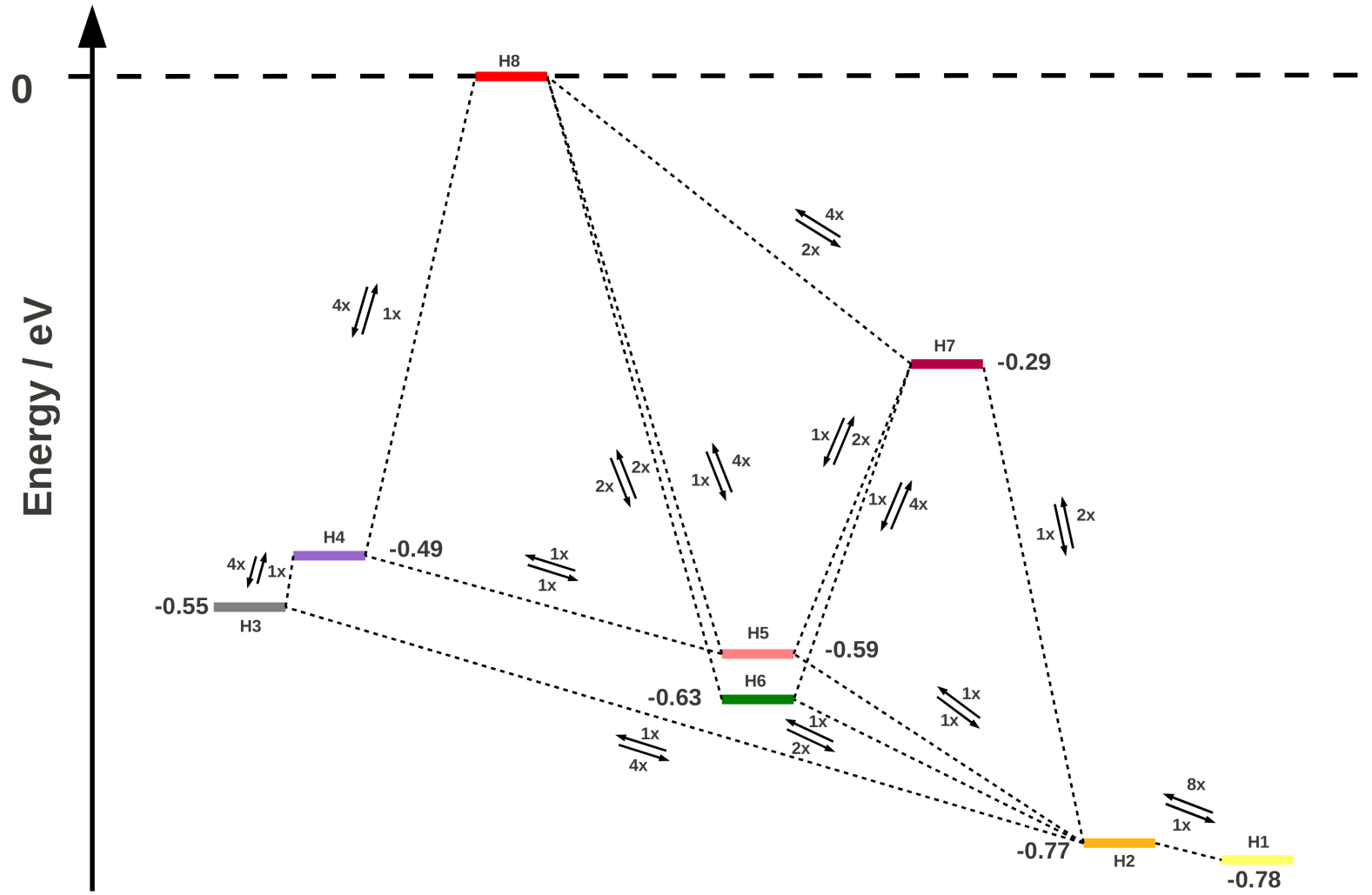




Figure 5.7: Energy diagram for 4x-2YBZ-H$n$ systems. The reference energy value is the one of the 4x-2YBZ-H8 optimized structure. Each dashed line represents a transfer pathway: starting from a given site H$n$, the proton can move to all sites connected to H$n$ by a dashed line. The couple of arrows next to each dashed line represents the two ways that the proton can follow along the transfer path. The symbol "$p$x" next to an arrow represents the multiplicity of the specific transfer way: following the arrow direction along the corresponding transfer path, there are $p$ equivalent pathways that lead from one site to the other.

# Chapter 6

# $BaZrO_3$ Derivatives Molecular Dynamics Simulations Results

Ab initio simulations performed on model systems for Y:$BaZrO_3$, and discussed in the previous chapter, clarify some geometrical features of the dopant site surrounding environment, and how these affect the overall protonic conduction process in this material. Nonetheless, in order to get a more detailed overview of proton hopping mechanisms, we need to know the height of the energy barriers the proton must overcome along its transfer path.

Classical dynamics simulations can supply these informations and, also, they give details on how geometrical parameters change with different temperature, adding further details to the ab initio description in a complementary way. In the following, results* will be presented according to the yttrium content of the supercell used in the simulations (see subsection 3.1.3): $BaZrO_3$ alone, single yttrium substitution and double yttrium substitution. It is here to be recalled that temperature values used in the following simulations are 100, 250, 500, 750, 1000 and 1250K, with a simulation time of 2 ns.

## 6.1 D-BZO and D-BZH Models

The structure of undoped barium zirconate was modelled by means of a $4 \times 3 \times 3$ cubic $Pm\bar{3}m$ supercell as shown in Figure 3.9, here called D-BZO model. In the range of temperatures investigated, the cell parameter $a$ turns out to be directly proportional to the temperature value, growing linearly

*Results presented in this chapter have been obtained by means of the Reax Force Field, kindly provided by Prof. Adri van Duin, Department of Mechanical and Nuclear Engineering, Pennsylvania State University.

according to the relation $\Delta a(T) = 2.11(1 + 2.42 \times 10^{-5}T)$. The thermal expansion coefficient of $2.42 \times 10^{-5}\mathrm{K}^{-1}$ is quite in agreement with that one experimentally found [170], as well as the extrapolated value $a(77) = 4.22$ Å at 77 K as found from NPD data [109]. Also, at low temperatures, the Ba−Ba and the Zr−Zr distances are the ones less affected by thermal motions; for this reason, they can be taken as a further reference to test the geometrical outcomes for this model. Consistently with the atomic positions in the unitary cell, the shorter Ba−Ba and Zr−Zr distance values should be equal to the lattice length; indeed, the radial distribution function $g(r)$ obtained at 100 K for the Ba−Ba and the Zr−Zr couple of atoms has its first local maximum at about 4.22Å, and the corresponding mean square displacements of 0.012 and 0.007 $\mathrm{Å}^2$ are in agreement with the value 0.011 and 0.009 $\mathrm{Å}^2$ as resulted from neutron diffraction experiments cited above. Moreover, using the relation 2.38, we can derive the force constant for the mean force potential between Zr−O and Zr−Ba for the undoped system; these turn out to be 8.46 and 5.75 $\mathrm{eV/Å}^2$ respectively.

Geometrical arrangement of the oxygen atoms in the structure is of fundamental importance for the global process of the protonic conduction, so analysing how it changes with temperature turns to be interesting. Taking as reference one of the oxygen atoms of the structure, radial distribution function $g_{\mathrm{O-O}}(r)$ for the couple O−O has been calculated for each of the temperature values investigated. As it is shown in Figure 6.1[†], the $g_{\mathrm{O-O}}(r)$ functions calculated at the temperature of 100 and 250K reveal a well defined oxygen substructure that changes with temperature, with O−O mean distance values that are not simply the result of temperature broadening but are characteristic of that temperature, like, for example, the bimodal O−O distance distribution round the mean values of 2.84 and 3.26 Å at the temperature of 250K. This substructure is definitively modified at 500K and it will keep almost unvaried at higher temperatures: the temperature broadening of the $g_{\mathrm{O-O}}(r)$ at such temperature generates the corresponding functions at higher temperatures.

This model was used as starting point for studying how proton modifies the features of the Y-doped $BaZrO_3$ structure far from a doped site. In order to do this, the protonated model D-BZH was built, where one hydrogen atom was added to the structure.

The trend of the cell parameter $a$ as a function of the temperature is substantially unvaried compared to the unprotonated case; the presence of hydrogen in the structure does not significantly changes the volume of the local undoped environment and the linear relation between the lattice parameter and the temperature still holds, being $\Delta a(T) = 2.11(1 + 2.48 \times 10^{-5}T)$ for D-BZH models. By means of the relation 2.38 we can derive the force constant for the Zr−O and Zr−Ba mean force potential; the corresponding

[†] All the graphs reported in this chapter have been realized with Gnuplot [171] software.

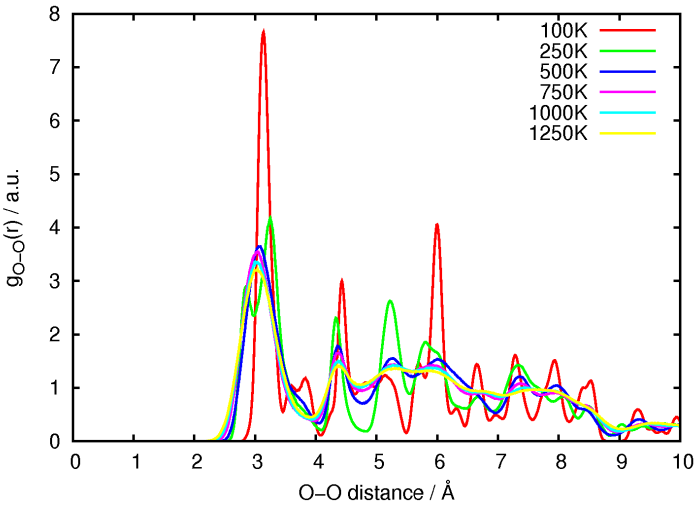


Figure 6.1: Radial distribution functions $g_{O-O}(r)$ for the O−O couple of atoms, calculated at different temperatures for the D-BZO system.

calculated values are 8.53 and 5.85 eV/Å$^2$, slightly higher than the unprotonated case. According to these findings, the vibration frequencies of the Zr−O and Zr−Ba distances should result shifted towards higher values than the unprotonated case; in this sense, the proton has the effect to make the lattice more rigid than in its absence. In assisting protonic transfer, cation-anion vibrational contributions result, in this way, less important than bending motions: O−Zr−O and O−Y−O octahedral axes are allowed to rotate rather than to strecth.

Comparing the radial distribution function for the couple of atoms Zr−O of the unprotonated model with the protonated one, the mean distances distributions and the corresponding spreading width have almost the same value. This trend shows that the proton does not affect the Zr−O long range structure. Analogous results have been obtained for the Zr−Ba distances. Concerning the results for the couple O−O, the radial distribution function $g_{O-O}(r)$ show a temperature trend similar to the one obtained for the unprotonated case, with an oxygen substructure not changing with temperature equal or above 500K. On the other hand, comparing the $g_{O-O}(r)$ on D-BZO and D-BZH taken at the same temperature, oxygen substructure of the unprotonated system results significantly modified by the presence of the proton at low temperatures; for temperatures higher than 250K, the oxygen geometrical arrangement is substantially the same for both unprotonated and protonated cases. For each of the considered temperature values, the $g_{O-O}(r)$ calculated on D-BZH systems shows a very narrow distribution of the O−O mean distance around the value of 1.2Å, this lacking in the

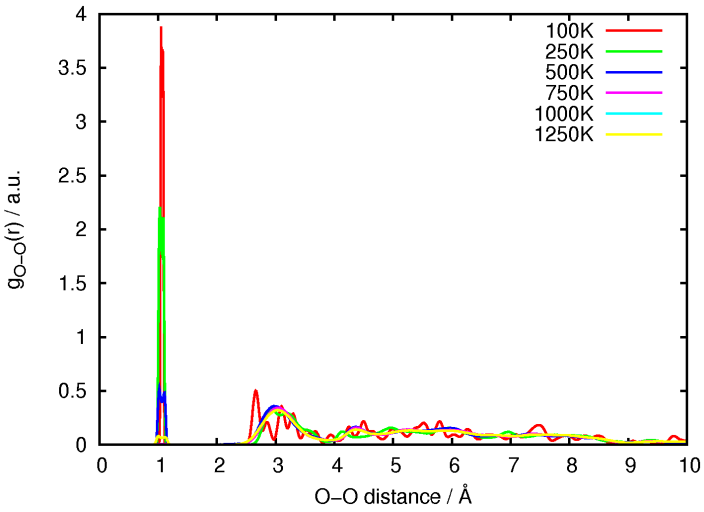


Figure 6.2: Radial distribution functions $g_{\mathrm{O-O}}(r)$ for the O−O couple of atoms, calculated at different temperatures for the D-BZH system. The narrow distribution of the O−O mean distance around the value of 1.2 Å is due to oxygen atoms lying in the proton first coordination shell.

D-BZO model and corresponding to those oxygen atoms lying in the proton first coordination shell (see Figure 6.2).

The simulation time is long enough to enable the proton explores the whole simulation box, allowing a good sampling of the proton diffusion coefficient for each of the considered temperature value. By means of Equation 2.43, this allows to evaluate the activation energy $E_a$ of the proton hopping process between two oxygen sites, that are all equivalent for undoped $BaZrO_3$ compounds. For D-BZH systems, $E_a$ turns out to be 0.32 eV, a value smaller than 0.46 eV experimentally found for the Y:$BaZrO_3$ compound [20]. This result can be checked by calculating the activation energy $E_a$ through the analysis of the residence time of the proton near an oxygen atom for each temperature value. This is done by means of the Arrhenius relation 2.47, that relates the proton residence time $\tau$ to the absolute temperature $T$. The activation energy $E_a$ calculated with this relation is 0.30 eV, coherent with the one found through the analysis of the diffusion coefficient but, as before, lower than the experimental outcome. This result shows that simple hopping process between two zirconium coordinated equivalent oxygen atoms is not enough to account for the global protonic conduction process experimentally observed and other contributions to the activation energy must be considered.That is, only refinement of the present structure do not appear capable of justifying this large difference. It has also to be noted that our simulation model do not include the presence of any

type of defects. It is well known that electron mobility in metals and semiconductors depends strongly upon concentration and type of defects [172]. Absolutely, our simulation model lacks of any type of defects. Oxygen vacancies, e.g., can surely slow proton hopping. Also, we expect that model of doped $BaZrO_3$ describes more correctly the corresponding real system because doping is just equivalent to add specific defects.

## 6.2 D-YBZ and D-YBZ-H Models

Y-doped barium zirconate was modelled starting from the same $4 \times 3 \times 3$ cubic $Pm\bar{3}m$ supercell used for the D-BZO model, in which one zirconium atom has been substituted by an yttrium one, building the D-YBZ model for the present simulations. The relation of the lattice parameter $a$ *vs.* the temperature $T$ is $\Delta a(T) = 2.11(1 + 9.29 \times 10^{-5}T)$: the cell volume increases more rapidly with the temperature than the undoped case. As seen for the undoped D-BZO system, the Ba−Ba and Zr−Zr distances are the one less affected by thermal motions; they can be taken as a further reference to check the $a(T)$ relation, since the shorter Ba−Ba and Zr−Zr distance values should be equal to the lattice length. The radial distribution function $g(r)$ calculated at 100K for these couple of atoms has its first local maximum at about 4.22Å, and the corresponding mean square displacements of 0.012 and 0.007 $Å^2$ are in agreement with the values reported in [109].

The relation 2.38 allow us to derive the force constant for the mean force potential concerning the octahedral cation and its nearest oxygen and barium atoms, that is, for the couples Zr−O, Zr−Ba, Y−O and Y−Ba; the corresponding calculated values are 8.28, 5.70, 11.68 and 4.87 $eV/Å^2$, respectively.

Taking as reference one of the oxygen atoms of the doped octahedron, radial distribution functions $g_{O-O}(r)$ has been calculated for each of the considered temperature values. As it is shown by the $g_{O-O}(r)$ functions in Figure 6.3, an oxygen atom substructure is clearly identified, changing with the temperature. The O−O mean distances at 100K differ from those at 250K, revealing a particular oxygen sub-network activated by the temperature. From 500K on, this sub-network is not changing any more: peaks in the corresponding $g_{O-O}(r)$ undergo temperature broadening, keeping unaltered the pattern of the mean values.

The Y-doped model was extended by adding one proton into the $4 \times 3 \times 3$ supercell, so building D-YBZ-H model. This is intended to reproduce the protonated doped environment in order to study related geometrical features and their influence on the protonic conduction process.

The presence of one proton does not affect the linear dependence of the lattice parameter $a$ with the temperature found for the D-YBZ unprotonated model; increasing the temperature, the lattice parameter $a$ increases more

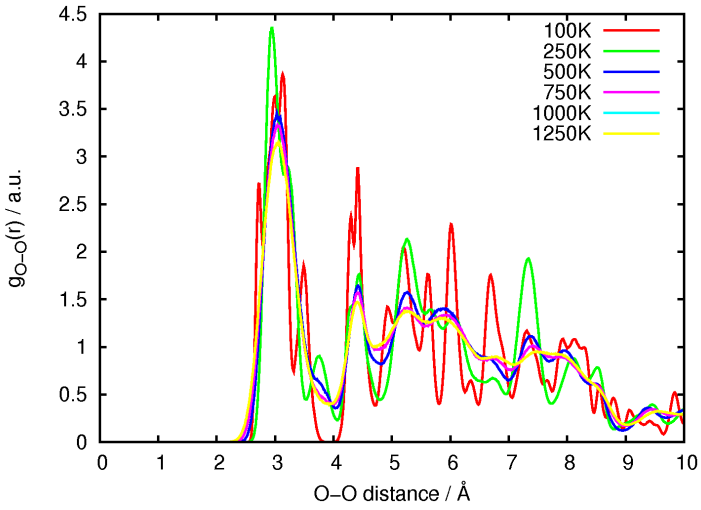


Figure 6.3: Radial distribution functions $g_{\mathrm{O-O}}(r)$ for the O−O couple of atoms, calculated at different temperatures for the D-YBZ model. The reference atom is one of the oxygen atoms surrounding the yttrium atom in the structure.

rapidly than the unprotonated case according to the linear law $\Delta a(T) = 2.11(1 + 9.50 \times 10^{-5}T)$. Also the force constants carried out with D-YBZ model increase if one proton is inserted into the octahedral environment: the whole cation-anion network results more rigid than in the unprotonated case. Thus, the relevant force constants calculated with this model are: *i*) Zr−O, 8.34 eV/Å$^2$; *ii*) Zr−Ba, 5.80 eV/Å$^2$; *iii*) Y−O, 11.78 eV/Å$^2$; *iv*) Y−Ba 4.91 eV/Å$^2$. These values suggest that the corresponding vibrational frequencies are shifted towards higher values compared to the unprotonated case; globally, this can have the effect to reduce the vibrational contribution and to favour the bending one in the proton hopping process.

The radial distribution functions calculated at different temperatures show almost the same distance pattern of the corresponding ones in the D-YBZ model, indicating that the proton does not affect the long range structure. On the other hand, comparing the low temperature $g_{O-O}(r)$ functions of D-YBZ and D-YBZ-H, the oxygen substructure of the unprotonated system results significantly modified by the proton; at temperatures higher than 250K, the oxygen network is definitely established, being the corresponding distance pattern only broadened by thermal motions.

As observed in section 5.3, when one zirconium atom is substituted with an yttrium one, the oxygen sites, that are all equivalent in the cubic undoped structure, are differentiated, gaining features characteristic of the place they occupy into the structure. Recalling the nomenclature used in section 5.3,

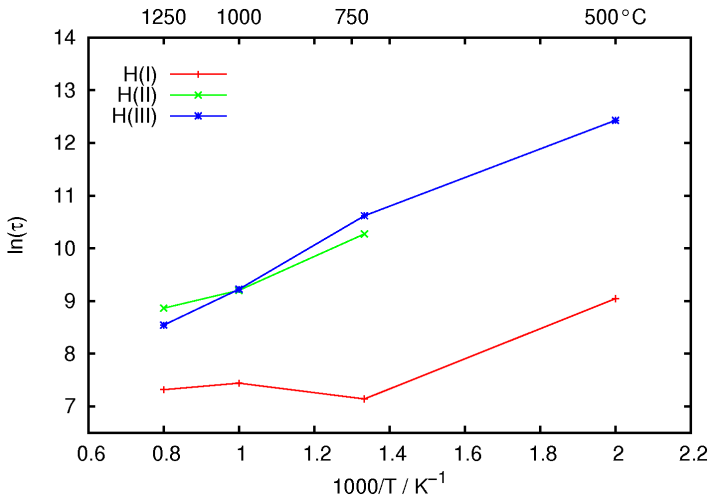


Figure 6.4: Arrhenius plot of the proton residence time for the H(I), H(II) and H(III) sets of proton stable sites in D-YBZ model.

D-YBZ-H geometries own the H1,$\cdots$,H4 different oxygen sites found in the analogous 4x-YBZ-H systems. Different hopping path are thus created, with corresponding different hopping barriers. Analysing how proton diffusion coefficient changes with temperature, it is possible to evaluate the activation energy for the whole protonic conduction, but it is not possible to distinguish which of the hopping paths are the limiting ones for the global process; in other words, the activation energy $E_a$, calculated by considering the entire simulation time, should be regarded as a macroscopic average of the all contributions. By means of Equation 2.43, the extrapolated value of $E_a$ for D-YBZ-H systems is about 0.40 eV, slightly lower than the reference value of 0.43 eV experimentally found [20].

How the different proton pathways weigh in the determination of the global $E_a$ value can be determined analysing the proton residence time near a particular oxygen atom. Looking at the energy diagram showed in Figure 5.2, the oxygen atoms of the D-YBZ-H geometry can be divided into three clusters, according to their stabilization energy. Let us call H(I), H(II) and H(III) the {H1}, {H2} and {H3, H4} sets of stable sites and let us consider the residence time in each of these three clusters. The Arrhenius plot of the residence time $\tau_I$ in the cluster H(I) allows to know the activation energy $E_a^I$ for the intra-octahedral proton hopping between those oxygen atoms belonging to the cluster H(I); in a similar manner, $E_a^{II}$ and $E_a^{III}$ are calculated for the H(II) and H(III) clusters.

Looking at the Figure 6.4, it is possible to see that the relation between $\ln(\tau_I)$ and $1/T$ is not linear in the range of considered temperatures; in order

to obtain the corresponding $E_a^I$ value in the same manner as for the other cases, i.e. by applying Equation 2.47, we will limit to consider only the two values of $\tau_I$ corresponding to the temperatures of 1000K and 1250K, the ordinary working temperatures of these materials, always keeping in mind this strong restriction. The activation energies found for the three clusters are: *i*) H(I), 0.05 eV; *ii*) H(II), 0.23 eV; *iii*) H(III), 0.28 eV. None of these energies is higher than the value of 0.40 eV extrapolated by the diffusion coefficient as a function of the temperature, suggesting that the limiting pathways of the whole proton transfer could be those connecting two of the three considered clusters. However, the global barrier value of 0.40 eV is lower than 0.43 eV, the experimental one; this can be related to an undersampling of inter-cluster hopping of our simulation, whose energy barrier may be higher than the experimental value. Thus, correct estimation of inter-cluster hopping energy barriers requires much longer simulation time. Also this result show that the D-YBZ-H model is not suitable to describe the proton conduction mechanisms in Y:$BaZrO_3$ at different temperature and that it should require refinement; nonetheless, results obtained using D-YBZ-H model suggest that the arrangement of equivalent oxygen atoms sites, according also to their stabilization energies, plays a fundamental role in discriminating about the limiting pathways of the whole protonic conduction process, suggesting to take as reference the ab initio results on alternative dopant environment geometries.

## 6.3 D-2YBZ and D-2YBZ-H Models

Ab initio results on Y:$BaCeO_3$ (see section 4.2) inferred the formation of yttrium clusters when doping with yttrium atoms; so we extended this suggestion to the case of the barium zirconate exploring this peculiar dopant geometrical configuration by means of ab initio methods (see section 5.4). In particular, we observed that, when two nearest neighbour zirconium atoms are each substituted by an yttrium one, oxygen structural sites are distinct, despite they turn out to be equal from considerations on symmetries owned by the system. The effect of such kind of substitution is to single out eight different oxygen sites, so eight corresponding proton stable sites, that we called H1,$\cdots$,H8, with energy relative values like those shown in the diagram 5.7. In order to explore how this structural arrangement affects protonic conduction, we considered a $4\times3\times3$ supercell of $Pm\bar{3}m$ cubic barium zirconate where two nearest neighbour zirconium atoms are substituted by two yttrium ones, building the D-2YBZ model for the MD simulations here presented.

The cell parameter $a$ increases with the temperature according to the law $\Delta a(T) = 2.11(1 + 2.40 \times 10^{-5}T)$; the value $2.40 \times 10^{-5}\mathrm{K}^{-1}$ of thermal expansion coefficient is similar to that one we found with D-BZO model. It

is also in quite agreement with that experimentally found [170]. Compared to the D-BZO and D-YBZ models, the D-2YBZ shows the lowest expansion coefficient, suggesting that the dopant particular configuration counterbalances the volume growth with the temperature. The Ba−Ba and Zr−Zr distances are the ones less affected by thermal motions; they, indeed, reproduce the lattice length of about 4.22 Å at 100K as well as the mean square displacement values as reported in literature [109].

The relation 2.38 allow us to extrapolate the force constant for the mean force potential concerning each kind of octahedral cation and its nearest oxygen and barium atoms. For the couples Zr−O, Zr−Ba, Y−O and Y−Ba the corresponding calculated values are: *i*) Zr−O, 8.44 eV/Å$^2$; *ii*) Zr−Ba, 5.87 eV/Å$^2$; *iii*) Y−O, 10.43 eV/Å$^2$; *iv*) Y−Ba 5.34 eV/Å$^2$. Highest values correspond to highest bond oscillation frequencies. Comparing these force constants with the corresponding ones in D-YBZ model, we note that only the value relative to the Y−O bond results lower; this can be related with the different geometry of the present model, in which the two nearest neighbour yttrium atoms produce a softening the Y−O bond, making more rigid the other ones.

Taking as reference the oxygen atom bound to the two yttrium ones (see Figure 3.9), radial distribution functions have been calculated for each of the considered temperature values; these are shown in Figure 6.5. An oxygen atom substructure is clearly identified, changing with the temperature. The O−O mean distances at 100K differ from those at 250K, revealing a particular oxygen sub-network activated by temperature. The oxygen sub-network at 250K results well established: it holds the peaks position pattern unvaried after temperature increases, spreading the surrounding values according to a typical temperature broadening. Thus, the features of the dopant environment result well defined already at 250K and, in comparison with D-YBZ model, they are less affected by temperature.

The present model was extended by adding one proton into the structure, building the protonated D-2YBZ-H model. The aim is to reproduce the protonated doped environment and to study the related features, comparing them with those of the D-YBZ-H one, in which one yttrium atom is surrounded by only zirconium ones in its octahedral cation first coordination shell.

The lattice length $a$ increases linearly with the temperature more rapidly than for the undoped case, according to the relation $\Delta a(T) = 2.11(1 + 2.71 \times 10^{-5}T)$. Unlike D-YBZ model, the presence of two nearest neighbour yttrium atoms single out a bimodal distribution of the Y−O and Y−Ba distances in yttrium first and second coordination shell; the Y−O mean values found are 2.21 and 2.34 Å while the values for the Y−Ba case are 3.61 and 3.77 Å. Correspondingly, applying the relation 2.38 to values distribution round each of these mean values, two different force constants can be cal-

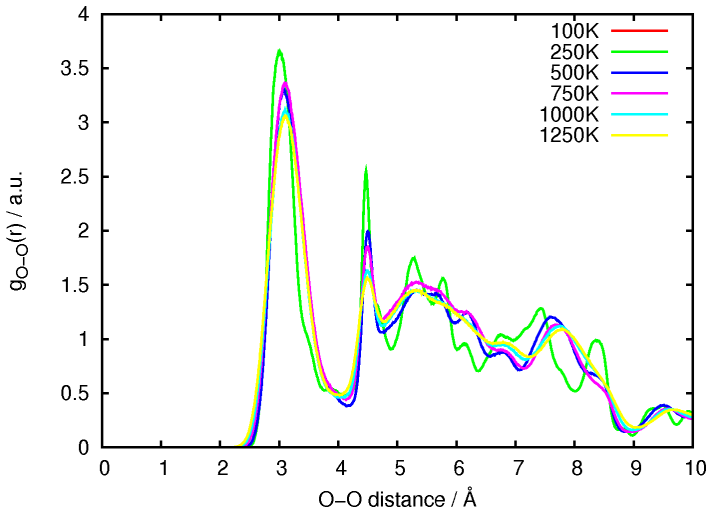


Figure 6.5: Radial distribution functions $g_{O-O}(r)$ for the O−O couple of atoms, calculated at different temperatures for the D-2YBZ model. The oxygen atom used as reference is the one bonding with both the two yttrium atoms of the structure.

culated for the Y−O and Y−Ba mean force potentials; these are: *i*) Y−O, 9.48 and 7.47 eV/Å$^2$ for the mean values of 2.21 and 2.34 Å; *ii*) Y−Ba, 7.64 and 3.89 eV/Å$^2$ for the mean values of 3.61 and 3.77 Å. The present force constants values appear to be the split of the corresponding D-YBZ ones, as well as the relative mean distances; this corresponds to two different vibrational frequencies for each of the considered bonds. In particular, within the same doped octahedron, the oxygen atoms oscillate in two different ways, making more anisotropic the intra-octahedral proton transfer. This is a peculiar feature of the dopant geometrical environment due to the particular mutual position of the two yttrium atoms. The remaining force constants found are: *i*) Zr−O, 8.37 eV/Å$^2$; *ii*) Zr−Ba, 4.78 eV/Å$^2$. Almost all the values are lower than the corresponding ones in the undoped case; at variance of what we saw for D-BZH and D-YBZ-H models, the presence of the proton softens the host matrix, lowering the bond vibrational frequencies.

The oxygen sub-structure still holds the behaviour found in the unprotonated case as a function of the temperature. The peculiar feature is the further narrow distribution of the O−O mean distances around the value of 1.3 Å, corresponding to those oxygen atoms lying in the proton first coordination shell.

The eight different oxygen sites single out hopping pathways with different activation energy barriers. Analysing how proton diffusion coefficient changes with temperature, it is possible to estimate the activation energy

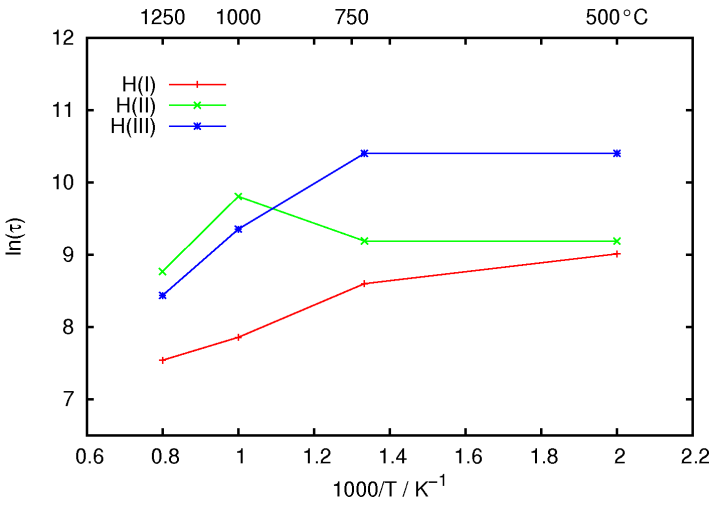


Figure 6.6: Arrhenius plot of the proton residence time for the H(I), H(II) and H(III) sets of proton stable sites in D-2YBZ model.

$E_a$ for the whole protonic process without to distinguish about the different transfer paths; in this way, $E_a$ should be seen as a macroscopic average of the single contributions. By means of Equation 2.43, the extrapolated value of $E_a$ for D-2YBZ-H systems is about 0.47 eV, higher than the experimental value of 0.43 eV [20].

By analysing the proton resident time near an oxygen atom lying in a given site, it is possible to estimate how different proton pathways contribute to the determination of the global $E_a$ value. Looking at the energy diagram of Figure 5.7, the oxygen atoms of the D-2YBZ-H geometry can be grouped into three clusters, according to their stabilization energy. Let us call H(I), H(II) and H(III) the {H1, H2}, {H3, H4, H5, H6} and {H7, H8} sets of stable sites and let us consider the residence time in each of these three clusters. The Arrhenius plot of the residence time $\tau_I$ in the cluster H(I) allows to extrapolate the activation energy $E_a^I$ for the intra-octahedral proton hopping between those oxygen atoms belonging to the cluster H(I); in a similar manner, $E_a^{II}$ and $E_a^{III}$ are calculated for the H(II) and H(III) clusters.

The residence time $\tau$ calculated at 500K for all the three clusters (see Figure 6.6), cannot be taken into account for extrapolating the activation energy, since at that temperature, the proton does not significantly change its position along the simulation; however such values can be taken as lower limits for the corresponding residence times.

The relation between $\ln(\tau_{II})$ and $1/T$ is not linear in the range of the considered temperature values; in order to obtain the corresponding $E_a^{II}$

value in the same way as for the other clusters, we will limit to consider only the two values of $\tau_{II}$ for temperatures equal and higher than 1000K, being these values inside the working temperatures range of the considered material. This strong limitation is useful only to make a rough estimation of the activation energy barrier for cluster H(II) in a way coherent with the extrapolations for H(I) and H(III) clusters. The deviation of $\tau_{II}$ from Arrhenius behaviour suggest a more detailed analysis of the mechanisms of proton hopping inside the cluster H(II), whose $E_a^{II}$ value can be regarded as the result of a first order approximation of a more complex $\tau(T)$ expression.

The activation energies found for the three clusters are: *i*) H(I), 0.17 eV; *ii*) H(II), 0.45 eV; *iii*) H(III), 0.31 eV. Because of the low activation energy of H(I) cluster, the number of O→O jumps per unit time between the H1 and H2 stable sites is higher than others: the proton motion in the zone between two yttrium atoms is faster than in the others. This situation is better illustrated in Figure 6.7. In the abscissa, simulation time is reported; the red line is referred to the $y$-axis on the left which reports the atomic labels assigned to oxygen atoms while the green line refers to the $y$-axis on the right representing the cluster label. The red line specifies the oxygen atom nearest to the proton at simulation time reported in abscissa; the green line represents the cluster to which the proton belongs at the corresponding time. It is evident from the figure that the proton jumps rapidly between oxygen atoms belonging to the H(I) cluster while it resides for longer time near one and the same oxygen atom when this last one belongs to the H(II) cluster.

Since none of the three activation energy values are higher than the energy of 0.47 eV found analysing the temperature dependence of the diffusion coefficient, the limiting pathway of the whole proton transfer could be one connecting two of the considered clusters. On the other hand, the energy differences between all the stable sites calculated by means of the 4x-2YBZ-H$n$ models suggest the presence of barriers higher than 0.50 eV for a proton migration between H(II) and H(III) clusters. However, let us recall here that the yttrium contents of the $4 \times 3 \times 3$ supercell used for the present dynamics simulations resemble about a 4% of yttrium doping; as observed in section 5.4, higher dopant concentrations will lead to an overlap of the three considered clusters. In particular, H(II) cluster would increase its size to the detriment of H(III) one, becoming the region of the material in which the proton would spend most of the time; correspondingly, $E_a^{II}$ activation energy would be the predominant contribution to the global value observed for the whole protonic conduction process. Indeed, the $E_a^{II}$ value seems to reproduce quite well the experimental one.

Besides giving a contribution to the explanation of the experimental findings, this result suggest also that a reliable model of the protonic conduction process in Y:$BaZrO_3$ should pay attention more to the local environment in which the proton moves than to the system global features due to con-

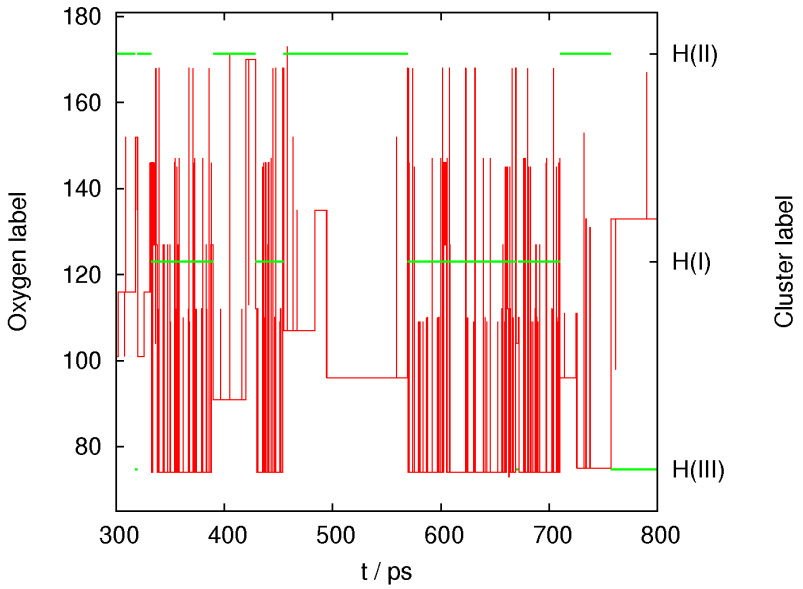


Figure 6.7: Proton hopping in H(I), H(II) and H(III) clusters of D-2YBZ model as a function of the time. The red line is referred to the $y$-axis on the left, which reports the label of the oxygen atoms, and represents the oxygen atom nearest to the proton at simulation time reported in abscissa; the green line refers to the $y$-axis on the right, which reports the cluster label, and represents the cluster to which the proton belongs at the corresponding time. The proton jumps rapidly between oxygen atoms belonging to the H(I) cluster.

siderations based on the kind of the involved atomic species. If the last approach could be a good starting point to study the protonic diffusion as a whole, local details give important informations on the limiting steps of the conduction mechanism. According to the obtained results, the most reliable dopant environment geometry in Y:$BaZrO_3$ should be the one in which two yttrium atoms are first neighbour in the octahedral cation coordination shell. Furthermore, stabilization energies of the 4x-YBZ models, activation energies extrapolated with D-YBZ-H model, considerations on proton residence times and the rapidity of the proton motion near the doped sites, together with the conclusions about the geometry of the doped site, suggest that protonic conduction in Y:$BaZrO_3$ could be improved avoiding yttrium clusterization in moieties of the kind Y−O−Y. In order to do this, it turns out to be necessary a detailed analysis of the reaction mechanisms that from the initial reactants lead to the formation of the final material.

# Conclusions

As stated in the **Introduction**, aim of this study is to do a further step in understanding structural and dynamical aspects of proton conduction in a class of solid protonic conductors. Specifically, computational studies (ab initio and molecular dynamics) have been done on barium cerate and barium zirconate perovskite structures, doped with different trivalent species in the tetravalent cation octahedral site.

We have summarized our results into two sections: results from ab initio models and results from molecular dynamics.

**Ab Initio Results.** Models of barium cerate derivatives have been obtained by substituting cerium atom with yttrium, indium or gadolinium ones. The size of the suggested fragment was shown to be a good compromise between the physical consistency of the numerical results and the computational resources used to get them. Particular care were devoted to the choice of the basis sets, in order to get structure results in better agreement with the experimental ones. In fact, this appears critical in In:$BaCeO_3$ derivatives. Similarly, results on Gd:$BaCeO_3$ system suggest that also the choice of the energy functional is of fundamental importance to get a reliable description of such doped systems.

For $BaCeO_3$ compounds, concurrent use of C-SPA/P-DOS analysis and the *M-ca* procedure, considered together, would seem able to rationalize both structural and conducting properties of the doped sites on pure electronic basis. In particular, in order to increase the material conductivity, a dopant species has to leave unchanged, or even decrease, the local basicity of the oxygen octahedral environment; moreover, small structural changes, not affecting the basicity, seem to be less effective in producing conductivity modifications.

The present approach suggested a possible origin of the bimodal Y−O distance distribution recently found by EXAFS experiments on Y-doped $BaCeO_3$ materials. By means of our *double substitution* models, such experimental findings are explained on the basis of local clustering of yttrium atoms.

Starting from the structural outcomes, based on geometric and electronic considerations, it is possible to self-consistently analyse also the charge

distributions characterizing the Y-doped $BaCeO_3$ materials. In particular, charge gradient considerations let us to confirm the common view that the protonic intra-octahedral hopping is more likely to occur than the inter-octahedral one in the bulk of $BaCeO_3$ derivatives; furthermore, the gradients in the concentration of the charge density around dopant atoms should play a minor role in the same protonic diffusion.

The models of barium cerate compounds summarized above have been used to describe the corresponding protonated environment. Proton surrounding atomic geometries during the hopping event, were explored by keeping fixed proton positions along a possible hopping path, with respect to an external cage. Results show that the proton reorganizes the octahedral distances and charges distribution in a way essentially irrespective of the type of the octahedral cation; in particular, oxygen atoms octahedron shows an axial and a planar distortions. Four octahedral oxygen atoms are arranged in a plane containing the hydrogen atom; during proton motion from one oxygen site to another, such plane always contains the hydrogen atom together with the oxygen ones. In this sense, proton motion in barium cerate derivatives has been called as *planar*, inferring that it should keep its directional characteristics against thermal vibrations: the property of being planar is due only to the presence of the proton and not to the type of the nearest octahedral cation. On the other hand, the octahedral cation atomic type mainly determines distance and angle values between the proton and the involved anions and cations; as an example, in In:$BaCeO_3$, the shrinking of the oxygen atoms octahedron round the dopant atom and a small dihedral angle value involving the proton make unfavourable a proton jump towards cerium-coordinated oxygen atoms, lowering proton ability to diffuse into the bulk.

Relevant results on Y:$BaCeO_3$ have leaded to the formulation of analogous models to study the yttrium-doped barium zirconate perovskite. Single and double zirconium substitutions with yttrium atoms have been considered, in the aim to understand if the inferred yttrium local clustering is a general feature of the yttrium atom as a substituent for the tetravalent cation in perovskite materials.

Singly and doubly substituted Y:$BaZrO_3$ models shows that yttrium doping does not change the $Pm\bar{3}m$ cubic structure of the undoped compound; with such symmetry, oxygen sites are all equivalent. After yttrium doping, more than two distinct oxygen sites are singled out, despite symmetries of the undoped system are preserved. When only one zirconium atom is substituted by an yttrium one, four distinct oxygen sites are individuated with four different stabilization energies for the proton. The number of distinct oxygen sites grows up to eight by considering the simultaneous presence of two nearest neighbour yttrium atoms.

The features of such distinct oxygen sites are highlighted in presence of a proton, that acts as a probe of their response to a structural perturbation.

Distinct proton stable sites correspond to distinct oxygen sites. Proton ability of locally specialize oxygen sites overlaps with the features of these last ones. The effect of this overlapping is reflected into the relative energies of the proton stable positions.

Differences among stabilization energies found for the singly doped barium zirconate models are not able alone to explain the activation energy for the proton hopping process obtained in experiments. In presence of two nearest neighbour yttrium atoms, relative energy differences of the eight proton stable sites reproduce the correct order of magnitude of the proton hopping activation energy value. Distribution of such energy values clearly suggest to group distinct oxygen atoms into three clusters, owning peculiar structural features not immediately evident from an inspection of the geometrical positions of their constituents.

**Molecular Dynamics Results.** Ab initio results on $BaZrO_3$ derivatives are the basis of MD simulations performed on yttrium-doped barium zirconate. Dynamics simulations models take into account undoped as well as singly and doubly doped structures. Results of MD simulation add temperature dependence to ab initio outcomes *i*) of structural details, *ii*) of proton motion. As to structural details, a peculiar oxygen sub-network is individuated, changing its characteristics up to a temperature value which depends on the yttrium content. Protonated models reproduce the behaviour inferred by the corresponding ab initio results: only the system with two yttrium atoms is able to account for the macroscopic protonic conduction activation energy. This fact confirms the ab initio suggestions that the three oxygen atoms clusters had their own peculiar structural features; in particular, two of them act as a multilevel trap for the proton, delaying its diffusion across the bulk. A singular feature of this proton trap is found in the cluster near a doped site: a very high number of proton hopping events per unit time between those oxygen atoms surrounding an yttrium one.

Summing up ab initio and dynamics simulation results on yttrium-doped barium zirconate systems, it appears that yttrium clusterization occurs also for such compounds; eventually, protonic conduction in these materials could be improved avoiding such clusterization, that is preventing the formation of protonic traps.

All results have shown the close interrelation between structure and dynamics of matter at a microscopic level. They also show the importance of combined use of experimental and computational approaches to the proton conduction problem to clarify all the story. As a fruitful consequence of this view, we suggest that better efficiency of proton conduction of perovskite can be accomplished by studying in details (experimentally and computationally) the reaction mechanisms that from the initial reactants lead to the formation of the final material.

# Acknowledgements

My Ph.D. work would not have been possible without the essential help of my tutors, Prof. Emanuele and Prof. Duca, and without the precious advices of Prof. Martorana: I acknowledge their constant dedication they demonstrated me since the beginning and for their professional effort in assisting my work.

I will never get tired to thank my parents, my brother Vincenzo and all my dears who always trusted in all my choices and who always have been able to find words of comfort for the most difficult moments.

I thankfully acknowledge Prof. Pablo Ordejón of the "Centre d'Investigació en Nanociéncia i Nanotecnologia" (CIN2, CSIC-ICN, Barcelona – Spain), for making me welcome in his group and his willingness in assisting my work throughout and beyond my staying in Barcelona.

I give my thanks to Prof. Marco Cannas of the Department of Physical and Astronomical Sciences, University of Palermo, to Prof. Luis Seijo of the Department of Chemistry, Universidad Autónoma de Madrid, and to Prof. Javier Junquera, Department CITIMAC, Universidad de Cantabria, for their precious review work on the present thesis.

No words are enough to say thanks to the great family C.G.B. and all my old dear friends, who always approved and supported me since we met, for all the great moments they offered me. Each of them unique and irreplaceable. Among them, I thankfully acknowledge the work done by my friend Giuseppe to create a special cover layout (different from the standard one) for the present thesis.

I give a particular acknowledgement to the "CCCP" group of the Inorganic and Analytic Chemistry Department: Sergio, Teresa, Remedios, Nerina, Franco, who helped me in resolving the little problems throughout this trip.

I will never forget my friends in Barcelona with whom I shared all the moments of that wonderful experience: Hernan, Francesca, Alberto, Mario, Martina, Juanma.

I give my thanks to Prof. Adri van Duin of the Department of Mechanical and Nuclear Engineering, Pennsylvania State University, for kindly having supplied me the force field he developed for yttrium doped barium zirconate systems, allowing the realization of a fundamental part of this work.

This work has been supported by: Università degli Studi di Palermo, Inorganic and Analytic Chemistry Department (ex 60%: *Ossidi Misti a Base di Cerato di Bario: Sintesi, Caratterizzazione Strutturale e Studio Computazionale del Meccanismo di Conduzione Protonica*); COMETA consortium, to which Università di Palermo belongs as a partner; HPC-EUROPA2 project (project number: 228398) with the support of the European Commission - Capacities Area - Research Infrastructures.

# Bibliography


[1] Fischer, S. F., Hofacker, G. L., and Rathner, M. A. *J. Chem. Phys.* **52**, 1934 (1970).

[2] Sabin, J. R., Fischer, S. F., and Hofacker, G. L. *Int. J. Quantum Chem.* **3 (Pt.1)**, 257 (1969).

[3] Fischer, S. F. and Hofacker, G. L. *Phys. Ice Proc. Int. Symp.* , 369 (1969).

[4] Fischer, S. F., Hofacker, G. L., and Sabin, J. R. *Phys. Kondens. Mater.* **8**, 268 (1969).

[5] Kreuer, K. D., Weppner, W., and Rabenau, A. *Angew. Chem., Int. Ed. Engl.* **21**, 208 (1982).

[6] van Grotthuss, C. J. D. *Ann. Chim.* **58**, 54 (1806).

[7] Frank, H. S. *Proc. R. Soc. London* **A247**, 481 (1958).

[8] Kreuer, K. D. *Chem. Mater.* **8**, 610–641 (1996).

[9] Born, M. and Oppenheimer, J. R. *Ann. Physik* **84**, 457 (1927).

[10] Alig, H., Lösel, J., and Trömel, M. Z. *Kristallogr.* **209**, 18 (1994).

[11] Borgis, D., Tarjus, G., and Azzouz, H. J. *Chem. Phys.* **97**, 1390 (1992).

[12] Islam, M. S., Davies, R. A., Fisher, C. A. J., and Chadwick, A. V. *Solid State Ionics* **145**, 333–338 (2001).

[13] Norby, T. *Solid State Ionics* **125**, 1–11 (1999).

[14] Kreuer, K. D. *Solid State Ionics* **97**, 1–15 (1997).

[15] Kreuer, K. D. *Solid State Ionics* **125**, 285–302 (1999).

[16] Larring, Y. and Norby, T. *Solid State Ionics* **70–71**, 305–310 (1994).

[17] Norby, T. and Christiansen, N. *Solid State Ionics* **77**, 240–243 (1995).

[18] Phair, J. W. and Badwal, S. P. S. *Ionics* **12**, 103–115 (2006).

[19] Alberti, G. and Casciola, M. *Solid State Ionics* **145**, 3–16 (2001).

[20] Kreuer, K. D. *Annu. Rev. Mater. Res.* **33**, 333–359 (2003).

[21] Takahasho, T. and Iwahara, H. *Rev. Chim. Miner.* **17**, 243 (1980).

[22] Iwahara, H., Esaka, T., Uchida, H., and Maeda, N. *Solid State Ionics* **3–4**, 359 (1981).

[23] Iwahara, H., Asakura, Y., Katahira, K., and Tanaka, M. *Solid State Ionics* **168**, 299–310 (2004).

[24] Tomita, A., Hibino, T., Suzuki, M., and Sano, M. *J. Mater. Sci.* **39**, 2493–2497 (2004).

[25] Lufaso, M. W. B. S. *Perovskite synthesis and analysis using structure prediction diagnostic software*. PhD thesis, The Ohio State University, (2002).

[26] Momma, K. and Izumi, F. *J. Appl. Crystallogr.* **41**, 653–658 (2008).

[27] Kimball, S., Mattis, P., et al. GNU Image Manipulation Program, Version 2.6.8, http://www.gimp.org.

[28] Kreuer, K. D., Fuchs, A., and Maier, J. *Solid State Ionics* **77**, 157–162 (1995).

[29] Islam, M. S. *J. Mater. Chem.* **10**, 1027–1038 (2000).

[30] Wakamura, K. *J. Phys. Chem. Solids* **66**, 133–142 (2005).

[31] Kreuer, K. D., Adams, S., Münch, W., Fuchs, A., Klock, U., and Maier, J. *Solid State Ionics* **145**, 295 (2001).

[32] Hempelmann, R., Karmonik, C., Matzke, T., Cappadonia, M., Stimming, U., Springer, T., and Adams, M. A. *Solid State Ionics* **77**, 152–156 (1995).

[33] Matzke, T., Stimming, U., Kramonik, C., Soetratmo, M., Hempelmann, R., and Güthoff, F. *Solid State Ionics* **86-88**, 621 (1996).

[34] Davies, R. A., Islam, M. S., and Gale, J. D. *Solid State Ionics* **126**, 323 (1999).

[35] Islam, M. S., Davies, R. A., and Gale, J. D. *Chem. Mater.* **13**, 2049–2055 (2001).

[36] Islam, M. S., Slater, P. R., Tolchard, J. R., and Dinges, T. *Dalton Trans.* , 3061–3066 (2004).

[37] Iwahara, H., Esaka, T., Uchida, H., Yamauchi, T., and Ogaki, K. *Solid State Ionics* **18–19**, 1003–1007 (1986).

[38] Iwahara, H., Yajima, T., Hibino, T., Ozaki, K., and Suzuki, H. *Solid State Ionics* **61**, 65–69 (1993).

[39] Iwahara, H., Uchida, H., Ogaki, K., and Nagato, H. *J. Electrochem. Soc.* **138**, 295–299 (1991).

[40] Yahima, T., Iwahara, H., Koide, K., and Yamamoto, K. *Sensors Actuators B5* **145** (1991).

[41] Fukuoka, November (1983).

[42] Yahima, T., Koide, K., Yamamoto, K., and Iwahara, H. *Denki Kagaku* **58**, 547 (1990).

[43] Iwahara, H. *Solid State Ionics* **77**, 289–298 (1995).

[44] The Solid State Ionics Society of Japan, (2000).

[45] Matsumoto, H., Hayashi, H., and Iwahara, H. *J. Nucl. Sci. Technol.* **39**, 367–370 (2002).

[46] Bonanos, S. and Mogensen, M. *Solid State Ionics* **97**, 483–488 (1997).

[47] Marnellos, G. M., Kyriakou, A., Florou, F., Angelidis, T., and Stoukides, M. *Solid State Ionics* **125**, 279–284 (1999).

[48] Bonanos, S. *Solid State Ionics* **145**, 265–274 (2001).

[49] Schober, T. *Solid State Ionics* **144**, 379–386 (2001).

[50] Kakuta, T., Hirata, S., Mori, S., Konishi, S., Kawamura, Y., Nishi, M., and Ohara, Y. *Fus. Sci. Technol.* **41**, 1069 (2002).

[51] Matsumoto, H., Hamajima, S., and Iwahara, H. *Solid State Ionics* **145**, 25–29 (2001).

[52] Tsotsis, T. T., Minet, R. G., Champagnie, A. M., and Liu, P. T. K. *Catalytic membrane reactors, computer aided design of catalysts.* New York, (1993).

[53] Vayenas, C. G. *Solid State Ionics* **28–30**, 1521–1539 (1988).

[54] Stoukides, M. *Ind. Eng. Chem. Res.* **27**, 1745–1750 (1988).

[55] Vayenas, C. G., Bebelis, S. I., Yentekakis, I. V., and Lintz, H. G. *Catal. Today* **11**, 303–438 (1992).

[56] Vayenas, C., Jacksic, M., Bebelis, S., and Neophytides, S. *Modern aspect in electrochemistry*, chapter The electrochemical activation of catalytic reactions, 57. New York (1996).

[57] Vayenas, C., Bebelis, I., Yentekakis, I., and Neophytides, S. *The CRC handbook of solid state electrochemistry*, chapter Electrocatalysis and electrochemical reactors, 445. Boca Raton, FL (1997).

[58] Eng, D. and Stoukides, M. *Catal. Rev–Sci. Eng.* **33**, 375 (1991).

[59] Stoukides, M. *J. Appl. Electrochem.* **25**, 899–912 (1995).

[60] Stoukides, M. *Cat. Rev. Sci. Eng.* **42**, 1– (2000).

[61] Marnellos, G. and Stoukides, M. *Solid State Ionics* **175**, 597–603 (2004).

[62] Fabry, P. and Siebert, E. *The CRC handbook of solid state electrochemistry*, chapter 11, 371–406. Boca Raton, FL (1997).

[63] Hammou, A. *Advances in electrochemical science and engineering*. VHC, New York (1992).

[64] Kordesch, K. and Simander, G. *Fuel cells and their applications*. VHC, New York (1996).

[65] Julien, C. *The CRC handbook of solid state electrochemistry*, chapter Solid state batteries. CRC Press, Boca Raton, FL (1997).

[66] Alqahtany, H., Eng, D., and Stoukides, M. *J. Electrochem. Soc.* **140**, 1677– (1993).

[67] Alqahtany, H., Eng, D., and Stoukides, M. *Energy and Fuels* **7**, 495 (1993).

[68] Marnellos, G. and Stoukides, M. *Science* **95**, 282 (1998).

[69] Tsiplakides, D., Bebelis, S., Pliangos, C., Brosda, S., and Vayenas, C. G. *Electrochemical activation of catalysis*. Kluwer Academic, Plenum, New York, (2001).

[70] Song, C. *Catal. Today* **77**, 17–49 (2002).

[71] Flavin, C. and DUnn, S. *State of the World, Worldwatch Institute*, chapter Reinventing the energy system. Washington, DC, 118 edition (1999).

[72] Marland, G., Boden, T. A., and Andres, R. J. *Trends: A Compendium of Data on Global Change*, chapter Global, regional and national $CO_2$ emissions. Oak Ridge National Laboratory, Oak Ridge, TN, USA (2000).

[73] Groove, W. R. *Philos. Mag.* **14**, 127–130 (1839).

[74] Larminie, J. and Dicks, A. L. *Fuel cell systems explained*. Wiley, New York, (2000).

[75] Carrette, L., Friedrich, K. A., and Stimming, U. *Fuel Cells* **1**, 5–39 (2001).

[76] Hirschenhofer, J. H., Stauffer, D. B., Engleman, R. R., and Klett, M. G. *Fuel Cell Handbook*. Federal Energy Technology Center, Morgantown, WV, 4th edition, (1998).

[77] Ganascia, J. G. *Les Nouvelles d'Archimède* **51**, 18–19 (2009).

[78] Knight, K. S. *Solid State Ionics* **145**, 275–294 (2001).

[79] Glockner, R., Islam, M. S., and Norby, T. *Solid State Ionics* **122**, 145–156 (1999).

[80] Davies, R. A., Islam, M. S., Chadwick, A. V., and Rush, G. E. *Solid State Ionics* **130**, 115–122 (2000).

[81] Wu, J., Davies, R. A., Islam, M. S., and Haile, S. M. *Chem. Mater.* **17**, 846–851 (2005).

[82] Shukla, A., Dolg, M., Stoll, H., and Fulde, P. *J. Chem. Phys. Letters* **262**, 213–218 (1996).

[83] van Santen, R. A. *J. Mol. Catal. A: Chem.* **115**, 405–419 (1997).

[84] Cammarata, A., Martorana, A., and Duca, D. *J. Phys. Chem. A* **113**, 6381–6390 (2009).

[85] Giannici, F., Longo, A., Deganello, F., Balerna, A., Aricò, A. S., and Martorana, A. *Solid State Ionics* **178**, 587–591 (2007).

[86] Longo, A., Giannici, F., Balerna, A., Ingrao, C., Deganello, F., and Martorana, A. *Chem. Mater.* **18**, 5782–5788 (2006).

[87] Roothaan, C. C. J. *Rev. Mod. Phys.* **23**(2), 69–89 (1951).

[88] Rabuk, A. and Scuseria, G. E. *J. Chem. Phys.* **110**, 695–700 (1999).

[89] Levine, I. N. *Quantum Chemistry*. 5th edition, (2000).

[90] Hoenberg, P. and Kohn, W. *Phys. Rev.* **136**, 864–871 (1964).

[91] Kohn, W. and Sham, L. J. *Phys. Rev.* **137**, 1697–1705 (1965).

[92] Derlet, P. M. and Dudarev, S. L. *Progress in Materials Science* **52**, 299–318 (2007).

[93] Feynman, R. P. *Phys. Rev.* **56**, 340 (1939).

[94] Foresman, J. B. and Frisch, A. *Exploring Chemistry with Electronic Structure Methods.* Gaussian Inc., Pittsburgh, PA, 2th edition, (1996).

[95] Mulliken, R. S. *J. Chem. Phys.* **23**, 1833–1840 (1955).

[96] Mulliken, R. *J. Chem. Phys.* **23**, 1841–1846 (1955).

[97] Mulliken, R. *J. Chem. Phys.* **23**, 2338–2342 (1955).

[98] Mulliken, R. *J. Chem. Phys.* **23**, 2343–2346 (1955).

[99] Stout, E. W. and Politzer, P. *Theoretica Chimica Acta* **12**, 379–386 (1968).

[100] Christoffersen, R. E. and Baker, K. A. *Chem. Phys. Lett.* **8**, 4–9 (1971).

[101] Grabenstetter, J. E. and Whitehead, M. A. *Theoretica Chimica Acta* **26**, 390 (1972).

[102] Gorelsky, S. I. and Lever, A. B. P. *J. of Organometallic Chem.* **635**, 187–196 (2001).

[103] Ros, P. and Schuit, G. C. A. *Theoretica Chimica Acta* **4**, 1–12 (1966).

[104] Löwdin, P. O. *Adv. Quantum. Phys.* **5**, 185–199 (1970).

[105] Zhang, S. B. and Northrup, J. E. *Phys. Rev. Lett.* **67**, 2339–2342 (1991).

[106] Croxton, C. A. *Introduction to Liquid State Physics.* (1975).

[107] Giacovazzo, C., Monaco, H. L., Artioli, G., Viterbo, D., Ferraris, G., Gilli, G., Zanotti, G., and Catti, M. *Fundamental of Crystallography.* Oxford University Press, 2th edition, (2002).

[108] Levin, I., Amos, T. G., Bell, S. M., Farber, L., Vanderah, T. A., Roth, R. S., and Brian, H. T. *J. Solid State Chem.* **175**, 180–181 (2003).

[109] Lucazeau, G., Pagnier, T., Charrier-Cougoulic, I., and Ritter, C. *E. P. J. Applied Physics* **9**, 1–19 (2000).

[110] Larring, Y. and Norby, T. *Solid State Ionics* **77**, 147–151 (1995).

[111] Cherry, M., Islam, M. S., Gale, J. D., and Catlow, C. R. A. *J. Phys. Chem.* **99**, 14614–14618 (1995).

[112] Fabbri, E., Pergolesi, D., Licoccia, S., and Traversa, E. *Solid State Ionics* **181**, 1043–1051 (2010).

[113] Krith, A. and Irvine, J. T. S. *Solid State Ionics* **162–163**, 83–91 (2003).

[114] Kompan, M. E., Baikov, Y. M., Melekh, B. A. T., and Volchek, B. Z. *Solid State Ionics* **162–163**, 1–5 (2003).

[115] Stokes, S. J. and Islam, M. S. *J. Mater. Chem.* **20**, 6258–6264 (2010).

[116] Cammarata, A., Ordejón, P., and Duca, D. *Science and Supercomputing in Europe, HPC-Europa Transnational Access report 2010*, chapter Computational studies on systems derived from barium zirconate perovskite structure. (In press.).

[117] Cammarata, A. unpublished, (2011).

[118] Knight, K. S. *Solid State Ionics* **127**(1–2), 43–48 (2000).

[119] Shimojo, F. and Hoshino, K. *Solid State Ionics* **145**, 421–427 (2001).

[120] Münch, W., Kreuer, K. D., Adams, S., Seifert, G., and Maier, J. *Phase Transition* **68**, 567–586 (1999).

[121] Maekawa, H., Kashii, N., I., K. J., Hinatsu, Y., and Yamamura, T. *Solid State Ionics* **122**, 231–236 (1999).

[122] Omata, T., Takagi, M., and Otsuka-Yao-Matsuo, S. *Solid State Ionics* **168**, 99–109 (2004).

[123] Münch, W., Seifert, G., Kreuer, K. D., and Maier, J. *Solid State Ionics* **97**, 39–44 (1997).

[124] Islam, M. S. *Solid State Ionics* **154–155**, 75–85 (2002).

[125] Giannici, F., Longo, A., Balerna, A., Kreuer, K. D., and Martorana, A. *Chem. Mater.* **21**, 2641–2649 (2009).

[126] Jena, H., Kutty, K. V. G., and Kutty, T. R. N. *Mat. Res. Bull.* **39**, 489–511 (2004).

[127] Yamazaki, Y., Hernandez-Sanchez, R., and Haile, S. M. *Chem. Mater.* **21**, 2755–2762 (2009).

[128] Duval, S. B. C., Holtappels, P., Vogt, U. F., Stimming, U., and Graule, T. *Fuel Cells* **5**, 613–621 (2009).

[129] Kruth, A., Davies, R. A., Islam, M. S., and Irvine, J. T. S. *Chem. Mater.* **19**, 1239–1248 (2007).

[130] Dick, B. J. and Overhauser, A. W. *Phys. Rev.* **112**, 90–103 (1958).

[131] Mott, N. F. and Littleton, M. J. *Trans. Faraday Soc.* **34**, 485–499 (1938).

[132] Saul, P., Catlow, C. R. A., and Kendrick, J. *Phil. Mag. B* **51**, 107 (1985).

[133] Björketun, M. E., Sundell, P. G., and Wahnström, G. *Faraday Discuss.* **134**, 247–265 (2007).

[134] Shi, C., Yoshino, M., and Morinaga, M. *Solid State Ionics* **176**, 1091–1096 (2005).

[135] Munch, W., Kreuer, K. D., Seifert, G., and Maier, J. *Solid State Ionics* **136–137**, 183–189 (2000).

[136] Munch, W., Seifert, G., Kreuer, K. D., and Maier, J. *Solid State Ionics* **86–88**, 647–652 (1996).

[137] Cammarata, A. *Science and Supercomputing in Europe, HPC-Europa Transnational Access report 2007*, chapter Computational studies of the structure and of the proton transport phenomena in systems derived from barium cerate perovskite structure, 119–129. Casalecchio di Reno, Bononia (2007).

[138] Frisch, M. J., Trucks, G. W., Schlegel, H. B., Scuseria, G. E., Robb, M. A., Cheeseman, J. R., Montgomery Jr., J. A., Vreven, T., Kudin, K. N., Burant, J. C., Millam, J. M., Iyengar, S. S., Tomasi, J., Barone, V., Mennucci, B., Cossi, M., Scalmani, G., Rega, N., Petersson, G. A., Nakatsuji, H., Hada, M., Ehara, M., Toyota, K., Fukuda, R., Hasegawa, J., Ishida, M., Nakajima, T., Honda, Y., Kitao, O., Nakai, H., Klene, M., Li, X., Knox, J. E., Hratchian, H. P., Cross, J. B., Bakken, V., Adamo, C., Jaramillo, J., Gomperts, R., Stratmann, R. E., Yazyev, O., Austin, A. J., Cammi, R., Pomelli, C., Ochterski, J. W., Ayala, P. Y., Morokuma, K., Voth, G. A., Salvador, P., Dannenberg, J. J., Zakrzewski, V. G., Dapprich, S., Daniels, A. D., Strain, M. C., Farkas, O., Malick, D. K., Rabuck, A. D., Raghavachari, K., Foresman, J. B., Ortiz, J. V., Cui, Q., Baboul, A. G., Clifford, S., Cioslowski, J., Stefanov, B. B., Liu, G., Liashenko, A., Piskorz, P., Komáromi, I., Martin, R. L., Fox, D. J., Keith, T., Al-Laham, M. A., Peng, C. Y., Nanayakkara, A., Challacombe, M., Gill, P. M. W., Johnson, B., Chen, W., Wong, M. W., Gonzalez, C., and Pople, J. A. *Gaussian 03, Revision D.02*. Gaussian, Inc., Wallingford CT, (2005).

[139] Foresman, J. B. and Frisch, Æ. *Exploring Chemistry with Electronic Structure Methods*. Gaussian Inc., Pittsburgh PA, 2 edition, (1996).

[140] Bacskay, G. B. *Chem. Phys.* **61**, 385–404 (1981).

[141] Hariharan, P. C. and Pople, J. A. *Theor. Chem. Acc.* **28**, 213–222 (1973).

[142] Francl, M. M., Petro, W. J., Hehre, W. J., Binkley, J. S., Gordon, M. S., De Frees, D. J., and Pople, J. A. *Theor. Chem. Acc.* **77**, 3654–3665 (1982).

[143] Binkley, J. S., Pople, J. A., and Hehre, W. J. *J. Am. Chem. Soc.* **102**, 939–947 (1980).

[144] Gordon, M. S., Binkley, J. S., Pople, J. A., Pietro, W. J., and Hehre, W. J. *J. Am. Chem. Soc.* **104**, 2797–2803 (1982).

[145] Pietro, W. J., Francl, M. M., Hehre, W. J., Defrees, D. J., Pople, J. A., and Binkley, J. S. *J. Am. Chem. Soc.* **104**, 5039–5048 (1982).

[146] Dobbs, K. D. and Hehre, W. J. *J. Comput. Chem.* **7**, 359–378 (1986).

[147] Dobbs, K. D. and Hehre, W. J. *J. Comput. Chem.* **8**, 861–879 (1987).

[148] Sánchez-Portal, D., Ordejón, P., Artacho, E., and Soler, J. *Int. J. Quantum Chem.* **65**, 453–461 (1997).

[149] Perdew, J. P. and Zunger, A. *Phys. Rev. B* **23**(10), 5048–5079 May (1981).

[150] Junquera, J., Zimmer, M., Ordejón, P., and Ghosez, P. *Phys. Rev. B* **67**(15), 155327–155338 Apr (2003).

[151] Duin, A. C. T., Merinov, B. V., Han, S. S., Dorso, C. O., and Goddard III, W. A. *J. Phys. Chem. A* **112**, 11414–11422 (2008).

[152] Levine, N. I. *Quantum Chemistry.* Prentice Hall, Upper Saddle River NJ, 5 edition, (1999).

[153] Dolg, M., Wedig, U., Stoll, H., and Preuss, H. *J. Chem. Phys.* **86**, 866–872 (1987).

[154] Kaupp, M., von Schleyer, P. R., Stoll, H., and Preuss, H. *J. Chem. Phys.* **94**, 1360–1366 (1991).

[155] Dolg, M., Stoll, H., Preuss, H., and Pitzer, R. M. *J. Phys. Chem.* **97**, 5852–5859 (1993).

[156] Giannici, F., Longo, A., Balerna, A., Kreuer, K. D., and Martorana, A. *Chem. Mater.* **19**, 5714–5720 (2007).

[157] Feller, D. *J. Comput. Chem.* **17(13)**, 1571–1586 (1996).

[158] Schuchardt, K. L., Didier, B. T., Elsethagen, T., Sun, L., Gurumoorthi, V., Chase, J., Li, J., and Windus, T. L. *J. Chem. Inf. Model.* **47(3)**, 1045–1052 (2007).

[159] Cao, X. and Dolg, M. *J. Chem. Phys.* **115**, 7348–7355 (2001).

[160] Dapprich, S., Komàroni, I., Byun, K. S., Morokuma, K., and Frisch, M. J. *J. Mol. Struct. (Theochem)* **461–462**, 1–21 (1999).

[161] Lee, C., Yang, W., and Parr, R. G. *Phys. Rev. B* **37**(2), 785–789 Jan (1988).

[162] Miehlich, B., Savin, A., Stoll, H., and Preuss, H. *Chem. Phys. Lett.* **157**(3), 200–206 (1989).

[163] Vosko, S. H., Wilk, L., and Nusair, M. *Can. J. Phys.* **58**, 1200–1211 (1980).

[164] Giannici, F., Longo, A., Balerna, A., and Martorana, A. *Chemistry of Materials* **21**(4), 597–603 (2009).

[165] Takeuchi, K., Loong, C. K., Richardson Jr., J. W., Guan, J., Dorris, S. E., and Balachandran, U. *Solid State Ionics* **138**, 63–77 (2000).

[166] Kreuer, K.-D., Münch, W., Ise, M., He, T., Fuchs, A., Traub, U., and Maier, J. *Ber. Bunsenges. Phys. Chem.* **101**(9), 1344–1350 (1997).

[167] Björketun, M. E., Sundell, P. G., and Wahnström, G. *Phys. Rev. B* **76**, 54307–54315 (2007).

[168] Iguchi, F., Sata, N., Tsurui, T., and Yugami, H. *Solid State Ionics* **178**, 691–695 (2007).

[169] Cervera, R. B., Oyama, Y., Miyoshi, S., Kobayashi, K., Yagi, T., and Yahaguchi, S. *Solid State Ionics* **179**, 236–242 (2008).

[170] Zhao, Y. and Weidner, D. J. *Phys. Chem. Minerals* **18**, 294–301 (1991).

[171] Williams, T., Kelley, C., et al. Gnuplot, Version 4.4, http://www.gnuplot.info.

[172] Kittel, C. *Introduction to Solid State Physics.* John Wiley and Sons, Inc., 7th edition, (1996).